PHYSICAL, STRUCTURAL, THERMAL AND OPTICAL PROPERTIES OF TERNARY AND QUATERNARY CHALCOGENIDE GLASSY SEMICONDUCTORS

THESIS SUBMITTED IN FULFILLMENT OF THE REQUIREMENTS FOR THE DEGREE OF

DOCTOR OF PHILOSOPHY

IN

PHYSICS

BY

NEHA SHARMA

[Enrollment Number 096904]

DEPARTMENT OF PHYSICS AND MATERIALS SCIENCE

JAYPEE UNIVERSITY OF INFORMATION TECHNOLOGY

WAKNAGHAT, SOLAN (H.P) – 173234

INDIA

JULY 2013

CERTIFICATE

This is to certify that the thesis entitled, "**Physical, Structural, Thermal and Optical Properties of Ternary and Quaternary Chalcogenide Glassy Semiconductors**" which is being submitted by **Miss Neha Sharma** for the award of degree of **Doctor of Philosophy** in **Physics** by the **Jaypee University of Information Technology** at Waknaghat, is the record of candidate's own work carried out by her under our supervision. This work has not been submitted partially or wholly to any other University or Institute for the award of this or any other degree or diploma.

Dr. Pankaj Sharma

Supervisor–I
Email: pankaj.sharma@juit.ac.in
Phone: +91 94189 52533

Dr. Vineet Sharma

Supervisor–II
Email: vineet.sharma@juit.ac.in
Phone: +91 94182 33083

Acknowledgement

I am most thankful to ***Almighty*** *for strength and courage He has bestowed upon me.*

Foremost, I am deeply indebted to my supervisors **Dr. Pankaj Sharma** and **Dr. Vineet Sharma** for their continuous support and motivation in my Ph.D. work. Without their kind and patient instructions, it would have been difficult for me to complete this work.

I express my deepest gratitude to **Prof. (Dr.) Yajulu Medury (COO, JES)**, **Brig. (Retd.) Balbir Singh (Director, JUIT)** and **Prof. T.S. Lamba (Dean A&R)** for providing me financial support and assistance in all forms during the research work.

My sincere thanks to **Prof. (Dr.) P.B. Barman**, Head, Department of Physics and Materials Science, Jaypee University of Information Technology, Waknaghat for his kind support. I want to thank Prof. (Dr.) Sunil K. Khah, Dr. Dheeraj Sharma, Dr. Rajesh Kumar, Dr. S.K. Hazra, Dr. Ragini Raj Singh and Dr. S.K. Tiwari for their interest and valuable suggestions. I am also thankful to the non–teaching staff for their kind cooperation during entire work

I extend my gratitude to **Prof. (Dr.) S.C. Katyal**, JIIT Noida, for motivation and encouragement during my initial days of research work

Away from home, I have been very fortunate to meet people who have always been very kind and supportive. I feel very thankful to my friends, Mr. Suresh Kumar, Ankush Thakur, Abhishek Kandwal, Pawan Kumar, Hitanshu Kumar and Dikshita Gupta for making my days wonderful at JUIT. I would like to give special thanks to **Sunanda Sharda** for the discussions, for the sleepless nights we worked together before deadlines and for all the funs we have had in last four years. I also want to thank Miss Khushboo Kashyap (Delhi University) for concern, help and good wishes.

Ever thanks to **my parents** and **sister** and everyone back home for the inspiration and moral support. I am greatly indebted to them for their love and prayers.

Date: July 25, 2013 **(Neha Sharma)**

Contents

List of Figures

List of Tables

CHAPTER 1

Introduction

Materials have played an important part in our civilization. These are either natural like wood, or synthetic like plastic. The development of materials has given rise to the various eras as Stone Age, Bronze Age, and Steel Age. Modern materials science owes its origin to metallurgy, which has evolved from mining and use of fire. Scientists are using metals in various ways to engineer new materials. For example, metals become ceramics with the addition of oxygen or nitrogen. Materials science is one of the oldest forms of applied science that has been derived from the manufacture of ceramics. The understanding of materials really kick started in late 19^{th} century when it was recognized that the thermodynamic properties associated with atomic structure in various phases are related to the physical properties of material. Materials science has been driven with the development of revolutionary technologies such as plastics, semiconductors, biomaterials, etc. Materials science is an interdisciplinary field that applies the properties of matter to various areas of science. The basis of material science is solid–state physics for the understanding of the electronic, thermal, magnetic, chemical, structural and optical properties of materials.

Solid state physics is the study of rigid matter or solids through methods such as crystallography and metallurgy. Solid–state physics studies how the large–scale properties of solid materials result from their atomic–scale properties. Solids are a particular state of condensed matter characterized by strong interaction between their constituent particles (atoms, molecules). Solids are considered as materials with viscosities exceeding $10^{14.6}$ Poise while fluids (liquids and gases) have viscosities below this value.

1.1 Classification of solids

Solids can be broadly classified into two types based on the arrangement of their structural units as; crystalline solids and non–crystalline or amorphous solids.

1.1.1 Crystalline solids

A crystal is a regular three dimensional design and is a consequence of the regular arrangement of constituent atoms, ions or molecules. Crystalline materials have directional properties and therefore are also called as anisotropic materials. Crystalline materials exist either in a single crystalline form or in a polycrystalline form. (i) A single crystal consists of only one crystal and for semiconductor devices such types of crystals are used. Crystals often show cleavage on certain planes that indicates some planes of atoms are linked by weaker bond. (ii) Polycrystalline solids consist of many small crystals. These small crystals are known as grains and the properties of these polycrystalline solids are dominated by boundaries between crystallites called grain boundaries. Ceramics are the examples of polycrystalline solids. Atomic arrangement of crystalline and polycrystalline solids are shown in Figure 1.1.

1.1.2 Non–crystalline solids

In non–crystalline solids, the constituent particles are not arranged in an orderly manner. They do not have long range order of atoms in their structure and hence atoms have random distribution. They are of short range order, extending over a few atomic radii and do not have any correlation with atoms situated at longer distance. Arrangements of atoms in amorphous solid are shown in Figure 1.1. They do not have directional properties and are called isotropic substance.

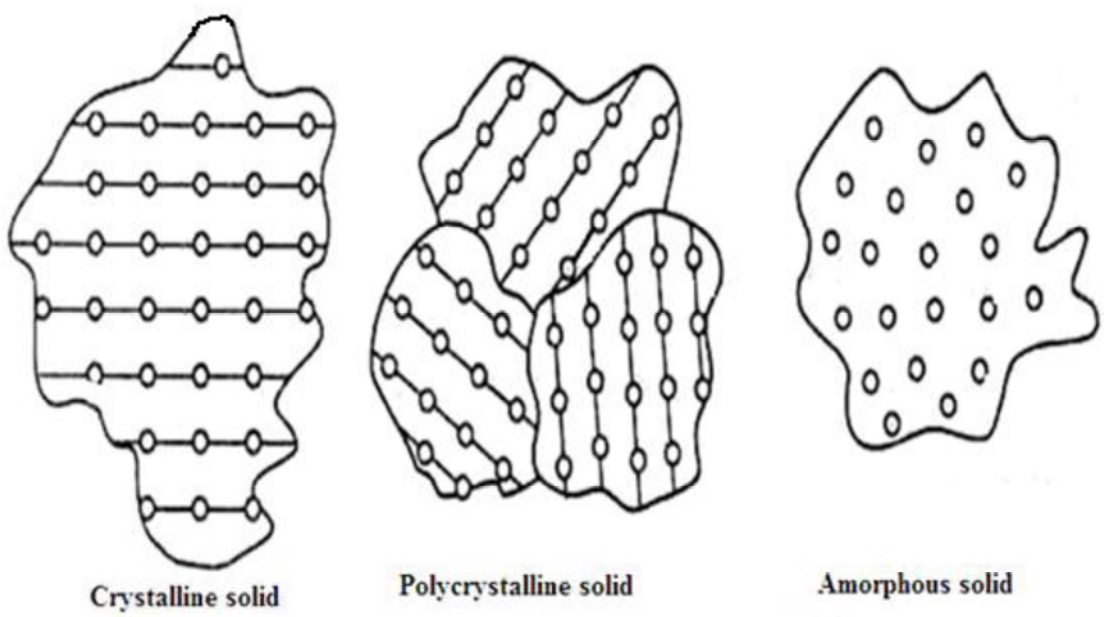

Figure 1.1 Atomic arrangements in solids.

Amorphous materials can be semiconductor, insulator and in some cases at very low temperature they even behave as superconductors. When a liquid is cooled below its melting temperature with slow cooling rate, its viscosity increases and liquid starts solidifying and crystallization takes place. If cooling rate is ultra high then liquid becomes super–cooled and if the viscosity rises enough then material takes amorphous or non–crystalline form.

1.2 Classification of amorphous materials

On the basis of chemical bonding, amorphous materials can be classified into two major categories as shown in Figure 1.2.

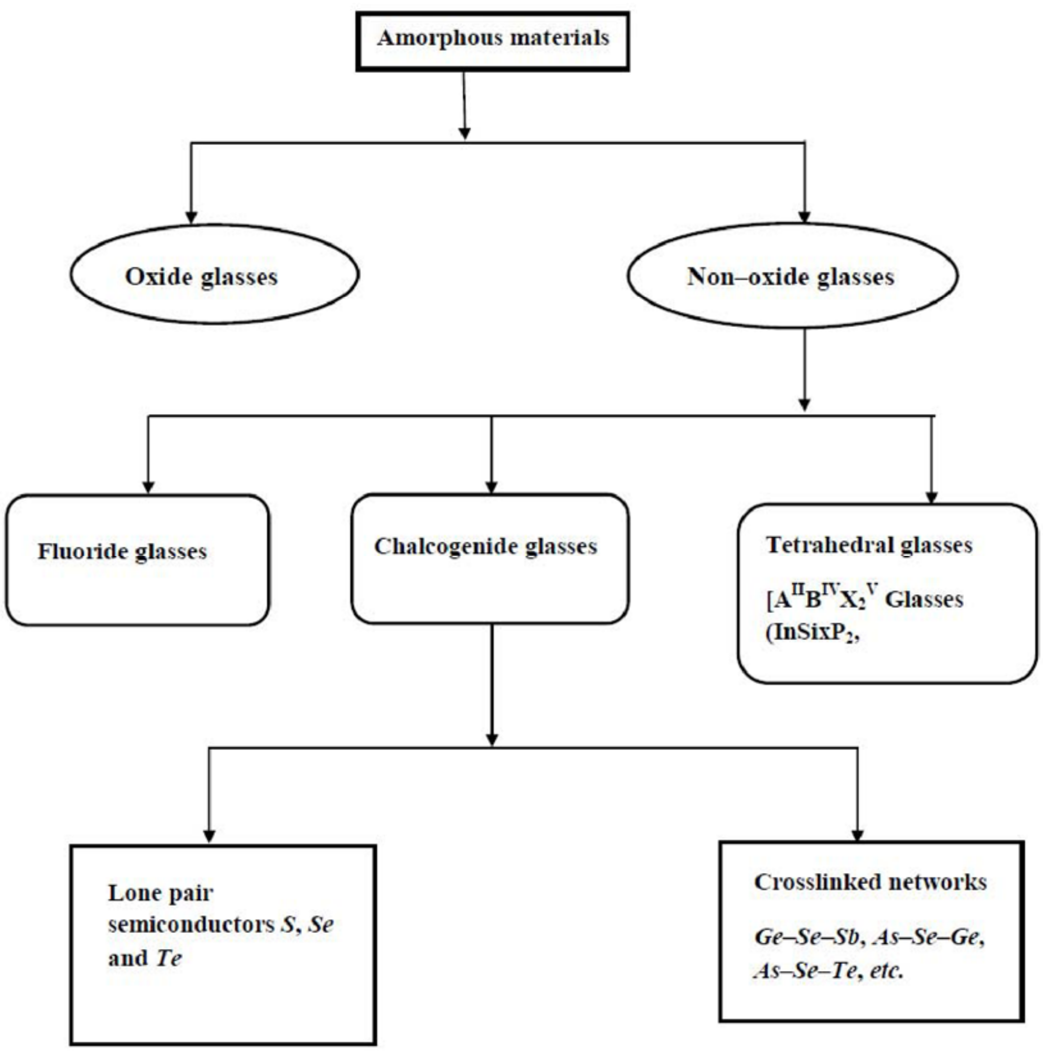

Figure 1.2 Classification of amorphous materials.

1.2.1 Oxide glasses

Oxide glasses such as silicates (*SiO_2*) have strong ionic bonds and are good insulators because electrons in these materials are bound to their ions and are not able to participate in electrical conduction. Silicate glasses are the most ancient materials known to mankind. They also occur naturally (volcanic glasses) and indeed offer important insight into the physico–chemical conditions in the interior of our planet. Structure of SiO_2 glass consists of SiO_4 regular tetrahedra sharing the oxygen at the corner. When these tetrahedra get interconnected then the glass network shows different ring structures. Zachariasen defined SiO_2, B_2O_3, As_2O_3, GeO_2, and P_2O_5 as glass network showing strongly connected continuous three – dimensional network structures [1].

Silica glasses are favorable materials for long distance optical fiber communication. However, these glasses have properties which are not suitable for some applications. Devices based on rare–earth doped silica have relatively long interaction length. Non–linear refractive index of silica glasses is low so that they require high intensity of light in order to function in non–linear devices and also the transmission of silica is limited to 2μm. These are some shortcoming of silica due to which there is need of some novel glasses for optical applications. These new glasses are categorized in non–oxide glasses.

1.2.2 Non–oxide glasses

Non–oxide glasses are divided into three categories; fluoride, tetrahedral and chalcogenide glasses.

Fluoride glass is a class of non–oxide optical glasses composed of ZBLAN (zirconium, barium, lanthanum, aluminum and sodium). As the viscosity of these glasses is very low, when processing through glass transition, crystallization is not avoided completely. Heavy metal fluoride glasses (HMFG) have low optical attenuation and are easy to manufacture, these are fragile as well and also have poor resistance to moisture. HMFG were initially designated for optical fiber applications due to their low intrinsic loss in mid–IR in comparison to silica fibers. Fibers of these glasses are advantageous especially in mid–e infrared 2000–5000 nm range.

1.3 Chalcogenide glasses

Chalcogenide glass contains large amount of chalcogen elements, Sulphur (*S*), Selenium (*Se*) and Tellurium (*Te*) having covalent bonding structure. The name chalcogenide originates from the Greek word "chalcos" meaning ore and "gen" meaning formation, thus, the term chalcogenide is generally considered to mean ore former. These elements are called chalcogenides as their atoms have marked tendency to link together to form long–chain homo polymer [2]. Oxygen also belongs to the same group, but, it has its own class called oxide glasses having distinctly different properties than chalcogenides. One of the basic differences, between these two is band gap; band gap of SiO_2 is around 10 eV while band gap of chalcogenides lie between 1 to 3 eV [3]. The atomic structure of chalcogenides is flexible and viscous. The band gap of chalcogenides is equivalent to the band gap of semiconductor. Thus, chalcogenides are also regarded as soft semiconductor.

1.3.1 Types of chalcogenide glasses

Chalcogens have relatively small glass forming region [4]. So, to increase the glass forming region it is necessary to combine chalcogens with good network formers *viz*., germanium (*Ge*), antimony (*Sb*), arsenic (*As*), tin (*Sn*), etc. Chalcogenide glasses can be further classified as;

i) Lone–pair semiconductors: *S, Se, Te*, As_2Se_3, As_2S_3, etc.

ii) Cross–linked network: When one or more than one element is added into binary system, then structure gets cross-linked *e.g. Ge–Se–Sb*, *As–Se–Ge, As–Se–Te, etc.*

1.3.2 History of Chalcogenide glasses

It is difficult to assign a date that when the field of chalcogenide glasses started. For the vast majority of time, the vitreous glassy state was limited to oxygen compounds and their derivatives. Schulz–Sellack [5] was the first to report data on oxygen free glass in 1870. Though vitreous selenium, arsenic selenide and sulphide were synthesized for the first time at the end of 19^{th} century, but, the scientists were not attracted to these materials. Glassy *Se* became the most concerned subject for scientific community at the beginning of 20^{th} century when Wood [6] and Meier [7] reported first research on this subject.

The first work on chalcogenide glasses (ChG) was attributed to Frerichs in the early 50's on As_2S_3 glass [8, 9] and As_2Se_3 by Fraser [10] and Dewulf [11]. Frerichs also started to work on the development of *Se* glasses and binary compounds with sulphur. Another scientist of vitreous ChG around that time was Winter Klein [12]. The major research on ChG was started by two research groups from Saint–Petersburg (USSR), one group was led by B.T. Kolomiets and N.A. Goryunova from the "A.F. Ioffe Physico–Technical Institute" who were reported to discover the first semiconducting glass [13] based on chalcogen elements while the other group was led by R.L. Myuller. In 1968, S.R. Ovshinsky found memory and switching effects in ChG [14]. This led to the development of non–crystalline chalcogenide glasses in various fields such as xerography, computer memories, etc. Around the same time Sir N. F. Mott (Nobel prize winner in Physics in 1977) and E.A. Davis developed the theory on the electronic processes in ChG [15]. After that several review books were published in subsequent years on glasses like "Chemistry of Glasses" by A. Paul in 1982 [16], "The Physics of Amorphous Solids" by R. Zallan in 1983 [17], "Physics of Amorphous Materials" by S.R. Elliott [18]. However the first review book entirely dedicated to chalcogenide materials, "Glassy Semiconductors", was published in 1981 by Z.U. Borisova who had worked with Myuller. In Moldova, A.M. Andriesh published in 1988 a book entitled "Glassy Semiconductors in Photoelectric Systems for Optical Recording of Information" on ChG with special emphasis on their applications. In 2000, M.A. Popescu gave a detailed account on the physical and technological aspects of chalcogenide systems in his book "Non–Crystalline Chalcogenides" [19]. The "Non–Crystalline Chalcogenides" is the most detailed book published in the field of amorphous and glassy chalcogenide materials. The book covers the scientific and technological information on chalcogens (sulphur, selenium and tellurium) and chalcogenide combinations. R. Fairman has covered properties of ChG along with applications in his book published in series on "Semiconducting Chalcogenide Glasses I, II and III" [20–22]. Recently, V.I. Mikla published a book on "Metastable States in Amorphous Chalcogenide Semiconductors" which explains the metastable states and related effects in depth against the background of a detailed consideration of local atomic and electronic structure, and taking into account a wide range of light–induced effects. [23].

1.4 Properties of chalcogenide glasses – A survey

Various chalcogenide glasses have been reviewed in terms of their composition *i.e.* binary, ternary and quaternary chalcogenide glasses for their structural, thermal and optical properties.

1.4.1 Binary chalcogenide glasses

Chalcogen such as *Se* in its pure form consists of mixture of two structural species *i.e.* long helical chains and eight member rings held to each other. When other element such as *Sb*, *Sn*, *As*, *Pb* is added to *Se* then the rings break down and network get strengthen by cross–linking the chain structure. Various properties have been studied in order to understand binary glasses.

1.4.1.1 Structural properties

Structural properties of chalcogenide glasses have been studied using infrared or Raman spectroscopy. The spectra obtained from infrared or Raman spectroscopy give information about the bonding arrangement of constituent elements which further provide the knowledge of structure of glasses. Various authors have reported about the structure of chalcogenide systems using the spectroscopy study [24–30].

Golovchak *et al.* have carried out work on the structure of homogeneous bulk As_xS_{100-x} ($25 \leq x \leq 42$) glasses, prepared by the conventional rocking melt quenching method, using Raman spectroscopy [24]. Raman spectrum has been measured in 250−550 cm^{-1} region. The main building blocks of the glass networks are regular $AsS_{3/2}$ pyramids and sulfur chains. With the excess of *As* content over the stoichiometric composition (with x = 40 and strongly in x = 42), a distinct (As_4S_4) peak at 364 cm^{-1} becomes evident in the region of stretching vibrations. Fayek has reported about the *GeSe* composition for structural studies using Far infrared (IR) transmission spectrum in spectral range 200–500 cm^{-1} [25]. Spectra of samples have shown strong absorption bands around 231 cm^{-1} and 311 cm^{-1} and have been assigned to *Ge–Se* and *Se–Se* respectively. Theoretical wave number values for *Se−Se* bond is less and for *Ge–Se* bond is greater than experimental values.

Iovu *et al.* have investigated the Raman spectra of As_xSe_{100-x} with $0 \leq x \leq 10$ glasses [26]. *Se* chains and Se_8 closed rings have been formed as majority building units in the system. At higher *As* contents, new structural units have been formed from *As* and *Se* atoms. With further addition of *As*, new *As–Se* structural units, like $AsSe_3$ pyramids, As_4Se_3 and As_4Se_4 cages have been reported [26]. Mykaylo *et al.* have reported about the structural properties of glassy $As_{40}Se_{60}$ [27]. Raman spectrum indicated a strong band at 227 cm^{-1} suggesting the structural group of $AsSe_{3/2}$ pyramids. Weak peculiarities within the range of 110 cm^{-1} – 150 cm^{-1} and 250 cm^{-1} have been connected with the presence of molecular fragments of *As−As* and *Se−Se* homopolar bonds in the glass matrix.

Santos *et al.* have reported the *GeSe* and $GeSe_2$ compositions, films have been deposited using thermal evaporation technique onto silica glass substrate [28]. IR spectra of annealed films have been recorded in reflection mode. For the $GeSe_2$ composition, the reflection spectrum has been dominated by a peak at 253 cm^{-1} and assigned as asymmetric stretching mode of the $GeSe_4$ tetrahedron, plus a minor peak at 220 cm^{-1}. For *GeSe* composition, main band at ~251 cm^{-1} corresponding to *Ge–Se* band, plus minor bands at 216 cm^{-1} and 193 cm^{-1} have been reported.

Delaizir *et al.* have studied the structural characterization for As_3Se_7 using Raman spectroscopy [29]. Raman spectra have been recorded at room temperature on a confocal micro–Raman instrument with a typical resolution of 3 cm^{-1}. The glass network was reported to be mainly composed of corner sharing [$AsSe_{3/2}$] pyramids and [$AsSe_{3/2}$] pyramids connected by *Se–Se* bonds. Sharma *et al.* have carried out work on Far–IR transmission spectrum for $Ge_{0.17}Se_{0.83}$ glassy alloys in spectral range of 500–200 cm^{-1} at room temperature [30]. Main absorption bands at ~250 cm^{-1} and 300 cm^{-1} have been reported. Band at 250 cm^{-1} corresponding to Se_8 (A_1, E mode) and 300 cm^{-1} has been assigned as *Ge–Se–Ge* (ν_1 mode).

Results obtained from survey give the knowledge of bonding network in terms of various units and modes obtained from constituent elements. Vibrational study reveals that binary chalcogenide glasses have transmission window in far infrared spectral domain region.

1.4.1.2 Thermal properties

Thermal property gives the information of various reactions that take place with the change in temperature. Differential scanning calorimeter (DSC) and differential thermal analysis (DTA) have been used extensively in recent times to study glass–transition behavior and thermodynamic properties. These techniques give the detailed probing of the nature of the glass transition and molecular networks. Several authors have studied thermal properties [31–42].

Holubova *et al.* have carried out work on *As* and *Sb* doped *Se* to study thermal properties [31]. Low content of *As* and *Sb* have been taken ranging from $x = 0, 1, 2, 4, 8$ and 16 in As_xSe_{100-x} and Sb_xSe_{100-x} glass forming systems. Stepscan DSC instrument was used to take the measurements at different heating rates. For As_xSe_{100-x} system, glass transition temperature (T_g) increases almost linearly with increasing *As* content from 40 ^{o}C up to 93 ^{o}C. The glass transition temperature of Sb_xSe_{100-x} changes only slightly in the same temperature range.

Shaaban *et al.* have reported the $Ge_{25}Se_{75}$ composition for thermal properties *viz.* (T_g), crystallization temperature (T_c), melting temperature (T_m), activation energy of glass transition temperature (E_g) and activation energy for crystallization (E_c) [32]. The calorimetric measurements have been carried out using DSC at four heating rates (γ = 5, 10, 20, 30, 40 K min^{-1}). The values of T_g, T_c and T_m reported to increase with increasing heating rates.

Bletskan has studied the glass formation and crystallization in $Ge-Te$ system using DTA measurement [33]. With increasing content of tellurium, glass forming tendency decreases and T_c reaches a maximum at 80 at.% of *Te*. Piarristeguy *et al.* have reported about glass formation in the Ge_xTe_{100-x} binary system using twin roller quenching (TRQ) and co–thermal evaporation techniques (CTE) synthesis methods [34]. The glass–forming regions are: 11.7–22.0 at.% *Ge* for bulk flakes and 10.2–35.9 at.% *Ge* for films. The thermal behavior of both bulk and film glasses have been investigated using DSC. T_g and T_c increase with the addition of *Ge* content for both methods. Sushama *et al.* have carried out the kinematical studies of glass transition and crystallization in glassy *Se–In* using DSC [35]. Glass transition region has been reported in terms of activation energy. Reported values of T_g, T_c and E_c are 322 K, 398 K, 12.14 kJ/mol respectively.

Tiwari *et al.* have studied $Se_{80}Ge_{20}$ composition for kinetic parameters under non–isothermal condition using DSC technique [36]. Fragility of glass decreases with increasing heating rate. Kotkata *et al.* have carried out work on crystallization parameter for $Se_{0.95}In_{0.05}$ and $Se_{0.90}In_{0.10}$ chalcogenide glasses at different heating rate [37]. The values of E_c show a decrease with increasing *In*–content. With the increasing heating rate for both the systems, T_g and T_c increase while T_m remains constant. Values of T_g, T_c and T_m for $Se_{0.90}In_{0.10}$ system are greater than $Se_{0.95}In_{0.05}$. The reported value of E_c show a decrease from 179 kJ/mol for pure *a–Se* to 118.06 ± 0.16 kJ/mol for $Se_{0.95}In_{0.05}$ and to 113.94 ± 0.25 kJ/mol for 10 at.% of *In*. Mehta *et al.* have reported the isothermal crystallization for $Se_{80}Ge_{20}$ and $Se_{78}Ge_{22}$ glassy alloys [38]. The reported value of E_c for $Se_{80}Ge_{20}$ is 0.61 eV and for $Se_{78}Ge_{22}$ is 0.63 eV.

Mehta *et al.* have investigated the glass forming ability and thermal stability of some *Se–Sb* glassy alloys using DSC technique at four heating rates (5, 10, 15 and 20 ^oC/min) [39]. The studied compositions are $Se_{98}Sb_2$, $Se_{96}Sb_4$, $Se_{94}Sb_6$, $Se_{92}Sb_8$, $Se_{90}Sb_{10}$. Thermal stability parameter of the samples increases with the increasing heating rate except for 10 ^oC/min. Thermal stability parameter decreases with the increasing content of *Sb*, except for 4 and 6 at.% of *Sb*.

Saraswat *et al.* have reported the specific heat studies in *a-Se* and *a-*$Se_{90}M_{10}$ (*M* = *In*, *Sb*, *Te*) alloys [40]. DSC scans have been taken at a heating rate of 10 ^oC. Specific heat values reported for *a-Se*, $Se_{90}In_{10}$, $Se_{90}Sb_{10}$, $Se_{90}Te_{10}$ are 0.08, 0.013, 0.016, 0.18 J/g/^oC respectively. Mehta *et al.* studied the non–isothermal crystallization of glassy $Se_{85-x}Te_{15}$ using DSC instrument at different heating rates 5, 10, 15, 20 K/min [41]. The reported values of T_g increase with increasing heating rate and value of E_c is 0.553 eV. Kapoor *et al.* have reported activation energy for glass transition, thermal stability and activation energy for crystallization transition temperature for *Se–Te* glassy alloys using DTA [42]. The obtained values for T_g, T_c, T_g-T_c and E_c are 354.17 K, 420.37 K, 66.2 K, 142.83 kJ/mol, respectively.

The glassy *Se* is thermally unstable so alloying it with other elements has shown an improvement in the thermal stability. The addition of elements having high metallic character leads to easy crystallization. *Te* based glasses exhibit poor stability and crystallization ability is large during heating. Specific heat values increases with the addition of second element. The glass transition temperature shows an increase with the addition of second element. Fragility of glasses shows a decrease with the increasing heating rate.

1.4.1.3 Optical properties

When light interact with the material it leads to various optical phenomena. The nature of this interaction between light and material is expressed in term of dielectric response of the material. The dielectric response can be calculated from the complex refractive index. Many authors have reported about the optical properties; refractive index (n), extinction coefficient (k) and absorption coefficient (α) for various chalcogenide glasses [43–56]

Nemec *et al.* have reported for thin amorphous As_xSe_{100-x} (x = 50, 57.1, 60) films prepared using pulsed laser deposition technique (PLD) and thermal evaporation (TE) [43]. With increasing content of *As* optical band gap (E_g^{opt}) decreases for PLD films and increases for TE films. The values of E_g^{opt} are higher for TE films in comparison to PLD films. Shaaban *et al.* carried out work on thermally evaporated amorphous $As_{40}S_{60}$, $As_{35}S_{65}$ and $As_{30}S_{70}$ thin films deposited by thermal evaporation [44]. The optical transmission spectra at normal incidence have been taken over the 400–900 nm spectral regions by a double beam computer controlled spectrophotometer. The values of n gradually increase towards the stoichiometric composition $As_{40}S_{60}$. The values of E_g^{opt} have been reported to decrease with the increasing *As* content.

Kotkata *et al.* have studied the effect of *In*–content on the optical properties of *a–Se* films [45]. Films have been deposited using thermal evaporation technique and properties were studied in the spectral region 500–2500 nm. With *In* addition from 0.0 to 0.35, n increases and E_g^{opt} decreases. Fadel *et al.* have reported the optical properties of $Se_{0.62}Ge_{0.38}$ glass; film was deposited using thermal evaporated technique on glass substrate [46]. Transmission spectrum was taken in wavelength range of 400–2500 nm and reported an optical band gap (E_g^{opt}) of 1.79 eV.

Shaaban *et al.* have reported the optical band gap and refractive index for amorphous semiconductor $Se_{70}S_{30}$ thin films deposited by electron beam evaporation. [47]. Transmittance spectra in the wavelength range 400–2500nm have been measured at normal incidence and used to determine refractive index (n). The value of n decreases with increasing wavelength and value of E_g^{opt} is 2.25 eV.

Optical parameters for $Se_{1-x}Sb_x$ (x = 0, 0.025, 0.050, 0.075, 0.10) have been reported by Sharma *et al.* [48]. Optical properties of system have been investigated using transmission spectra in the range 400–1200 nm. On addition of *Sb* to *Se*, transmission shifts to higher wavelength in the interference free region. Refractive index and extinction coefficient increase with increasing content of *Sb*. *Sb* incorporation to *a-Se* decreases the optical energy gap. Pan *et al.* have studied amorphous $GeSe_2$, film deposited by the pulsed laser deposition technique and annealed at different temperatures from 473 to 623 K [49]. The reported value of E_g^{opt} is 1.95 eV. The transmission and absorption spectra of the films have been measured using the spectrophotometer. With increase in annealing temperature, E_g^{opt} has been reported to increases.

Amorphous $Sb_{10}Se_{90}$ thin film deposited using thermal evaporation has been studied by Othman [50]. The changes in the optical properties (transmittance, optical band gap, absorption coefficient, refractive index and extinction coefficient) have been measured in the wavelength range 500–900 nm for the virgin and ultraviolet (UV) illuminated films. The values of E_g^{opt} decrease (photo–darkening) and the refractive index increases with the increase of UV exposure time.

Mainka *et al.* have carried out work on an optical study of amorphous $Se_{80}Te_{20}$ using transmission spectra in the wavelength range 500–2500 nm [51]. The reported value of n at 800 nm is 3.370 and the value of E_g^{opt} is 1.41 eV. Santos *et al.* have deposited the $GeSe_2$ film on *Si* and SiO_2 glass using thermal evaporation technique [28]. The ellipsometric measurements have been made at an angle of incidence of 70°, using the Jobin–Yvon UVISEL NIR Spectroscopic Phase Modulated Ellipsometer across the spectral range 4.7–0.75 eV (264–1650 nm). On *Si* substrate, reported value of E_g^{opt} is 2.19 eV and on SiO_2 substrate, value of E_g^{opt} is 2.05 eV.

Sharma *et al.* have reported the optical parameters for $Ge_{0.17}Se_{0.83}$ film deposited using thermal evaporation technique [52]. The normal incidence transmittance and reflectance spectrum in the spectral range 400 nm – 2000 nm of film has been obtained from a double beam ultraviolet–visible–near infrared spectrophotometer to determine E_g^{opt}. The reported value of E_g^{opt} is 1.80 eV. Aly has reported the optical parameters for amorphous $Se_{70}Te_{30}$ and $Se_{70}As_{30}$ thin films deposited onto glass substrates using thermal evaporation [53]. The transmission spectra of the films at normal incidence have been used in the wavelength range

400–2500 nm to calculate optical parameters. The value of n for $Se_{70}Te_{30}$ thin film is larger and E_g^{opt} is smaller than $Se_{70}As_{30}$.

Bahishthi *et al.* have studied the effect of laser irradiation on the optical properties of thermally evaporated $Se_{100-x}Te_x$ (x = 8, 12, 16) thin films [54]. The results show that the irradiation causes a shift in the optical gap. Reported values indicate that absorption coefficient (α) increases and E_g^{opt} decreases with increasing *Te* content and with laser irradiation α increases and E_g^{opt} decreases.

Mishra *et al.* have reported about $Se_{80}Te_{20}$ thin films deposited by thermal evaporation technique on quartz glass [55]. Spectral dependence of the transmittance in the spectral range 300–1200 nm has been measured for these films. The reported values of n and E_g^{opt} are 1.76 and 0.55 eV, respectively. Machado *et al.* have carried out work on optical properties of an amorphous $Se_{0.90}S_{0.10}$ alloy [56]. Absorbance measurements were carried out using Shimadzu UV–2401–PC spectrometer. The absorption edge appears around 620–680 nm and value of E_g^{opt} is 1.81 eV.

Arsenic sulphide (As_2S_3) glass has been widely used in optical devices because of its good transparency and excellent resistance against moisture and corrosive chemicals [45]. It is difficult to prepare *Sb–Se* glasses with *Sb* content higher than 10 at.% using the melt quenching technique. Addition of impurities such as *Sb* to amorphous *Se* noticeably changes its physical properties. UV exposure induced changes, as high as 1%, in the refractive index indicate $Se_{90}Sb_{10}$ as a possible candidate for optical recording [50].

1.4.2 Ternary chalcogenide glasses

Most of the binary chalcogenides are in floppy mode due to which their structure is weak and system remains in 2–D network. To overcome this drawback, third element needs to be added. With the addition of third element, degree of cross linking in the structure increases, hence, system become rigid and 2–D network transits to 3–D network. There are some compositions at which network are fully crosslinked and system is completely stable. The properties of most chalcogenide glasses are composition–dependent. Adding third element to the binary system significantly affects the various properties of the system. Several properties of such ternary system have been studied by various researchers and are reviewed below.

1.4.2.1 Structural properties

Mykaylo *et al.* have studied the Raman spectra of $As_{40}S_{60-x}Se_x$ (x = 0, 10, 15, 20) glasses and thin films [27]. The Raman spectra for glasses and thin films have been taken at room temperature using He–Ne (λ = 0.630 μm) laser. The structure of glasses and thin films has been given in the form of the matrix consisting of pyramidal AsS_3, $AsSe_3$ and mixed AsS_mSe_{3-m} (m = 1, 2) units. These structural units are linked by S or Se atoms. The matrix also contains molecular fragments with $As–As$, $S(Se)–S(Se)$ homopolar bonds. Structure characterizations for $As_3Se_{7-x}Te_x$ ($0 \leq x \leq 3$) and $AS_2Se_{3-x}Te_x$ ($0 \leq x \leq 2.5$) glasses have been investigated by Delaizir [29]. Infrared measurements have been performed on $As–Se–Te$ bulk glasses at room temperature using Fourier−transform vacuum spectrometer (Bruker 113v), equipped with two sources (globar and Hg arc), two detectors (DTGS with KBr and polyethylene windows). Raman spectra have been recorded at room temperature on a confocal micro Raman instrument with a typical resolution of 3 cm^{-1} window. An introduction of tellurium in the structure of both glasses induces the breaking of $Se–Se$ bonds and the formation of $Te–Se$ bonds.

Sharma *et al.* have reported about $Ge_{0.17}Se_{0.83-x}Sb_x$ (where x = 0.03, 0.09, 0.12, 0.15) glass alloys for Far–IR studies using spectral range 500–200 cm^{-1} [30]. With increase in Sb content some new bands appeared at 228–231 cm^{-1} and 250–260 cm^{-1}. Bands at 228–231 cm^{-1} have been assigned to $Se–Sb$ bonds and 250–260cm^{-1} corresponding to Se_8. Boulmetis *et al.* have investigated Ge-As-S samples for structural analysis [57]. The Raman scattering spectra of several $(GeS_2)_x(As_2S_3)_{1-x}$ (x = 0.40, 0.60, 0.80, 0.83, 0.90) glasses have been measured over temperatures ranging from 20 K, through the glass transition temperature T_g and up to a temperature close to the melting point. Non stoichiometric $Ge_{0.30}As_{0.10}S_{0.60}$ glass has been reported to show high degree of disorder due to presence of homopolar $Ge–Ge$ bonds in comparison to the stoichiometric $Ge_{0.25}As_{0.10}S_{0.65}$.

El–Sayed has reported about the Far–IR studies of the amorphous $Sb_xGe_{28-x}Se_{72}$ (x = 0, 8, 16, 24 at.%) glassy semiconductors [58]. The Far–IR transmission spectra of different alloys have been recorded on a Fourier transform IR (Perkin–Elmer) double beam 598 spectrophotometer in conjunction with the KBr disc technique, over the spectral range of 4000–200 cm^{-1} at room temperature. The infrared features are assigned to *Ge–Se* bonds in $GeSe_4$ tetrahedral units and *Sb–Se* bonds in pyramidal molecules.

Wang *et al.* have carried out work on Far–IR transmitting *Te*–based chalcogenide glasses [59]. Far–IR transmitting glass systems including *Ge–In–Te*, *Ge–Ga–Te* along with some compositions containing alkali halides (*KI*, *CsI*) or metal halides (PbI_2, *CuI*, *AgI*, CdI_2 or ZnI_2) are reported. The broad absorption peak in the 15–20 μm disappeared in the Fourier–transform infrared (spectrometer) spectra when gallium is replaced by indium.

Adam *et al.* have reported the infrared and Raman measurements for $Sn_xSb_5Se_{95-x}$ system, where $x = 0$, 5, 10 and 12.5 mole% [60]. Addition of *Sn* causes a shift in peak and occurrence of new transmission bands around 117–145 cm^{-1} in $Sn = 5$ mole% until 180 cm^{-1} in $Sn = 12.5$ mole % spectra. These are ascribed to asymmetrical infrared active of tetrahedral $SnSe_4$ mode. Raman spectra reveal the increase of peak intensity and causes Raman shift towards 183 cm^{-1}, indicating the occurrence of *Sn–Se* bonds with addition of *Sn*.

Fayak has studied the effects of *Sn* addition on structural properties in *Ge–Se* chalcogenide glass [25]. Far–IR transmission spectra of homogeneous compositions in the glassy alloy system $Ge_{1-x}Sn_xSe_{2.5}$ ($0 \leq x \leq 0.6$) have been observed in the spectral range 200–500 cm^{-1} at room temperature. The infrared absorption spectra show strong bands around 231 cm^{-1}, 284 cm^{-1} and 311 cm^{-1} which are assigned to *GeSe*, *SeSn*, *Se–Se*. The *Sn* atoms appear to substitute for the *Ge* atoms in the outrigger sites of $Ge(Se_{1/2})_4$ tetrahedra up to 0.4. For $x > 0.5$, the glasses show a new vibrational band of an isolated F_2 mode of the *Ge*–centered tetrahedra outside the clusters.

Sun *et al.* investigated the structural changes in $GeTe_4$ glasses with the addition of metals (*Zn*, *Sb*, *In*, *Ga*) using Raman spectroscopy [61]. The Raman spectra of these glasses in the frequency region 100 cm^{-1} – 300 cm^{-1} display four main bands at about 124 cm^{-1}, 140 cm^{-1}, 159 cm^{-1} and 275 cm^{-1} which are contributed by *Ge–Te*, *Te–Te*, *Te–Te* and *Ge–Ge* vibration modes respectively. The intensity of bands at 159 cm^{-1} and 275 cm^{-1} vary with the addition of different glass modifiers. While the relative intensity of the bands at 124 cm^{-1} and 140 cm^{-1} are insensitive to composition changes. Glass modifiers like *Zn*, *In* and *Sb* act as glass network unstabilizers which disorganize the glass network by opening up chain structures of *Ge–Te* and *Te–Te*. In the case of *Ga*, $Ge–(Te–Te)_{4/2}$ tetrahedra and $Ga–(Te–Te)_{3/2}$ triangle formed. Iodine can form covalent bonds with tellurium and decrease the tendency of microcrystal formation. Thus, both *Ga* and iodine ultimately act as glass network stabilizer. Zha *et al.* have reported about $Ge_xAs_ySe_{100-x-y}$ ($33 \leq x \leq 39$ and $12 \leq y \leq 16$) glasses and their structure has been studied by Raman spectroscopic technique [62]. *Ge*–tetrahedrons [$GeSe_4$] dominated in the structural units, and defect bonds, such as *Ge–Ge*, *Ge–As* and *As–As* bonds, also occurred in the glasses.

The progressive shift of infrared absorption to longer wavelengths as *Se* is substituted by the heavier *Te* in *As–Se–Te* has been observed. This extension of the transmission window in the far infrared spectral domain suggest the use of *As–Se–Te* rather than *As–Se* glasses for the development of optical fiber sensors [29]. A great attention has been paid to $As_{40}S_{60-x}Se_x$ glasses and the thin films with increased *Se* content ($x > 20$). The *Ge–As–Se* system is interesting for two main reasons: the system has a broad glass formation region and the optical nonlinearities of the glasses in this system have been observed to be as high as hundreds of times that of silica glass [63]. *Ge*–rich and *Se* deficient *Ge–As–Se* glasses are promising for achieving large photosensitivity. With the addition of halides to *Te*–based chalcogenide glasses, volatility of halogen during synthesis could be avoided [59]. In ternary glass system, the glass composition $Ge_{16}Te_{69}(AgI)_{15}$ has relatively good thermal stability, broad transmission region and good chemical durability [61].

1.4.2.2 Thermal properties

Fayek *et al.* have reported the crystallization kinetics for $As_{30}Se_{70-x}Sn_x$ chalcogenide glasses (where x = 0, 1, 2 and 3) under non-isothermal conditions using DTA [63]. The value of E_c increases up to 2 at.% of *Sn* and then decreases for x = 3 at.%. Alternating differential scanning calorimetry (ADSC) has been used to investigate the effect of *Tl* addition on the thermal properties of $As_{30}Te_{70-x}Tl_x$ ($6 \leq x \leq 22$ at.%) glasses by Sharmila *et al.* [64]. The values of T_g and the specific heat capacity difference, ΔC_p decrease with the addition of *Tl*.

Ko *et al.* have carried out work on $Ge_{18}Sb_{22}Se_{60}$ composition for thermal studies using DSC technique [65]. The crystallization temperatures (T_c) have been determined in the range 278 ^oC–308 ^oC with the heating rates between 2 K/min and 70 K/min. With increase in heating rate the values of T_c increases. The reported value for activation energy of the crystallization is 3.2 eV. Vazquez *et al.* studied the glass−crystal transformation kinetics for $Sb_{0.08}As_{0.44}Se_{0.48}$ (S1), $Sb_{0.12}As_{0.40}Se_{0.48}$ (S2) [66]. The values of T_g, T_c lie between 457.6–482.6 K, 549.4–596.2 K for S1 and 459.2–490.9 K, 579.3–641.4 K for S2 sample, respectively. The values of E_c decrease from S1 to S2 sample.

Prikryl *et al.* have reported the thermal study of $Ge_4Sb_4Te_x$ (x = 8, 9 and 10) glassy alloys [67]. The DSC curves exhibit at least two exothermic peaks in temperature range from 120 ^oC to 210 ^oC. The crystallization temperatures increase slightly with decreasing *Te* content in the series $Ge_4Sb_4Te_{10}$ – $Ge_4Sb_4Te_9$ – $Ge_4Sb_4Te_8$ from 147 ^oC to 160 ^oC. The value of E_c for first peak increases with addition of *Te* content. But, second peak shows an increase up to $Ge_4Sb_4Te_9$ and decreases for $Ge_4Sb_4Te_{10}$. Dahshan *et al.* have carried out work on thermal stability and activation energy for $Ge_{26}Te_{74-x}Cu_x$ (x = 2.5, 5, 7.5, 10 and 12.5 at.%) glasses using DSC technique at various heating rates [68]. The values of T_g and T_c increase with increasing heating rate and decreases with the addition of *Cu*. With increasing content of *Cu,* the value of E_c decreases and thermal stability increases.

Shaaban *et al.* have analyzed $Sb_xGe_{25-x}Se_{75}$ ($0 \leq x \leq 10$) alloys at different heating rates (α = 5, 10, 20, 30, 40, 50 K/min) [69]. With increase in *Sb* content, T_g increases while T_c and T_m decrease. With increase in heating rate, the values of T_g, T_c and T_m increase. E_g increases with addition of *Sb* content. Khan *et al.* have investigated the kinetics of crystallization in $Se_{75}S_{25-x}Cd_x$ (x = 0, 2, 4, 6 and 8) chalcogenide glasses using non–isothermal methods in DSC at different heating rates of 5, 10, 15 and 20 K/min [70]. The reported values of glass transition temperature and crystallization temperatures increase with increasing heating rates. E_c increases on the addition of *Cd* content and thermal stability increases with the increasing heating rate.

Lafi *et al.* have reported work on glass transition temperature and crystallization activation energy in $Se_{90}In_{10-x}Sn_x$ ($2 \leq x \leq 8$) semiconducting glasses using DSC [71]. Results reveal that both T_g and E_c decrease with the addition of *Sn* up to 6 at.% with sharp increase in both values at 8 at.%. Saxena has reported the crystallization study of amorphous $Te_x(Bi_2Se_3)_{1-x}$ alloys with variation of the *Se* content [72]. T_g increases slightly with variation of the *Se* content from 42 at.% to 57 at.%. The *Te–Bi–Se* system has shown a reduced tendency towards glass formation at higher *Se* concentrations.

Naqvi *et al.* have carried out work on $Se_{80-x}Te_{20}Zn_x$ (x = 2, 4, 6, 8, and 10) glasses and studied the kinetics of phase transformations using DSC under non–isothermal condition at five different heating rates in these glasses [73]. E_g decreases while E_c increases with increase in *Zn* content. Fayek *et al.* have reported the thermal analysis of $Ge_{2.5-x}Se_{7.5}Sb_x$ glasses (x = 0.5, 1, 1.5, 1.8 and 2) [74]. Non–isothermal method has been used for measurement in DSC instrument. Results show that the glasses that are rich in *Sb* have lower thermal stability.

Deepika *et al.* have studied the phase transformation kinetics of $Se_{58}Ge_{42-x}Pb_x$ (x = 9, 12) chalcogenide glasses using DSC at five different heating rates under non−isothermal conditions [75]. The values of T_g increases with increasing heating rate and decreases with the addition of *Pb* content. E_g increases with incorporation of *Pb* content. Shaaban *et al.* have reported for the kinematical studies of glass transition and crystallization in glassy $Se_{85-x}Te_{15}Sb_x$ (x = 2, 4, 6 and 8) using DSC [76]. The T_g, T_c, E_g and E_c showed an increasing trend with increasing *Sb* content.

Tiwari *et al.* have studied the DSC curves for $Se_{70}Te_{30-x}Ag_x$ alloys (x = 0, 2, 4, 6) [77]. The values of T_g decrease while E_g increase with incorporation of *Ag* content. Sharma *et al.* have carried out work on calorimetric study of amorphous $Se_{85-x}Te_{15}Bi_x$ (where x = 0, 1, 2, 3, 4, 5) glassy alloys [78]. The values of T_g and T_c shift to a higher temperature with increasing heating rate. With *Bi* addition, the value of T_g increases. The value of T_c increases as *Bi* is introduced to the *Se–Te* host, however, further increase in *Bi* concentration causes the reduction in T_c.

Jain *et al.* have reported the glass transition activation energy E_g, thermal stability of $Se_{90}In_{10-x}Sb_x$ (x = 0, 2, 4, 6, 8, 10) chalcogenide glasses using DSC [79]. DSC thermograms showed that each composition has a single T_g and T_c. The $Se_{90}In_6Sb_4$ glass has the lowest value of E_g. Mehta *et al.* have reported the calorimetric measurements performed in glassy $Se_{75}Te_{15}M_{10}$ (M = *Sb*, *Sn*) alloys to study the effect of *Sb* and *Sn* additives on the kinetics of glass transition and crystallization in glassy $Se_{85}Te_{15}$ alloy [80]. The results show that E_g and E_c increase after the addition of *Sb* and *Sn* additives. The value of E_g is higher in case of *Sn* additive while the value of E_c is higher in case of *Sb* additive.

The decrease of *Te* content in $Ge_2Sb_2Te_5$ based films show an increase in the crystallization temperature of amorphous films [67]. The increased values of T_c may lead to an increase in life time of data storage. The amount of *Sb* has been reported to play a significant role in the crystallization behavior of the *Se–Te* chalcogenide glass, where an increase in *Sb* content turns the glasses more stable [76]. The decrease in T_g for $Se_{70}Te_{30-x}Ag_x$ (x = 0, 2, 4, 6) alloys has been explained in terms of reduced mean atomic masses of these alloys and the poor chalcogenide glass forming ability of *Ag* atom [77]. In $Se_{85-x}Te_{15}Bi_x$ system, stable glasses have been reported only with lower *Bi* concentration [78]. In chalcogens, when elements of III and V groups having light atomic masses, small atomic radii, low ionicity and high covalent character are added, then larger glass formation region expands. On the other hand, when heavy elements are added then glass forming region shrinks. But, with heavy elements, IR transmission range increases and optical band gap decreases. Therefore, generally with the addition of third element to a binary system, the thermal stability of glasses increases.

1.4.2.3 Optical properties

Shaheen *et al.* have carried out work on amorphous $Se_{90}In_{10-x}Sn_x$ (x = 2, 4, 6, 8) thin films of thickness 1000 Å, prepared on glass substrates by the thermal evaporation technique [81]. Optical parameters of these thin films have been studied from the reflection and transmission spectrum at room temperature in the spectral range 400–700 nm. E_g^{opt} decreases on introducing *Sn* to *Se−In* system.

Saffarini *et al.* have studied the optical properties of bulk glasses with the chemical composition $Ge_ySe_{94-y}In_6$ ($8 \le y \le 30$) in spectral range of 250–3000 nm [82]. Optical energy gap has been found to increase up to x = 28.33 and then decreases. Abdel–Rahim *et al.* have studied the optical properties of *as*–deposited $Ge_xSe_{92-x}In_8$ (x = 10, 12.5, 15 and 20 at.%) thin films [83]. The refractive index has maximum value n_{max} at wavelength λ_c, which shifts toward the longer wavelength as the *Ge* content is increased. On the other hand, the value of *k* decreases with increasing wavelength. The value of E_g^{opt} decreases as *Ge* content increases from 8 to 20 at.%.

Pan *et al.* have studied amorphous $(GeSe_2)_{100-x}Bi_x$ (*x* = 0, 0.4, 2 and 4) films deposited by the pulsed laser deposition technique [84]. The optical transmission spectra, absorption spectra of the films have been used to calculate optical parameters. Transmission spectrum has been found to shift towards longer wavelength with *Bi* addition. Refractive index has been observed to increase while E_g^{opt} decreases with the addition of *Bi* content. Sharma *et al.* have reported the influence of *Sb* addition on the optical properties of thin films of the chalcogenide glassy $Ge_{0.17}Se_{0.83-x}Sb_x$ (*x* = 0, 0.03, 0.09, 0.12, 0.15) system [52]. Transmittance (*T*) and reflectance (*R*) spectra have been measured in the spectral region 400–2000 nm. E_g^{opt} decreases with increasing *Sb* content and values lie in range of 1.63−1.92 eV.

Sharma *et al.* have done the optical study for $Ge_{10}Se_{90-x}Te_x$ glassy semiconductors [85]. Optical transmission spectra of thin films have been obtained in the range 400–2400 nm. With the addition of *Te*, spectrum has been found to shift towards the longer wavelength *i.e.* red shift has been observed. The refractive index first decreases (up to 30 at.%) and thereafter increases with *Te* content. The values of *n*, *k* show normal dispersion behavior and *α*, E_g^{opt} (~ 1.86−0.9 eV) decrease with the addition of *Te* content.

Dahshan *et al.* have reported the effect of replacement of *Se* by *Ge* on the optical constants of chalcogenide $Ge_xAs_{20}Se_{80-x}$ (where *x* = 0, 5, 10, 15 and 20 at. %) thin films [86]. The transmission spectra, *T* (*λ*), of the films at normal incidence have been obtained in the spectral region from 400 to 2500 nm. With increasing *Ge* content the *n* and *k* decrease, while the E_g^{opt} increases. Sharma *et al.* have studied the alloy $(As_2Se_3)_{90}Ge_{10}$ [87]. Films were deposited on glass substrate by the thermal evaporation technique. The optical parameters, *n* and *k* have been calculated in the wavelength range 400–1500 nm by analyzing the transmission spectrum. The values of *n* and the *k* decrease with the increase in wavelength.

Petkova *et al.* have studied the $(AsSe)_{100-x}Sb_x$ thin films deposited on glass substrates using vacuum thermal evaporation (*VTE*) [88]. The optical transmission and reflection spectra of thin films have been recorded at room temperature in the range from 400 to 2500 nm. Red shift has been reported for these films. The reported values of optical parameters indicate that the values of n increase and E_g^{opt} decrease. Saleh *et al*. have studied $Sb_{65}Se_{35-x}Ge_x$ (x = 0−20 at.%) thin films, deposited by the electron beam evaporation technique on ultrasonically cleaned glass substrates [89]. E_g^{opt} decreases with addition of *Ge* content. Fadel *et al*. have reported the optical behavior for $Ge_{0.62}Se_{0.35}Sb_{0.03}$ composition [46]. Transmittance and reflectance have been measured using a double beam spectrophotometer in the wavelength range 400–2500 nm. The reported value of E_g^{opt} is 1.79 eV. Shaaban *et al*. have reported the optical properties of $Sb_xGe_{25-x}Se_{75}$ (x = 0, 5, 10, 15, 20 at.%) [90]. Optical measurements have been taken in spectral range of 400−2500 nm. E_g^{opt} has been observed to decrease with increasing content of *Sb*. Optical reflectance and transmittance for $Ge_{28-x}Se_{72}Sb_x$ (x = 0, 8, 16, 24 at.%) have been studied by Hosni *et al*. in wavelength region from 200 nm to 1100 nm [91]. The values of E_g^{opt} decrease with addition of *Sb* content.

Othman *et al.* have reported the optical properties for $As_{30}Sb_{15}Se_{55}$ composition [50]. The optical transmission and reflection spectra of these films have been measured in the wavelength range 400–900 nm. The values of α increase with an increase in photon energy and value of E_g^{opt} is 1.49 eV. Naik *et al.* have reported on the optical absorption spectra of $As_{40}Se_{60-x}Sb_x$ (with x = 0, 5, 10, 15 at.%) taken by using the Fourier Transform Infrared (*FTIR*) spectrometer in the wavelength range 400–1200 nm[92]. A clear red shift in the interference free region has been observed and E_g^{opt} decreases with increasing *Sb* content. Wang *et al.* have studied $Se_xGe_{25-x}Te_{75}$ (x = 0, 5, 10, 15, 20 at.%) glasses prepared by melt–quenching method [93]. The optical absorption edge shifts toward the lower wavelength and hence, E_g^{opt} increases with increasing *Se* content in the *Ge−Te* glass.

The optical band gap of the $As_{40}Se_{60-x}Sb_x$ films decreases while the width of localized states increases with the increase in *Sb* content [92]. Thin *As–Se–Sb* films are used as potential medium for optics and sensor applications. For $Se_xGe_{25-x}Te_{75}$ glasses the infrared cut off wavelength appears beyond 18 μm [93]. Therefore, optical band gap of the material plays a major role in the preparation of the device for a particular wavelength, which can be modified by the addition of impurity. So, the influence of metallic additives on the optical properties play an important role in case of chalcogenide glasses.

1.4.3 Quaternary chalcogenide glasses

Various quaternary chalcogenide glassy systems have been studied by researchers for Far–IR, thermal and optical properties and few compositions are reviewed below.

Petit *et al.* have studied the effect of the substitution of *S* for *Se* on the structure of the glasses in the system $Ge_{0.23}Sb_{0.07}S_{0.70-x}Se_x$ with $x = 0, 0.05, 0.10, 0.20, 0.50$ and 0.70 [94]. The progressive decrease of corner−sharing $GeS_{4/2}$ units for $0.05 < x < 0.50$ and increase of corner sharing $GeSe_{4/2}$ units and *Ge–Se–Ge* takes place when $x > 0.50$. Dahshan have reported the thermal stability and crystallization kinetics of $As_{14}Ge_{14}Se_{72-x}Sb_x$ (where $x = 3, 6, 9, 12$ and 15 at.%) glasses using DSC [95]. Reported values indicate that T_g and T_c strongly depend on heating rate as well as on *Sb* content. The values of T_g increase while E_c and the thermal stability decrease with the increase in *Sb* content.

Aly *et al.* have studied the effect of replacement of *Te* by *In* on the crystallization kinetics and the thermal stability for $Ge_{15}As_{20}Te_{65-x}In_x$ ($x = 0, 3$, and 6 at.%). Thermal properties have been studied using DSC under non-isothermal conditions [96]. The characteristic temperatures (T_g and T_c), the activation energy for glass transition and the activation energy for crystallization increase. The reported data for thermal stability criteria shows that $Ge_{15}As_{20}Te_{65}$ glass is the most stable composition of the reported compositions, and the stability follows the order $Ge_{15}As_{20}Te_{65} > Ge_{15}As_{20}Te_{62}In_3 > Ge_{15}As_{20}Te_{59}In_6$.

Kumar *et al.* have reported the glass transition kinetics for $Se_{90\,x}Te_5Sn_5In_x$ ($x = 0, 3, 6$ and 9) glassy alloys using DSC technique under non-isothermal conditions at different heating rates 5, 10, 15 and 20 K/min [97]. T_g increases while E_g decreases with increasing *In* content. The stability parameter increases with *In* content and $Se_{81}Te_5Sn_5In_9$ glass is best thermally stable glass of this series. Transmission spectra (400–1500 nm) of thermally evaporated amorphous $[(As_2Se_3)_{90}Ge_{10}]_{95}Cd_5$ and $[(As_2Se_3)_{90}Ge_{10}]_{95}Pb_5$ thin films have been used to report optical parameters by

Sharma *et al.* [98]. E_g^{opt} for $[(As_2Se_3)_{90}Ge_{10}]_{95}Cd_5$ is 1.36 eV and for $[(As_2Se_3)_{90}Ge_{10}]_{95}Pb_5$, E_g^{opt} is 2.86 eV.

Sharma *et al.* have reported for $Ge_{20}Se_{70-x}In_{10}Bi_x$ (x = 2, 4, 6, 8, 10) thin films [99]. The optical parameters have been measured using transmission spectra in the range of 400–1800 nm. Red shift has been observed with the addition of *Bi* content. The values of E_g^{opt} decrease (1.75 eV − 0.87 eV) with increasing *Bi* content. The effect of replacement of *Se* by *Sb* on the optical constants of quaternary chalcogenide $As_{14}Ge_{14}Se_{72-x}Sb_x$ (x = 3, 6, 9, 12 and 15 at.%) thin films have been reported by Dahshan *et al* [100]. The transmission spectra, $T(\lambda)$, of the films at normal incidence have been used in the spectral region from 400 to 2500 nm to determine E_g^{opt} values. The values of E_g^{opt} decrease from 1.72 to 1.56 eV.

Aly has studied the optical constants for *Ge–As–Te–In* amorphous thin films evaluated from their reflectance spectra [101]. The reflection spectra, $R(\lambda)$, of the films have been taken in the spectral region from 400 to 2500 nm. With the addition of *In* content, E_g^{opt} decreases. Ahmad *et al.* reported the optical transmission spectra of $Sn_{10}Sb_{20-x}Bi_xSe_{70}$ ($0.6 \leq x \leq 6.8$) thin films in a range 400–2500 nm [102]. The values of refractive index and absorption coefficient decrease with an increase in wavelength. The optical band gap initially increases with *Bi* content (for x = 2) and then decreases sharply for higher *Bi* concentrations.

1.5 Applications of chalcogenide glasses

Chalcogenides provide a versatile platform for various optical and thermal applications. Chalcogenide glasses can be formed with a wide range of compositions and doped with additional elements to provide further functionality. These glasses are well known for their transparency far into the infrared region, and are widely used in infrared optical components. Chalcogenide glasses have found a number of applications for optical devices, particularly in fiber form. Other applications are optical limiter devices, remote sensing etc. Thermal properties of glasses are vital due to their applications in the study of the glass-crystal transformation. Memory and threshold devices are some of the applications of thermal properties. An illustration for the application domain of chalcogenide glasses is given in Figure 1.3. Few of the applications of chalcogenide glasses are discussed in detail below.

Optical limiting is used to protect sensitive detectors from high power laser fire. Current interest for optical limiting is in the area of defense. High intensity blasts from infrared lasers can destroy the sensitive detectors used for guidance and military surveillance [103]. The devices can be protected against pulses by placing a nonlinear optical material in front of the detector. Such a material must be transparent to low intensity infrared light in the wavelengths of interest, but must react to high intensity threats. High non–linear refractive index materials are suitable for optical limiting [104, 105].

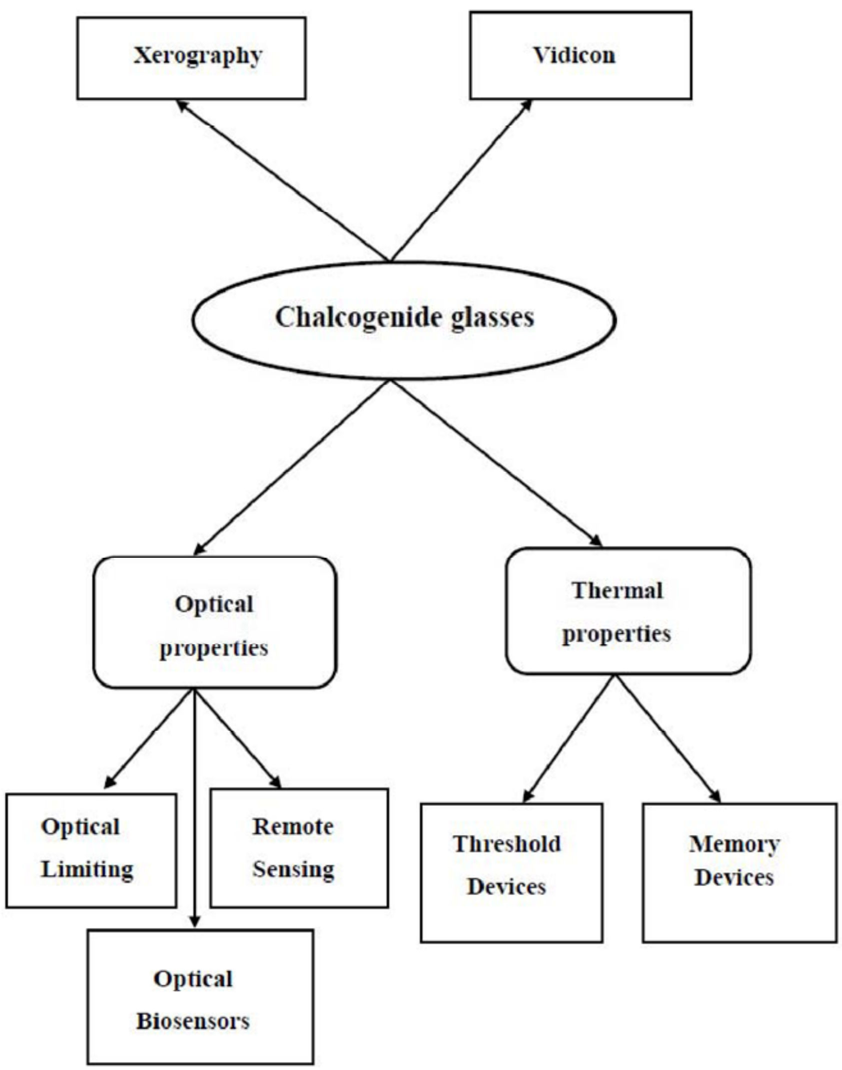

Figure 1.3 Applications of chalcogenide glasses in various fields.

The chalcogenide glasses possess appropriately large nonlinear optical responses and have excellent transparency over the entire infrared range with windows typically extending from less than 1 μm to greater than 12 μm in wavelength. Another importance of such material is transparency in the atmospheric windows of 3 to 5 μm and 8 to 14 μm, the two regions where atmospheric absorption is minimum. These two regions are important for remote detection, infrared imaging and night vision. Only impurity scattering reduces the transparency of chalcogenide glasses in these regimes, and that can be controlled by careful processing and improved purification methods.

Optical fibers containing chalcogenides have remarkable properties and play an important role in the development of optical biosensors [106]. Chalcogenides are matchless materials for the fabrication of core–clad structure. Due to wide optical window in the IR regime, chalcogenides are attractive candidates for sensing the fingerprint region of bio−molecules including proteins, nucleic acids, lipids, and carbohydrates [107]. Chalcogenide fibers are used to monitor the viability of live human lung cells by recording their IR spectra continuously over time after exposure to compounds inducing genotoxic or cytotoxic effects. This system can then be used to detect the presence of small quantities of toxic agents by monitoring the cell response through changes in their infrared spectra.

Remote sensing concerns with the activities such as recording or observing or sensing objects at far–off places. For example, the Darwin mission aims at directly analyzing extra solar earth like planets in order to detect signs of life in these exoplanets [59]. The main biological molecules of life are the water, ozone and carbon dioxide. Global warming is increasing day by day and greenhouse gas such as CO_2 is responsible for this. Therefore, detection of CO_2 in the earth's atmosphere has become important topic of research to analyze environmental processes. Remote optical detection of CO_2 involves monitoring of its two vibrational absorption bands at 4.3 and 15 μm and therefore, requires advanced infrared technologies. Chalcogenide fibers are well suited for applications in remote sensing and spectroscopy.

Memory and threshold devices are based upon the tendency of material to crystallize. Memory switches come from the boundaries of glass forming regions where glasses are more prone to crystallization. The glasses that are easily devitrified undergo memory switching on the other hand stable glasses show threshold behavior [32, 34, 37, 108]. The tendency of glasses to crystallization is determined by the difference between the temperatures of crystallization and glass transition. Glasses having small difference between crystallization and glass transition temperature behave as memory device. Chalcogenides show these behaviors and hence, can be used as data storage devices.

1.6 Motivation of thesis work

Extensive research in the field of chalcogenide glasses started in 1950, motivated particularly by their exceptional optical transmission in the infrared region. These glasses are having high atomic mass that indicates the vibrational absorption bands take place around 8μm for sulphide glasses; at ≈14μm for selenides; and up to 25μm for tellurides. As these glasses are less robust compare to oxide glasses and hence, are attractive for glass molding to produce optical elements such as lenses. Glass densities are high and combined with strong polarizability of the bonds, leads to a large index of refraction.

Among chalcogenides*,* *Se* is characterized with high viscosity and hence, has good glass forming ability. This makes *Se* a good host matrix for investigation both as bulk and thin films. However, *Se* has some disadvantages such as short lifetime and low sensitivity. This problem can be overcome by alloying *Se* with other elements, such as *As*, *Sb* and *Pb* etc [26, 27, 39, 48]. *Ge* has been chosen as an additive due to its high sensitivity, greater hardness, high crystallization temperature and smaller ageing effects [40]. Germanium based glasses especially, *Ge–Se* alloys, are the best glass formers in chalcogenide family with *Ge* content less than 33 at.%. These alloys are environment friendly and hence, replace environmentally unsafe *As–Se* glasses in various devices such as waveguide sensors [109]. Various authors have reported for *Ge-Se* systems for the study of structural, thermal and optical properties [25, 28, 32, 36, 49, 52]. As the transmission window of *Ge–Se* alloys is limited to mid infrared region, these glasses cannot fulfill the criteria for the fabrication of useful devices which need Far–IR transparency, due to which third element addition is needed. Addition of third element *viz.* *Sn*, *In*, *Bi* in *Ge–Se* system has been reported by various authors [25, 75, 82, 84]. *Sb* has been selected as third element due to its high electropositive character that may affect the optical properties of the system and hence, can be explored for various optical devices. When *Sb* is added to *Ge–Se* binary system, chains get crosslinked and glasses get strengthened. So, *Sb* has a potential to increase the glass formation region and also creates the configurational changes in the system. But, with increasing content of *Sb* the tendency towards the crystallization increases [110]. Further, *Te* is added to *Ge–Se–Sb* alloy, as this improves and enhances the IR transmission region. *Te* element is heavy so, there may be reduction of energy loss (due to multiphonon absorption) and hence, absorption edge may shift towards the longer wavelength.

This thesis reports the work that has been carried out on two chalcogenide systems *viz.* ternary and quaternary glasses and their thin films. In ternary *Ge–Se–Sb* glasses, the composition $Ge_{19}Se_{81-x}Sb_x$ has been expanded by replacing *Se* with *Sb* from 4 at.% to 20 at.%.

The physical, structural, thermal and optical properties for $Ge_{19}Se_{81-x}Sb_x$ (x = 0, 4, 8, 12, 16, 17.2, 20) system has been investigated systematically. Bonding arrangements and structural study of $Ge_{19}Se_{81-x}Sb_x$ (where x = 0, 4, 8, 12, 16, 17.2, 20) glassy alloys have been carried out using Far–IR transmission. Thermal stability and crystallization kinetics have been studied under non–isothermal conditions using differential thermal analysis for *Sb* alloyed *Ge−Se* system. UV–Vis–NIR spectrophotometer has been used for the study of optical parameters like refractive index, absorption coefficient, optical band gap etc.

In quaternary *Ge–Se–Sb–Te* glasses, composition $Ge_{19-y}Se_{63.8}Sb_{17.2}Te_y$ has been extended with the replacement of *Ge* with *Te* from 2 at.% to 10 at.%. Impurity effects in chalcogenide glasses have importance in the formation of glassy semiconductors. These impurity atoms are supposed to satisfy all the valence requirements when they enter the glassy network. The effect of impurity atoms in chalcogenide glasses depend upon the composition of the glasses as well as the chemical nature of impurity which ultimately affects the various properties. Thus, the study of physical, structural, thermal and optical properties plays crucial role to have better understanding of the system. Several physical parameters *viz.* average coordination number; lone pair of electrons, mean bond energy, glass transition temperature, cohesive energy, energy gap, density for $Ge_{19-y}Se_{63.8}Sb_{17.2}Te_y$ (y = 0, 2, 4, 6, 8, 10) have been studied. In Far-IR study; various absorption peaks are observed and formation of bonds are discussed. Thermal and optical properties for *Te* incorporated *Ge−Se−Sb* system have been investigated.

CHAPTER 2

Theoretical background

A short theoretical background has been presented in this chapter. This includes the basic structural models for chalcogenide glasses. Thermal parameters such as activation energy of glass transition temperature and crystallization are also discussed. Brief introduction of optical properties is given along with the models used to calculate various parameters.

2.1 Structural models

Long range order is absent in amorphous material that indicates lack of translational periodicity [111, 112]. The disorder is not complete on the atomic scale as the atomic scale structure implies order for few interatomic distances about any considered atom [112]. The structure of amorphous material is ambiguous, and specified in three stages: (i) the atomic co–ordination of each constituent (ii) the bond distribution (iii) the molecular cluster of network forming groups of atoms [1].

Structural models play a significant role in order to understand the nature of amorphous materials. Zachariasen proposed the first ideal model for inorganic covalent glasses, the Continuous Random Network (CRN) model [1]. This model is a basis for all structural models and later on, number of models has been proposed to explain various structure linked properties of glasses. He proposed some rules while building the model which are: (i) nearest neighbor distance (bond length) is constant or nearly same; (ii) the main reason of randomness comes from the significant spread in bond angles; (iii) there is more flexibility in covalent bond angles of two fold coordinated elements and least in three fold coordinated atoms. This model considers the structure to be "ideal" that indicates no defects such as dangling bonds and voids. This is not sufficient to describe the characteristics observed in medium range order and hence, the application of CRN model is limited to short range order.

The structure of chalcogenide glasses can be explained more appropriately using two models that are based on the distribution of bonds in covalent network. These two models are; Random Covalent Network Model (RCNM) and Chemical Ordered Covalent Network model (COCN) [113, 114]. These two models satisfy the 8-V_a rule which says that in stable covalent glasses, number of valence electrons (V_a) of particular atom is coordinated in such a way that the outer shell is filled with eight electrons [115]. The basic difference between these two models is based on the approach of distribution of bonds.

RCNM deals with the distribution of all possible bonds that are based on the local coordination and concentration of constituent elements [113]. This model is based on pure statistics rather than other factor "relative bond strength" and is applicable for all compositions. For A_xB_{1-x} binary system where *A* and *B* are elements belong to different column in periodic table and *x* is normalized concentration variable, the network structure is determined by various factors such as the local coordination of *A* and *B*, the distribution of bond types *A–A*, *A–B* and *B–B* and the topological rules for the interconnection of the molecular building units [116, 117]. This model gives equal preference to *A–A*, *B–B* and *A–B* bonds for all compositions except at $x = 0$ and $x = 1$. Luckovsky *et al.* studied the chemical order for *Ge–Se*, *Ge–S*, *As–S*, *As–Se* binary compositions employing Infrared and Raman spectroscopy to give the structural information in bulk form of these glasses [15]. From the vibrational spectra of *Ge−Se* alloy, *Se* chains and $GeSe_4$ tetrahedra are observed when *Ge* composition is up to 33 at. %. Raman spectroscopy gives the information for the presence of ethane Ge_2Se_4 molecular structure when *Ge* > 33 at. %. Figure 2.1 shows the molecular cluster in *Ge–Se, Ge–S* and *As–Se, As–S* systems for both *Ge* or *As* rich and *S or Se* rich regime. RCN model predict that 25 % of *Ge–Ge* bonds are formed near the stoichiometric composition but vibrational spectra propose that such type of bonds are observed after exceeding stoichiometric composition.

COCM model is based on the relative bond energies and formation of heteropolar bonds *A–B* rather than homopolar *A–A* or *B–B* bonds [114]. This model is applicable for $Ge \leq 1/3$, *i.e.* for *Se* rich composition and assumes that *Ge* atoms are introduced into *Se* matrix and cross link the two fold coordinated chains through four fold coordinated *Ge* site. There exists a completely ordered network that takes place at composition, $X_c = M_B/(M_B + M_A)$, where M_A is coordination number of *Se* and M_B is coordination number of *Ge*. For *B*–rich alloy region, which contains *A–B* and *B–B* bonds, the compositional range is given as $X_c < x \leq 1$ whereas for *A*–rich alloys with *A–B* and *A–A* bonds having range $0 \leq x < X_c$.

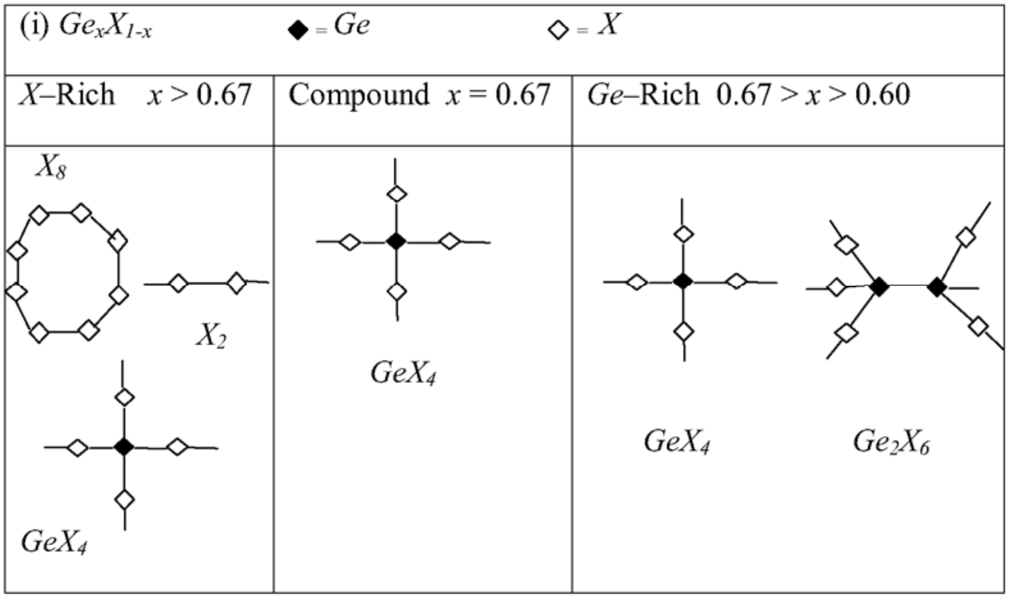

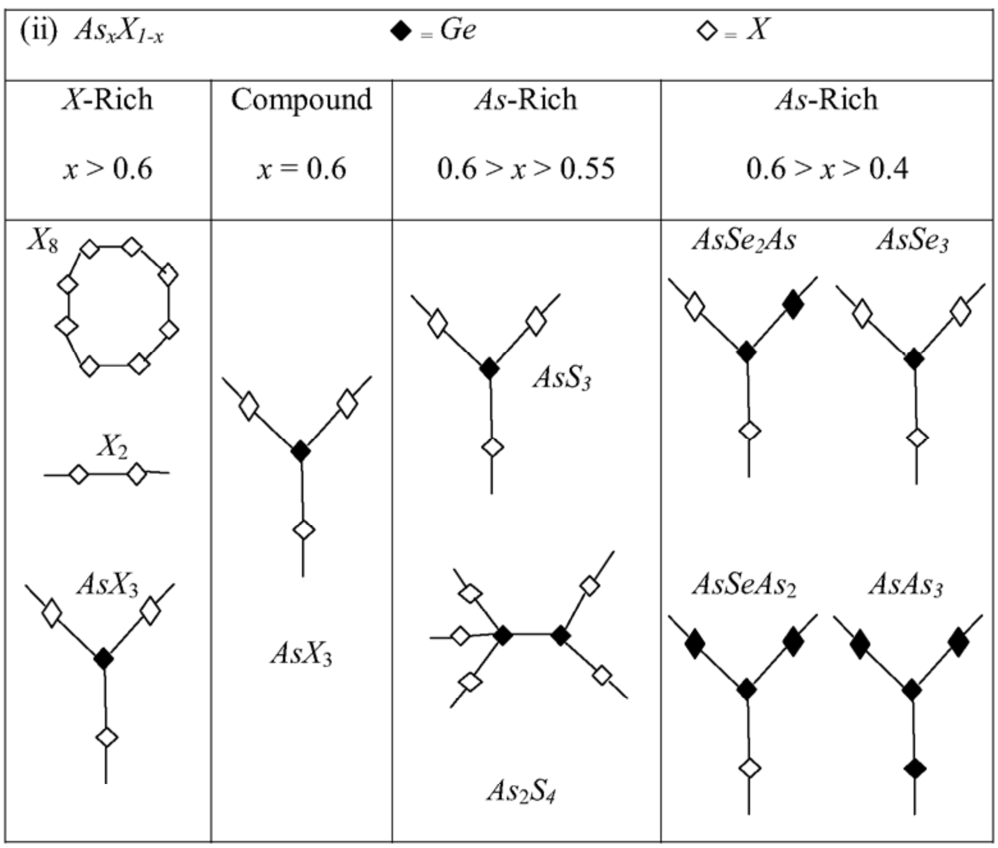

Figure 2.1 A schematic representation of the molecular structures in the alloys (i) $Ge_{1-x}X_x$ ($X = Se, S$) (ii) $As_{1-x}X_x$ ($X = Se, S$)

This model was initially applied to $Ge_{1-x}Te_x$ and $Ge_{1-x}Se_x$ alloys, in which chalcogen element was considered as to form chain like structure rather than rings. For *Se* containing systems, the bonding tendency is toward ring formation and the statistics of bonds also not change by considering ring formation. This may be explained by considering solid as a solution of rings in the network structure that includes GeS_4 tetrahedra. After evaluating these results, Luckovsky *et al.* concluded that COCM is best to explain the structure of *Ge−Se* alloys [116].

2.2 Thermal analysis

Thermal analysis is a measurement which shows the change of substance in terms of its physical and chemical properties with variation in temperature [118]. Thermal changes in substance are due to exothermic or endothermic enthalpic transition or reactions which are caused by phase changes, vaporizations etc. Phase transitions, dehydration, reduction and some decomposition reactions are endothermic effects while crystallization, oxidation and some decomposition reactions are exothermic effects [119]. Amorphous solids are thermodynamically unstable and have tendency to relax towards equilibrium [120]. Upon cooling a liquid below its melting point, does not crystallize but become a super cooled liquid. With further decrease in temperature, a stage comes called as glass transition temperature (T_g), below which the viscosity of material increases by many orders and become glass [121]. Figure 2.2 shows the volume versus temperature curve of a material which can either form glass or crystallize.

On cooling the liquid, there is an abrupt but continuous change in slope of specific volume (change in thermal expansion coefficient). Along with the specific volume there is a continuous change in specific heat also and the temperature at which these properties change is denoted as glass transition temperature [122]. Good glass is that in which cooling rate is greater; sample volume is small and slower crystallization rate [122]. At temperature near or somewhat below glass transition temperature (T_g), molecular mobility is not quite zero but there is slow and gradual approach to equilibrium which is called physical aging [123]. It is observed that aging effect eliminates after heating above T_g [120]. Aging indicates there is gradual continuation of vitrification around T_g and material behaves more and more glass like rather than liquid. Physical aging is very important phenomenon at which many properties of the material changes and various mechanical parameters such as stress, strain, enthalpy and many more can be determined. Aging is important in testing of plastics in order to predict the long range behavior [123].

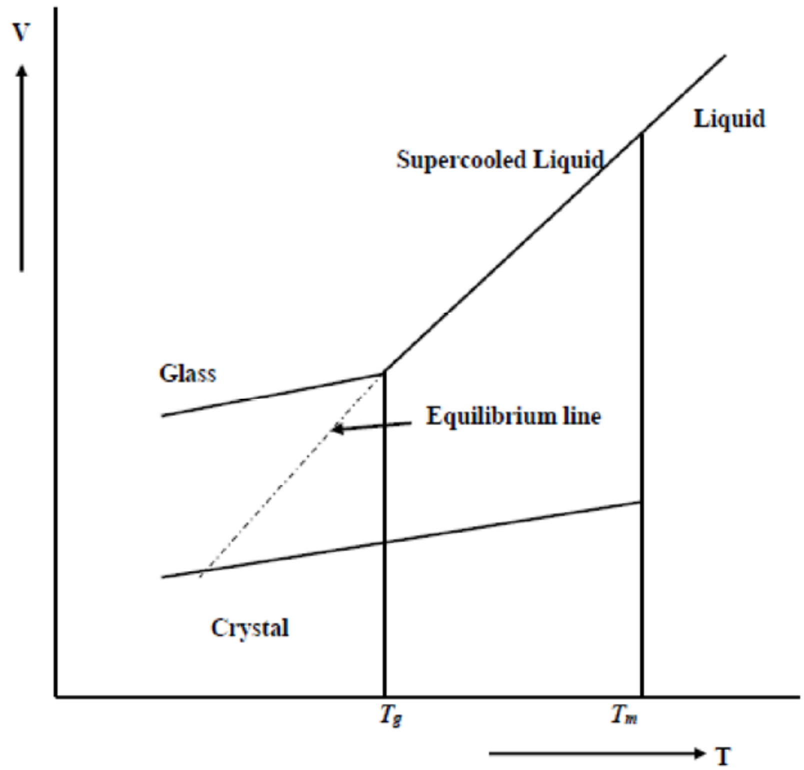

Figure 2.2 Schematic illustration of volume (V) versus temperature (T) curve: transition from the crystalline state to glassy state.

Glasses can be analyzed by doing calorimetric measurement which gives the information about thermal properties such as kinetics of crystallization, thermal stability etc. Here some methods are explained to study the glass transition and crystallization kinetics in terms of activation energy of glass transition and activation energy for crystallization.

Moynihan *et al.* have studied dependence of the glass transition temperature on heating and cooling rate [124]. Experimental measurement of glass transition temperature versus heating or cooling rate was performed for As_2Se_3, B_2O_3, potassium silicate and borosilicate crown glasses. Higher values of T_g are observed for faster cooling and heating rate. Glass like behavior is observed in a temperature range where structural relaxation becomes too slow so that it ceases and hence crosses the glass transition or transformation range. So, glasses always relaxed towards the direction of equilibrium. Activation energy for glass transition temperature is given as;

$$\frac{d(\ln \gamma)}{d(1/T_g)} = \frac{-E_g}{R} \tag{2.1}$$

where E_g is activation for glass transition, R is universal gas constant, γ is heating rate.

When there is a reaction in differential thermal analysis then a peak or deflection occurs which indicates that thermal properties of sample changes. Plot between $\ln \gamma$ and $1000/T_c$ is linear for most glasses and slope gives the activation energy for crystallization and equation is expressed as [125, 126];

$$\ln\left(\frac{\gamma}{T_c^2}\right) = const. - \frac{E_c}{RT_c} \tag{2.2}$$

While this equation is originally derived for crystallization process, but later on it was also suggested for glass transition work and equation took the form as [127];

$$\ln\left(\frac{\gamma}{T_g^2}\right) = -\frac{E_c}{RT_g} + const. \tag{2.3}$$

Mahadevan *et al.* have studied the thermal analysis on eight glasses of $As-Se-Sb$ system [128]. Study of As_2Se_3 alloys reveals that there is no change in thermal properties for bulk chunk and crushed powder. This infers that glass transition temperature and crystallization temperature are independent of particle size [128]. Activation energy gives the indication of speed in crystallization and equation can be written as [128];

$$\ln(\gamma) = -\frac{E_c}{RT_c} + const. \tag{2.4}$$

The equation (2.4) has derived from Kissinger method of crystallization.

The activation energy of crystallization (E_c) can also be determined by an approximation method developed by Augis and Bennett [129]. The relation can be expressed as;

$$\ln(\gamma/T_c) = -E_c/RT_c + \ln K_o \tag{2.5}$$

where R is universal gas constant, γ is heating rate and K_o is pre–exponential factor.

2.3 Optical properties of chalcogenide glasses

Chalcogens occupy six electrons in their outer valence shell, where *s* shell is filled with two electrons and one of the *p* shells, considered as nonbonding; have electron pair and other two shells having one electron in each. The two unfilled states of *p* orbitals are used in the formation of chemical bonds and hence, form two covalent bonds. Two bond forming ability makes atomic structure of chalcogens flexible. From the Figure 2.3, it can be seen that valence band consist of states with *p* bonding (σ') and lone–pair (LP) orbitals.

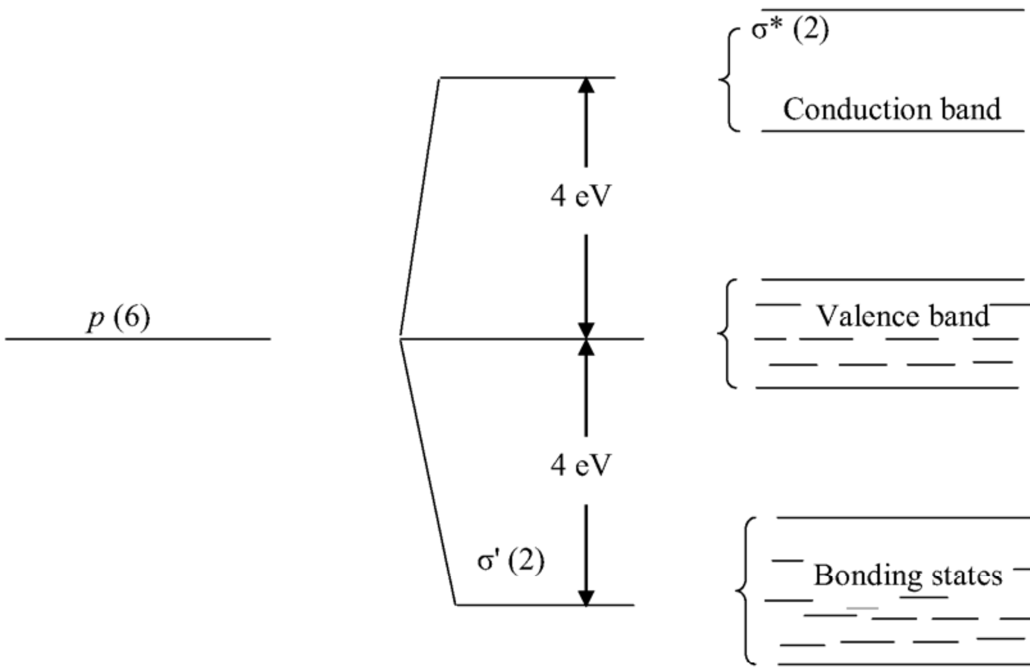

Figure 2.3 Band structure of chalcogenide glass given by Kastner [130].

The unshared electrons have higher energy than bonding electrons, so the LP orbitals occupy the states at the top of valence band. The role of valence band is then played by LP band and bonding band is no longer behaved as valence band [130]. The conduction band is formed by antibonding (σ*) band. The LP lies between the σ' and σ* and the occupied states fall into σ' band while unoccupied states form acceptor band above LP [130]. Chalcogenides are also called as lone–pair semiconductors because their electrical properties are determined by lone pair band [130]. When light interacts with the chalcogenide glasses the impact is profound on two properties;

electronic and vibrational structure of material. Electronically chalcogenide glasses behave as semiconductors due to their similar band gap. The presence of disorder in network creates the localized states in forbidden gap. These states play a significant role in electrical and optical properties of chalcogenide glasses. As the chalcogenide glasses comprise of heavy atoms due to which phonon vibrations with low energies take place. Lightweight materials such as silica glasses have strongly bound atoms; consequently phonon vibrations with high energies take place.

2.3.1 Different regimes of light and its absorption

Light is divided into different regions on the basis of wavelength or energy of photons when interacts with matter. The various regions of light are; ultraviolet (0.01 μm – 0.39 μm), visible (0.39 μm – 0.78 μm) and infrared (IR) having different wavelength ranges. The IR region is often subdivided in four regions; the near–IR (0.78 μm – 3 μm), intermediate–IR (3 μm – 6 μm), Far–IR (6 μm – 15 μm) and extreme–IR (15 μm – 1 mm) [131, 132]. Molecular vibrations and lattice vibrations in solids strongly absorbs Far–IR wavelength and this regime is important for the thermography and infrared imaging. This is due to the fact that black body at room temperature radiates energy at 9.89 μm of wavelength

Matter is an aggregation of atoms, which are composed of electrons, protons and neutrons. In material, photons interact with charged particles. The interaction between light with matter is considered as the function of dielectric response in the material which is also called complex dielectric response. The dielectric response can be computed from the knowledge of atomic and electronic dipoles present in material. Visible and infrared properties of materials are affected by the electronic, atomic and orientational dipoles [133]. The electronic dipoles are distortions of electric field surrounding the atoms of material. When there is a motion of positive and negative ions due to external electric field then atomic dipoles forms. Orientational dipoles occur when molecular dipoles rotate to align with applied electric field and such kind of dipoles are observed in gases and liquids. Two models are discussed here for the calculation of various optical parameters. Before starting those models it is important to give background of some of the significant optical parameters. These parameters are; refractive index, transmittance, absorbance and reflectance.

2.3.2 Brief background of optical parameters

2.3.2.1 Refractive index

In optics, when photon interacts with matter then it can alter the phase of photon due to which change in the direction of propagation of light occur and is said to be refraction of light. The refractive index of material is defined as the ratio of velocity of light in vacuum to velocity of light in medium. Photons absorbed and re−emitted by molecules which causes the speed of light to be slowed down. This slowness is represented in Maxwell's equation where μ, ε and σ parameters play role and deviate from their free space values [134]. Refractive index can be written as

$$n = \left(\frac{\varepsilon\mu}{\varepsilon_o \mu_o} \right)^{1/2} \tag{2.6}$$

where μ and ε are permittivity and permeability in medium and μ_o and ε_o are permittivity and permeability in vacuum respectively.

2.3.2.2 Transmittance, absorbance and reflectance

Optical properties of chalcogenide glasses have been studied from the last two decades since these materials are characterized by high transparency in near and medium infrared range and used in optical devices [135]. When a beam of light passes through a medium it is partially transmitted, partially reflected and partially absorbed. Transmission is the property of a substance to permit the passage of light, with some or none of incident light being absorbed in the process. It has been shown that the impurity absorption bands have limited the IR transmission of chalcogenide glasses [136]. These absorption bands can be removed so that the useful range of transmission is extended. Transmittance (T) of any system at high values of absorption coefficient (α) can be given as:

$$T = \left(1 - R'\right)^2 \exp(-\alpha t) \tag{2.7}$$

where R' is reflectance, t is the film's thickness and α is absorption coefficient.

As the beam of light passes through an absorbing medium, the amount of light absorbed is proportional to the incident light times the absorption coefficient. Absorption occurs when electric field of a light wave interacts with absorbing atoms or molecules in an oscillating dipole interaction.

The absorbance (A) or optical density can be written as:

$$A = \log_{10}(I_o/I) \tag{2.8}$$

where I is the transmitted light and I_o is the incident intensity. The higher the optical density of the system the lower will be the transmittance.

Reflectance (R') is the ratio of the total amount of radiation reflected by a surface to the total amount of radiation incident on the surface. When a beam of light is incident on a medium at a normal incidence then the reflectance is given by a relation:

$$R' = \frac{(n-1)^2 + k^2}{(n+1)^2 + k^2} \tag{2.9}$$

where n is the refractive index and k is the extinction coefficient of the material. Further, Swanepoel and Wemple Di−Domineco models give a detail insight to understand the optical properties of thin films.

2.3.2.3 Swanepoel model

This model is based on transmission of incident light from which refractive index (n), thickness (t), absorption coefficient (α) and extinction coefficient (k) of thin film can be calculated [137, 138]. Using transmission and reflection spectra, the refractive index and absorption coefficient can also be determined [139−141]. But, from Swanepoel's model, n and α can be determined from transmission spectra alone.

Consider a thin film on transparent substrate with thickness t and complex refractive index $n^* = n - ik$, where n is real part of refractive index and k is extinction coefficient (Figure 2.4). The transparent substrate has a thickness several orders of magnitude larger than t and has index of refraction s with zero absorption coefficient. If the film thickness is not uniform, then the interference effects are destroyed and transmission is a smooth curve rather than full spectrum [137]. As a reference the full spectrum obtained for a thin film with uniform thickness is shown in Figure 2.5. The spectrum is divided into four regions. In transparent region where $\alpha = 0$, transmission is determined by n and s through multiple reflection. Next is weak absorption region where α is very small and transmission starts to reduce. In medium absorption region, α is large and transmission decreases. Last region is strong absorption region, where transmission decreases drastically.

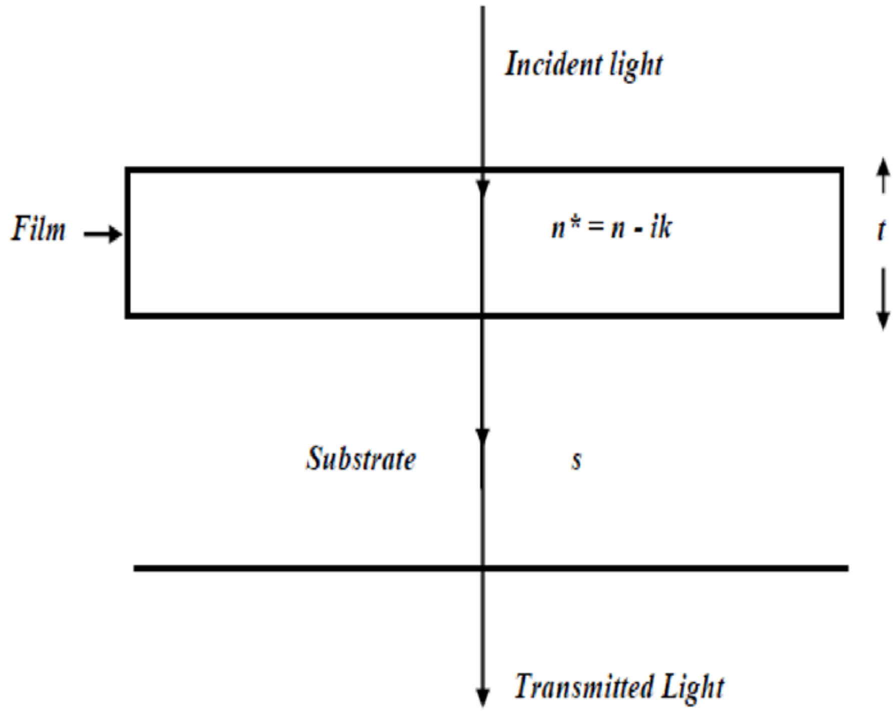

Figure 2.4 System of an absorbing thin film on a thick finite transparent substrate.

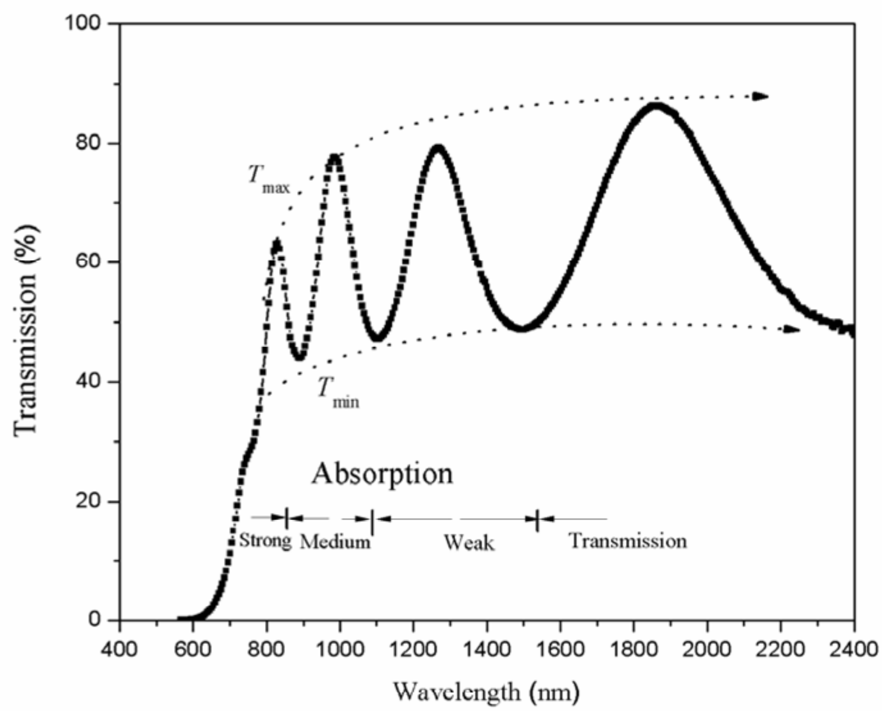

Figure 2.5 Different absorption regions in the transmission spectrum.

As the extremes of interference fringes are observed leading to continuous envelops. These envelops are formed through the maximum transmittance (T_{max}) and minimum transmittance (T_{min}) data. So, T_{max} and T_{min} are considered as the continuous function of wavelength. Advantage of this method is that the envelope is a slowly changing function with wavelength as compared to direct spectrum where transmittance varies rapidly with wavelength. Refractive index for the thick substrate is given as;

$$s = \frac{1}{T_s} + \left(\frac{1}{T_s} - 1\right)^{1/2} \qquad (2.10)$$

where T_s is interference free transmission for substrate and is expressed as;

$$T_s = \frac{2s}{s^2 + 1}$$

In the region of weak and medium absorption, refractive index is given as;

$$n = \left[N + \left(N^2 - s^2\right)^{1/2}\right]^{1/2} \qquad (2.11)$$

where

$$N = 2s\frac{T_{\max} - T_{\min}}{T_{\max}T_{\min}} + \frac{s^2 + 1}{2}$$

The values of n can also be estimated in other parts of spectrum by extrapolating the n which is calculated using above equations. The values of refractive index can be fitted to Cauchy dispersion relationship to obtain n in other part of spectrum [137];

$$n = a + \frac{b}{\lambda^2} \qquad (2.12)$$

where a and b are material dependent Cauchy's constants. Once refractive index is known, the absorbance (A) can be calculated;

$$A = \frac{E_M - \left[E_M^2 - (n^2 - 1)^3 (n^2 - s^4)\right]^{0.5}}{(n-1)^3 (n - s^2)} \qquad (2.13)$$

where

$$E_M = \frac{8n^2 s}{T_{\max}} + (n^2 - 1)(n^2 - s^2)$$

Extinction coefficient (k) is a measure of fraction of light lost due to scattering and absorption per unit distance of participating medium;

$$k = \frac{\lambda}{4\pi t} \ln(1/A) \tag{2.14}$$

If n_1 and n_2 are the refractive indices of two adjacent maxima or minima at wavelengths λ_1 and λ_2 respectively, then the thickness t of the film is given by

$$t = \frac{\lambda_1 \lambda_2}{2(\lambda_1 n_2 - \lambda_2 n_1)} \tag{2.15}$$

2.3.2.4 Absorption coefficient and optical band gap

Absorption coefficient (α) is a fundamental property of material. It defines the extent to which material absorbs energy. In a material with low absorption coefficient light is only poorly absorbed, and if the material is thin enough it will appear transparent to that wavelength. Interaction of light with film deposited on the substrate has been shown in Figure 2.4. The absorption coefficient depends on the material and also on the wavelength of light which is being absorbed. The absorption coefficient (α) is related to the extinction coefficient (k) by the relation:

$$\alpha = \frac{4\pi k}{\lambda} \tag{2.16}$$

where λ is the wavelength and absorption coefficient in the units of cm^{-1}.

The high absorption region having indirect interband transitions between valence and conduction bands, absorption coefficient is given as [144]:

$$\alpha = \frac{B\left(h\nu - E_g^{opt}\right)^p}{h\nu} \tag{2.17}$$

where E_g^{opt} is the optical band gap and B is a constant which measures the extent of band tailing. In the above mentioned equation, p = 1/2 for a direct allowed transition, p = 3/2 for a direct forbidden transition, p = 2 for an indirect allowed transition and p = 3 for an indirect forbidden transition. The optical band gap of the semiconductor can be determined using fundamental absorption called band to band transition. In this transition, photon is absorbed and excitation of electrons from valence band to conduction band takes place. The threshold at low energy side of the optical absorption spectra is called optical absorption edge.

There are two possible transitions; direct and indirect. In direct gap transition, the lowest point in the conduction band lies directly above the highest point in the valence band whereas in an indirect transition, the lowest point in the conduction band is not directly above the highest point in the valence band. Indirect gap transitions are much weaker and such type of transitions are not possible with photon only. A phonon, *i.e.*, quantum mechanical particle associated with the vibrations of the crystal lattice, is required for such type of transitions [142].

Optical absorption edge corresponds to separation in energy between bottom of conduction band and top of the valence band. By plotting the graph between α and $h\nu$, absorption edge can be obtained. From the Figure 2.6, one can see the three parts X, Y, Z of the absorption edge [143].

a) High absorption region

Part X is the high absorption region with $\alpha > 10^4$ cm^{-1} and dependence of absorption coefficient on photon energy can be seen from Tauc plot (Figure 2.7) where relation between $(\alpha h\nu)^{0.5}$ and $h\nu$ is given. Slope of Tauc edge, called energy tailing parameter depends on the width of localized states in the energy gap which is in the order of 10^5 to 10^6 $cm^{-1}eV^{-1}$. Part X of the absorption curve is associated with the transitions from localized valence band states into delocalized conduction band states above mobility edge of conduction band (E_c^m) or vice-versa. The density of states such as localized and delocalized is given by the model called CFO [144].

b) The exponential region of the absorption edge

Part Y of the absorption edge is the exponential region and extends over 4 orders of magnitude of α. It has following properties:

1. The absorption constant range is from 1 cm^{-1} to about 10^4 $cm^{-1}$and formula can be expressed as;

$$\alpha(\nu) = \exp\left(\frac{h\nu}{E_g}\right) \tag{2.18}$$

2. The energy characterizing the slope is almost temperature independent at low temperatures.

3. At high temperature, the slope decreases with the temperature.

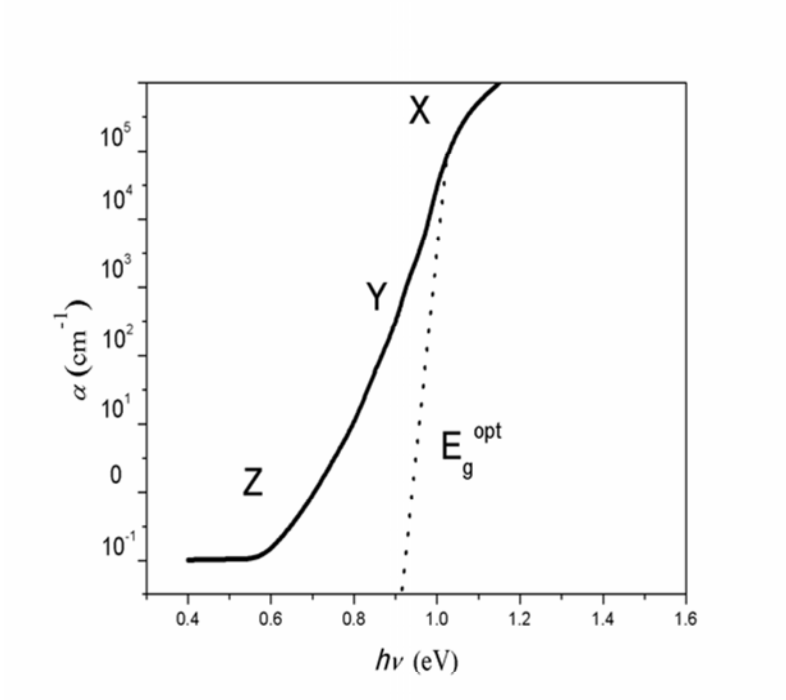

Figure 2.6 The illustration of absorption edge with its various parts.

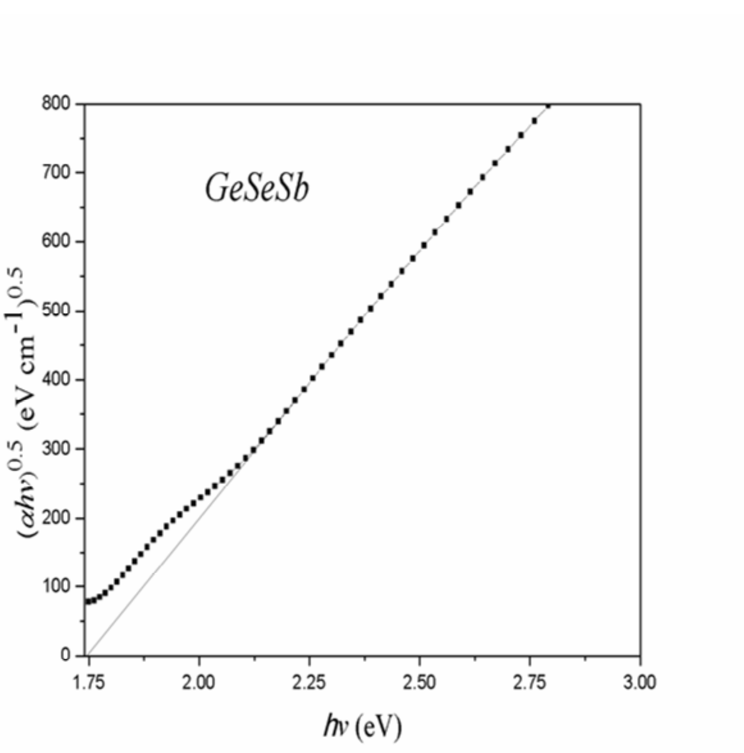

Figure 2.7 The dependence of $(\alpha h\nu)^{0.5}$ on photon energy from which optical band gap is determined.

From Figure 2.7, the tails of band state densities extending into the gap tells that the electron states in these tails are localized. These tails are referred as Urbach tails or Urbach edge.

c) Weak absorption region

Part Z that lies below the exponential region in absorption edge, shows an absorption tail. Weak absorption tail is difficult to study in thin films due to the low absorption level.

2.3.2.5 Wemple Di–Domineco model

The refractive index behavior for various solids and liquids were discussed by Wemple and Di–Domineco (WDD) using single–effective–oscillator approach [145]. Later on, same model applied to amorphous semiconductors to discuss dispersion of refractive index [146] and expression is given below;

$$n^2 - 1 = \frac{E_d E_o}{E_o^{\ 2} - (h\nu)^2} \qquad (2.19)$$

where E_o is single oscillator energy or average energy gap, E_d is dispersion energy, hν is photon energy. Parameter E_d measures the strength of interband transition and it obeys simple empirical relationship [146]

$$E_d = \beta' N_c' Z_a N_e \qquad (2.20)$$

where β' is two valued function *i.e.* for ionic and covalent materials. Ionic value is taken as 0.26 ± 0.03 eV and covalent value is 0.37 ± 0.04 eV. $N_c^{'}$ is the coordination number of the cation nearest neighbor to anion and N_e is effective number of valence electrons per anion. Z_a is formal chemical valency of anion. E_d is independent of E_o which indicates that oscillator strength quantity does not depend upon the energy parameter. This model implies that E_d does not depend on the volume density of valence electrons (internuclear spacing) [146]. The special attention is given to lone–pair electrons in disordered materials and concluded that the decrease in E_d is due to reduction in oscillator strength of lone–pair electrons to conduction band transition [146]. There is an inefficient packing in amorphous glasses *i.e.* energy difference is not a main focus of the work but interested parameter is coordination number. For tetrahedrally bonded materials, refractive index as well as E_d are not affected by loss of long range order.

CHAPTER 3

Experimental and technical details

This chapter describes the methods used to synthesize amorphous materials in bulk as well as in thin film form. The characterization techniques used to study the bulk and thin films have also been discussed.

3.1 Bulk glass synthesis

Melt quench is a simple and convenient technique for the synthesis of glassy alloys. Quenching can be done using different sources such as dry ice–alcohol mixture, liquid nitrogen and ice water. For the formation of glass, cooling must be sufficiently fast to prevent crystal nucleation and growth. The marked characteristics of melt quench technique are that the amorphous solid is formed through continuous hardening, *i.e.*, increase in viscosity of the melt and has large flexibility for wide range of compositions. Fischer and Krebs [147] expressed that for synthesis of chalcogenide glasses, following facts should be considered. (i) To obtain homogeneous melt, frequent agitation of melt is required. (ii) The vapor pressure of *Se* increases quickly at higher temperatures, so temperature should be raised in steps. Ampoules must be sealed at high vacuum, as chalcogens are prone to the oxidation. For the preparation of glasses, heating schedule depends upon the melting point as well as on the vapor pressure of the constituents. The slow heating rate *i.e.* 3–4 ^{o}C/min is required. If it is not so, then the vapor pressure of chalcogens become very high and hence, this could break the ampoules.

Chalcogenide glasses in bulk form have been synthesized using high purity elements. The quartz ampoules have been cleaned first with chromic acid. Elements have been weighed in the batch of 4 g according to their atomic weight percentages. After batching, the quartz ampoule have been sealed by an oxy fuel burner, while being evacuated to a vacuum ~ 10^{-4} Pa. For melting, the sealed ampoule have been transferred to an electric furnace and heated gradually in steps. The synthesis of glasses has been done after holding the molten mixture for several hours at melting point of constituents [148]. These ampoules have been frequently rotated to make the melt homogeneous [149]. Finally, the ampoules containing melts have been taken out from the furnace and quenched into ice cold water. Ampoules have been kept in H_2O_2 + HF solution for twenty four hours, so that sample can easily be separated from the ampoules. Then, the bulk glasses have been taken out by breaking the ampoules.

3.2 Thin film deposition

A thin film may be defined as a solid layer having a thickness varying from a few Å to about l0 μm or so. Thin films have got unique properties significantly different from their corresponding bulk materials due to small thickness and unique physical structures which are direct consequences of the growth processes. Thin films have extensive applications in various fields of electronics, optics, and defense. There are many successful techniques with which thin films can be deposited usually from bulk targets. Various techniques are; sputtering, chemical bath deposition, thermal deposition in vacuum by resistive heating, electron beam evaporation etc.

In the present work, thermal deposition in vacuum by resistive heating method is used. Thermal deposition is the most widely used method for the preparation of thin films. This method is comparatively simple and is adopted for the deposition of metals, alloys and also many compounds. The process of film deposition by evaporation consists of several physical stages which are; transfer of atoms/molecules from the evaporation source to the substrate, deposition of these particles on the substrate. The quality of the thin film depends on the rate of deposition, substrate temperature, ambient pressure etc. The primary requirement for this method is a high vacuum deposition system having a pressure of about 10^{-4} Pa or even less.

Prior to deposition of thin films, it is essential to clean the surface of the substrate because thin films readily adhere to a clean insulating surface. Tendency for the films to crack and peel increases if the surface is contaminated with foreign impurities and the adhesion of the films is degraded. Cleaning of the substrate is done in three steps: (i) soap solution cleaning and (ii) cleaning with acetone (vapour cleaning) and (iii) with methanol. Soap solution cleaning basically involves scrubbing the substrate in the soap solution, then rinsing it thoroughly with double distilled water. This procedure is repeated 3−4 times for cleaning single substrate. Soap solution cleaning is used to remove any visible oil, grease and dust impurities. Acetone has been used to remove organic impurities and methanol is for the removal of inorganic impurity. After all the cleaning steps, the cleaned substrates are subjected to dry in an oven at a temperature approximately 110 ^{o}C and then put into deposition chamber. In the method of resistive heating, fine powder of the material to be evaporated is put into cleaned boat made of refractory metals like tungsten, molybdenum, and tantalum. The choice of a particular refractory metal as a heating source depends on the materials to be evaporated. The vacuum chamber has been evacuated to a base pressure of 10^{-4} Pa. Flash cleaning is done by passing a heavy current through the boat so as to make it white hot or incandescent for a short period. A shutter incorporated in between the source and the substrate so that no vapour stream of the material can reach the substrate directly prior to attaining the required deposition conditions. After establishing the required source temperature and vacuum in the chamber, the shutter has been removed to start the deposition of film on the cleaned substrate. Thin films have been kept in the deposition chamber in the dark for 24 h to attain thermodynamic equilibrium as emphasized by Abkowitz *et al.* [150]. The evaporation process has been carried out in a vacuum coating system (HINDHIVAC model 12A4D India).

Vacuum deposition of thin films was first carried out by Nahrvvold in 1887. Evaporated thin films find industrial usages for an increasing number of purposes such as front surface mirrors, interference filters, sun glasses and in solar cells.

3.3 Characterization of bulk samples and thin films

For the bulk sample characterization x–ray diffraction (XRD), energy dispersive x–ray spectroscopy (EDAX), Fourier–Transform infrared spectroscopy (FT–IR) and differential thermal analysis (DTA) has been used. The deposited thin films have been characterized for XRD and UV–Vis–NIR spectroscopy. The basic phenomena for the various characterization techniques used are described below.

3.3.1 X–ray diffraction

X–ray diffraction is the most widely used technique to characterize the nature of sample both in bulk and thin film form. In this technique, the beam of x–rays directed at the sample interacts with the electron of atoms. Electrons start oscillating with the same frequency as the incoming beam. The atoms in a crystal are arranged in a regular pattern, and in very few directions constructive interference takes place. Hence, diffracted beam may be described as a beam composed of a large number of scattered rays that reinforce each other. Schematic diagram of x–ray diffractometer has been shown in Figure 3.1. In the scanning mode of θ–2θ, when monochromatic x-rays incident on the sample then it makes an angle θ with the sample *i.e.* θ is the angle between the incident x–rays and the set of parallel atomic planes and not the angle between x–rays and sample surface. The detector motion is coupled with source in such a way so that it always makes an angle of 2θ with the incident direction of beam. Recorded spectrum is between intensity and 2θ.

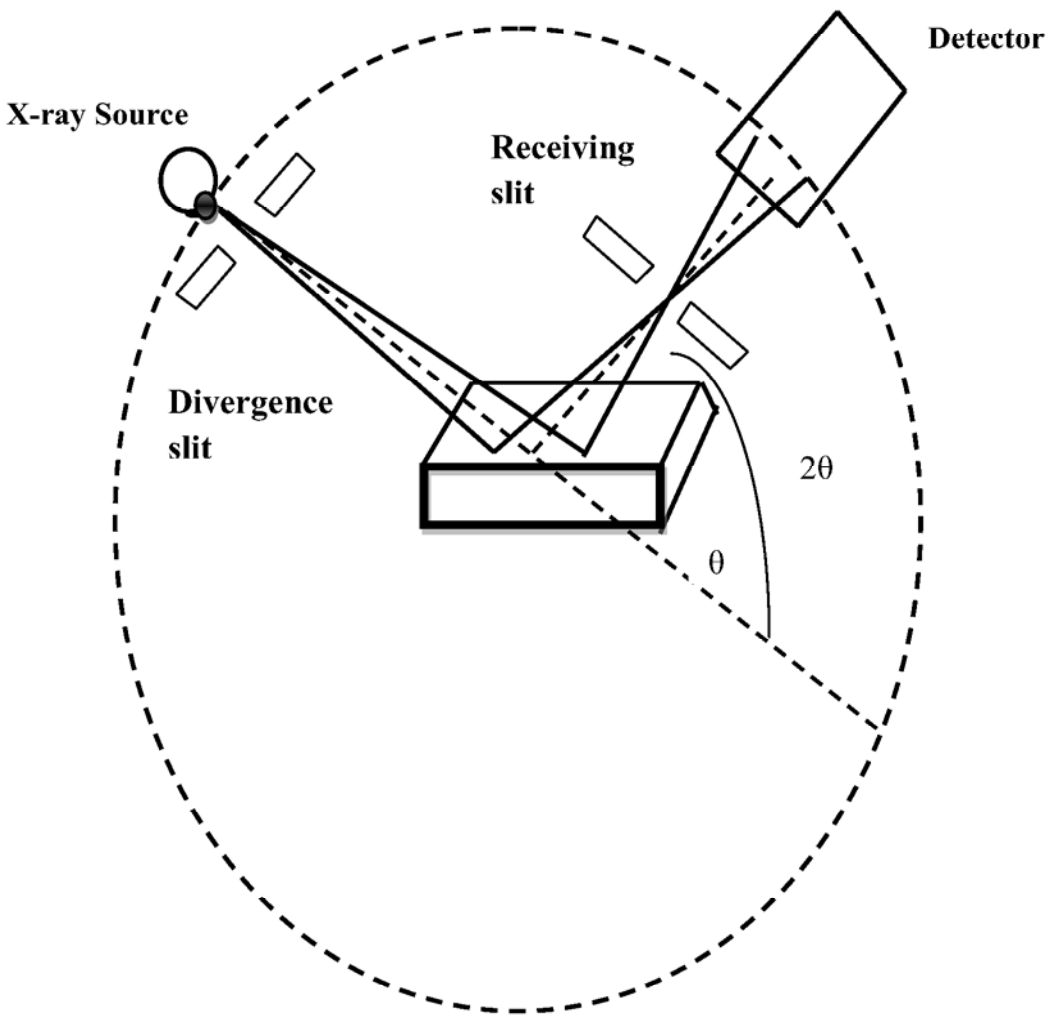

Figure 3.1 Schematic diagram of x–ray diffractometer.

For periodic arrangement of atoms, the x–rays will be scattered only in certain directions when they hit planes. This will cause high intensity peaks and if these peaks are sharpened then material has better crystallinity. X–rays will be scattered in many directions leading to large humps distributed in a wide range instead of high intensity narrower peaks. The powder method has been used to check the nature *i.e.* amorphous or polycrystalline or crystalline of the bulk samples. The bulk samples first crushed to fine powder using mortal & pestle and then used to take XRD pattern. Philips PW 1710 x–ray diffractometer has been used to obtain the XRD patterns of the samples. Data has been obtained in the range 10^{o} to 100^{o} with a step size 0.05^{o}. Thin films deposited on the microscopic glass slides have also been characterized in grazing angle XRD mode to check the crystalline or amorphous nature.

3.3.2 Energy dispersive x–ray spectroscopy

Energy dispersive x–ray spectroscopy is a technique used to characterize the composition of samples. When electron beam interacts with the sample then an electron of the inner shell gets excited and creates a hole in shell. This hole is then filled by an electron of higher energy shell. The difference in the higher energy shell and lower energy shell is released in the form of x–rays (Figure 3.2). The energy emitted by the sample can be measured with energy dispersive spectrometer.

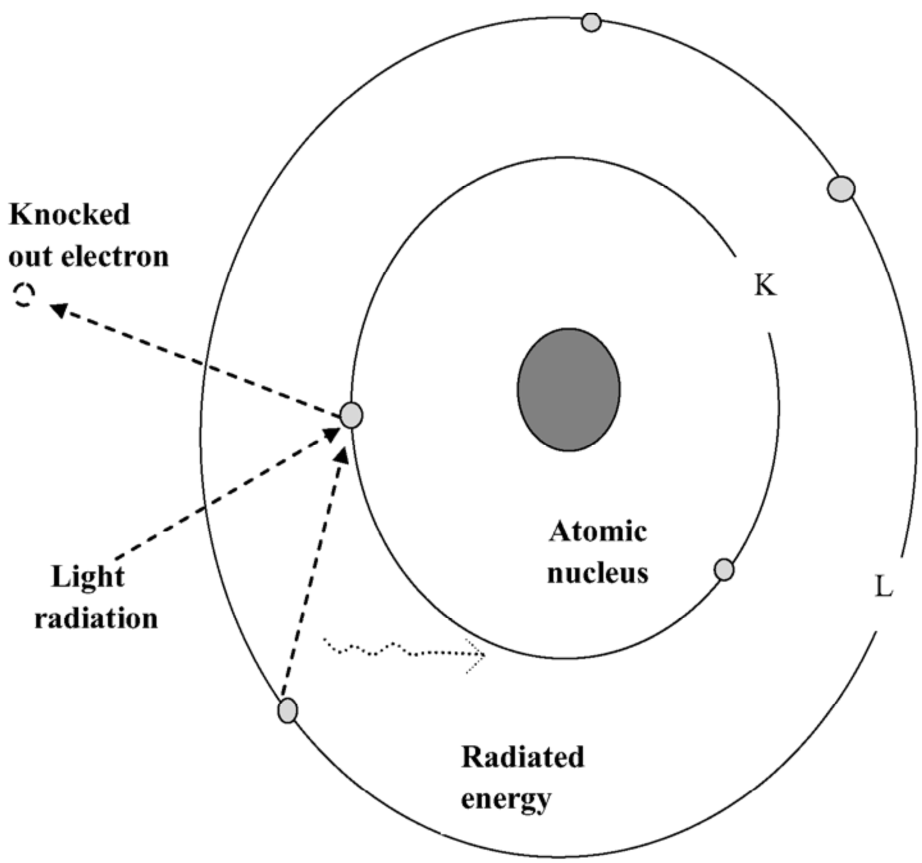

Figure 3.2 Principle of energy dispersive x–ray spectroscopy.

3.3.3 Fourier−Transform infrared spectroscopy

Infrared region of electromagnetic spectrum lies between visible and microwave. Infrared absorption spectroscopy is used to determine the structure of molecules with characteristic absorption of infrared radiation. When sample is exposed to infrared radiation then molecules selectively absorb radiations of specific wavelengths due to which dipole moment of sample molecules change. As a result the vibrational energy levels of sample molecules transfer from ground state to excited state. The intensity of absorption peaks is related to the change of dipole moment and the possibility of the transition of energy levels. Therefore, by analyzing the infrared spectrum, structural information of a molecule can be obtained readily.

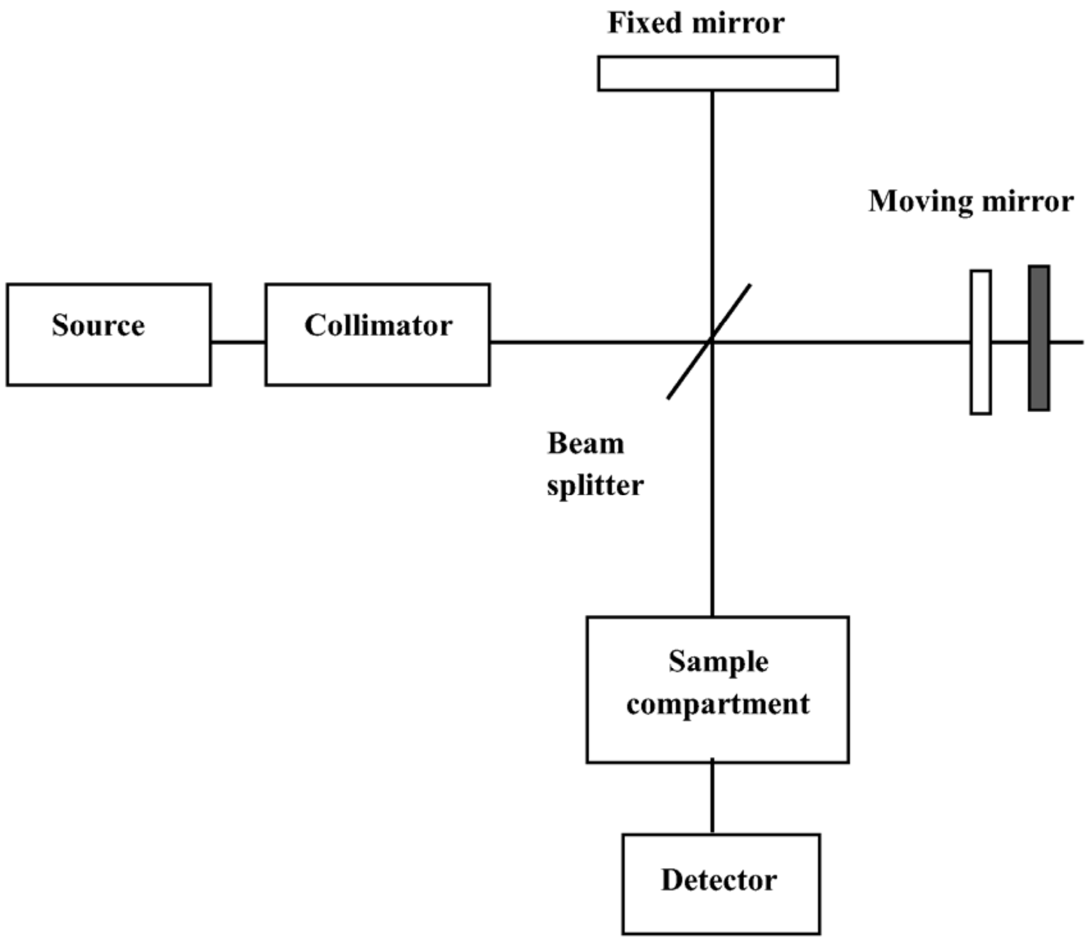

Figure 3.3 Block diagram of Fourier–Transform infrared spectrometer.

Fourier–Transform infrared (FT–IR) spectroscopy combines the advantage of IR spectroscopy (time–based signal) and Fourier–Transform (frequency–based signal).

Block diagram of FT–IR spectroscopy has been illustrated in Figure 3.3. A Michelson interferometer is used for this purpose. Radiation from the source is passed through a beam splitter, so that half of the beam reaches the movable mirror while the other half is reflected from the fixed mirror. The reflected beams from the two mirrors recombine at the beam splitter thus creating constructive and destructive interferences. The resulting interference pattern is a time–based function that is translated as a function of frequency after Fourier−Transform. The obtained spectrum is a pattern of the absorbed frequencies. In the present work, Far–infrared transmission measurements have been obtained in the spectral range of 50–350 cm^{-1} at room temperature using Perkin Elmer–Spectrum RX–IFTIR.

3.3.4 Differential thermal analysis

Differential thermal analysis (DTA) has been used to demonstrate the thermodynamic properties that are essential for understanding the behaviour of material under different heating and cooling rates. DTA is carried out by heating the sample together with reference standard under identical thermal conditions in the same oven then measuring the temperature difference between the sample and reference during the period of heating**.** By this way any change in the state can be seen and temperature at which it occurs will be recorded. In this technique, sample and the reference are placed on the highly thermal conductive pans in furnace as shown in Figure 3.4. Under the sample pans, thermocouples are attached physically. As the detection thermocouples are opposed to each other, small temperature difference between the sample and reference can be detected.

Differential thermal analysis is used to scan a temperature range by heating at a linear rate for the study of exothermic and endothermic change. For an exothermic reaction; the temperature of sample is greater than the reference. For endothermic; the sample temperature lags behind to the reference. When no reaction occurs in the sample material, the temperature of the sample remains same to that of the reference substance. This is due to the reason that both are being heated exactly under identical condition *i.e.* temperature difference will be zero for no reaction. But as soon as reaction starts, the sample becomes either hot or cool depending upon whether the reaction is exothermic or endothermic. In this method, small temperature changes can be easily detected where as the peak area is proportional to the enthalpy change. A reference DTA curve for glassy sample has been given in Figure 3.5.

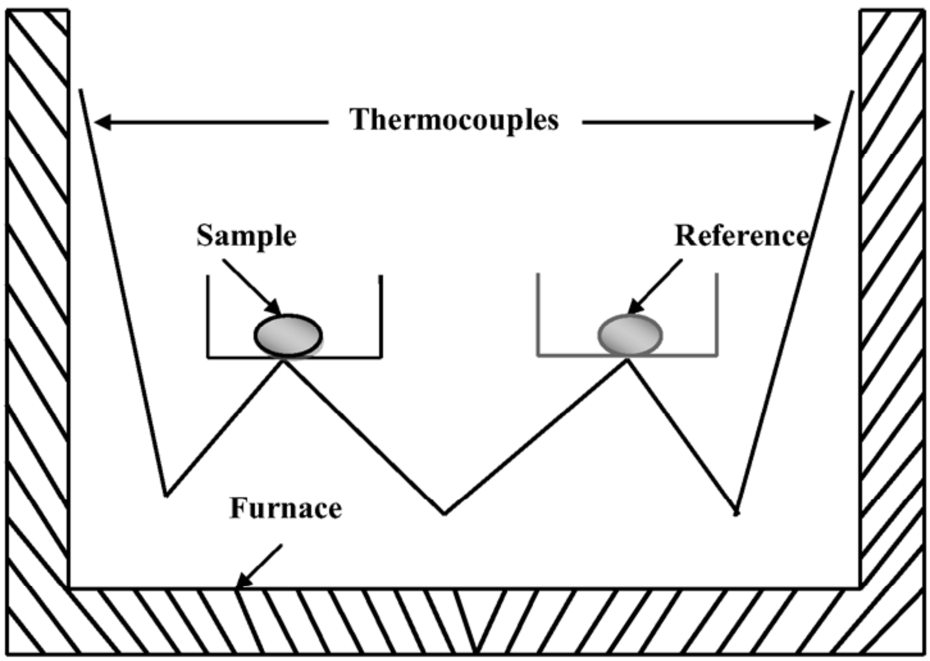

Figure 3.4 Differential thermal analysis apparatus.

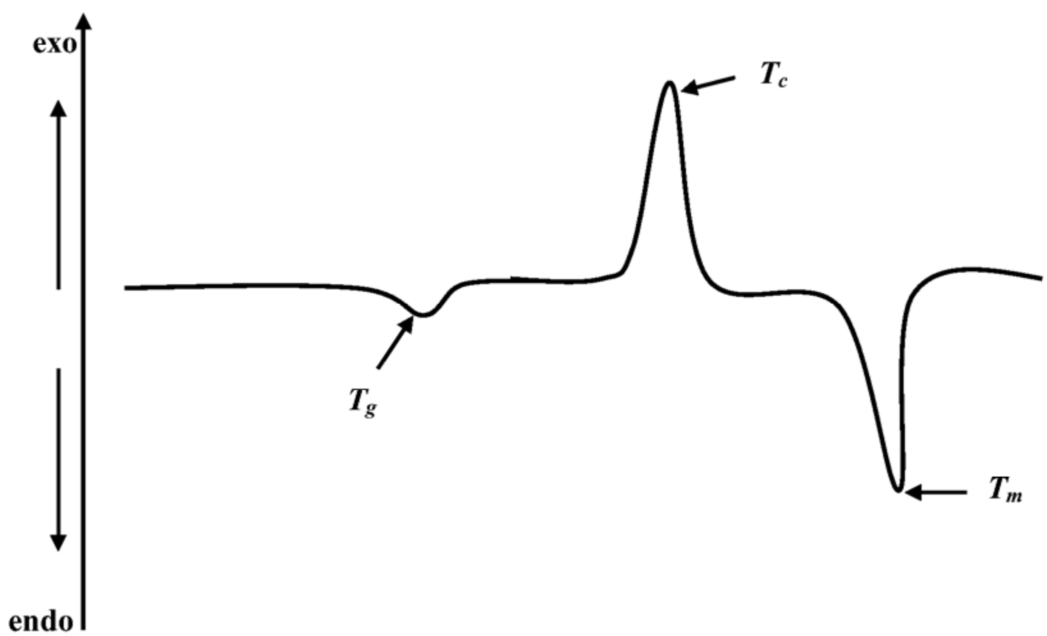

Figure 3.5 A typical DTA curve showing the various temperature peaks.

The glass transition temperature shows endothermic peak and is designated as T_g. The second peak is exothermic which occurs due to phase change and at this point amorphous mass begins to crystallize and is assigned as crystallization temperature (T_c). The third peak is endothermic peak which takes place due to absorption of heat and sample begins to melt and is represented as melting temperature (T_m). General behaviour of the glass is to show one or more exothermic peak while some glasses do not show even one exothermic peak such glasses have high thermal stability. Glass which is very unstable shows multiple peaks of crystallization. The instrument used for thermal analysis in the present work is EXSTAR TG/DTA 6300 with alumina pan.

3.3.5 Transmission spectroscopy

A number of things happen when a light beam comes in contact with a solid such as reflection, transmission, etc. No material is fully transparent in all optical frequencies and hence, there is always some absorption in some region of the spectra. Using UV−Vis−NIR spectrophotometer, it possible to measure different percentages of light transmitted or absorbed by the sample. Spectrophotometer measures the intensity of light passed through a sample (I), and compares it with the intensity of light before it passes through the sample (I_o). The ratio I/I_o is called the "transmittance", and usually expressed as a percentage (%T). Spectrophotometer can be a single beam or a double beam. In a single beam spectrophotometer, whole light passes through the sample cell. I_o must be measured by removing the sample.

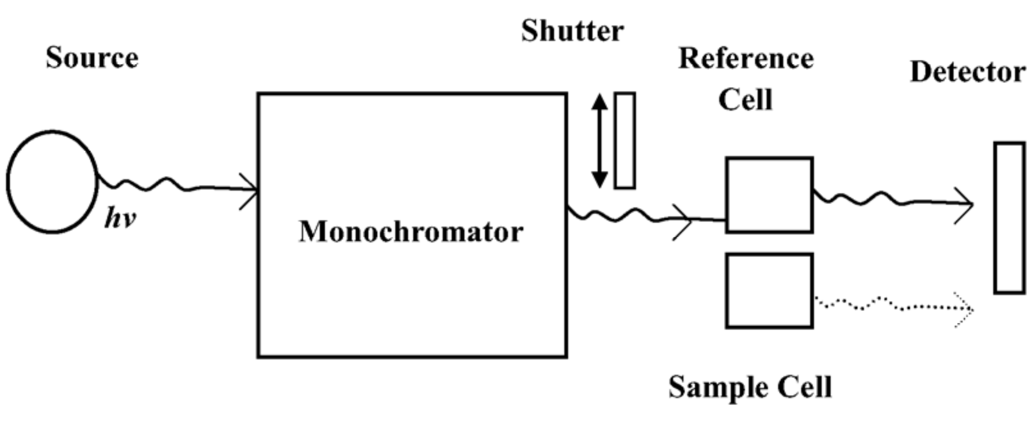

Figure 3.6 Schematic diagram of a double-beam UV−Vis−NIR spectrophotometer.

A double beam spectrophotometer utilizes two beams of light; a reference beam and a sampling beam that passes through the sample. The reference beam intensity is taken as 100 % transmission and the measurement displayed is the ratio of the intensities of two beams. The basic parts of the spectrophotometer are; light source, monochromator, sample holder. The block diagram of spectrophotometer is shown in Figure 3.6. Thin films are studied more accurately by acquiring transmission instead of absorption which is used for bulk glasses. Typical spectral transmission curves *i.e.* interference fringes are obtained. From these spectral transmission curves of thin film, thickness and various optical constants such as refractive index and optical band gap can be extracted.

In the present study, the normal incidence transmittance spectra in the spectral range 400–2400 nm of films have been obtained by a double beam ultraviolet–visible–near infrared spectrophotometer (Perkin Elmer Lambda–750). All measurements have been performed at room temperature (300 K). The spectrophotometer is set with a slit width of 1 nm in the spectral range [151]. Slit width correction is not needed due to its small value in comparison with different line widths.

CHAPTER 4

Physical, structural, thermal and optical properties of ternary chalcogenide glassy semiconductors

- **Neha Sharma**, Sunanda Sharda, Vineet Sharma and Pankaj Sharma, "*Far−Infrared Investigation of Ternary Ge−Se−Sb and Quaternary Ge−Se−Sb−Te Chalcogenide Glasses*" **Journal of Non–Crystalline Solids**, 375 (2013) 114–118.
- **Neha Sharma**, Sunanda Sharda, Vineet Sharma and Pankaj Sharma, "*Effect of Antimony Addition on Thermal Stability and Crystallization Kinetics of Germanium – Selenium Alloys*" **Journal of Non–Crystalline Solids,** 371−372 (2013) 1–5.
- **Neha Sharma**, Sunanda Sharda, Vineet Sharma and Pankaj Sharma, "*Nonlinear optical properties of IV-V-VI chalcogenide glasses*" **AIP Conference Proceedings,** 1512 (2013) 546–547.
- **Neha Sharma**, Sunanda Sharda, Vineet Sharma and Pankaj Sharma, "*Optical analysis of $Ge_{19}Se_{81-x}Sb_x$ thin films using single transmission spectrum*" **Materials Chemistry and Physics**, 136 (2012) 967−972.
- **Neha Sharma**, Sunanda Sharda, Vineet Sharma and Pankaj Sharma, "*Structural Rigidity, Percolation and Transition-Temperature Study of the $Ge_{19}Se_{81-x}Sb_x$ System*" **Defect and Diffusion Forum** 316–317 (2011) 37–44.

In the this chapter, various physical parameters *viz.* average coordination number, glass transition temperature, cohesive energy, theoretical energy gap and structural properties have been determined for $Ge_{19}Se_{81-x}Sb_x$ (x = 0, 4, 8, 12, 16, 17.2, 20) system. Thermal and optical properties have also been described for $Ge_{19}Se_{81-x}Sb_x$ (x = 0, 4, 8, 12, 16, 17.2, 20) system.

4.1 Physical properties of *Ge–Se–Sb* chalcogenide glasses

Chalcogenide glasses are of special interest for their high transparency towards the infrared region. These glasses are attractive candidates for various applications due to their good optical and thermal properties. *Ge–Se–Sb* system is an important system; the addition of *Sb* to *Ge–Se* creates a configurational disorder in the system. For the fabrication of waveguide sensors, absorption coefficient and scattering losses should be small in desired wavelength [109]. Therefore, when small quantity of *Sb* is added to *Ge–Se* system there is a significant decrease in optical loss [109]. It has been expected that physical properties of chalcogenide glasses can be tuned by their chemical compositions. On the basis of constraint theory it has been concluded that physical properties of such covalent glasses can be controlled by the mean coordination number. According to Phillips and Thorpe model; for low average coordination number, the network of the glass is polymeric in which rigid regions are isolated [152,153]. As the average coordination number increases, the rigid regions grow in size and get interconnected. When average coordination number is 2.4 then a stage comes where network transforms into completely rigid glassy structure and this transition is called as rigidity percolation. Another model which depends upon composition is chemical ordering threshold [154]. The threshold position which usually found is based on the stoichiometric composition of the system. At the stoichiometric composition, only heteropolar bonds present. Various properties at this point show more significant changes. In this section, some physical parameters have been calculated for $Ge_{19}Se_{81-x}Sb_x$ (x = 0, 4, 8, 12, 16, 17.2, 20) system.

4.1.1 Experimental details

Bulk samples of $Ge_{19}Se_{81-x}Sb_x$ (x = 0, 4, 8, 12, 16, 17.2, 20) have been synthesized by melt quench technique. Materials have been weighed according to their atomic weight percentage and sealed in evacuated (~ 10^{-4} Pa) quartz ampoules. The sealed ampoules have been kept inside the furnace where the temperature has been increased up to 1000 ºC at a heating rate of 3–4 ºC/min. The ampoules have been rocked for 24 hours at the highest temperature to make the melt homogeneous. Then these ampoules have been quenched in ice–cold water. The ingots of samples in the form of bulk glass have been taken out by breaking the ampoules.

4.1.2 Results and discussion

4.1.2.1 Average coordination number and number of constraints

Chalcogenide glasses with varying compositions have a correspondingly changing covalent coordination number, so it is useful to introduce the concept of average coordination number. Average coordination number (*m*) is the mean number of bonded neighbors per atom in the structure [155];

$$m = uN_{Ge} + vN_{Se} + wN_{Sb} \tag{4.1}$$

where *u, v, w* are atomic fraction and N_{Ge} = 4, N_{Se} = 2, N_{Sb} = 3 are coordination number of *Ge*, *Se* and *Sb* respectively. The covalent bonded glassy networks are influenced by mechanical constraints (N_c) these are; bond stretching (N_a) and bond bending (N_b) [157] and has been calculated as;

$$N_a = \frac{m}{2} \tag{4.2}$$

$$N_b = 2m - 3 \tag{4.3}$$

The total number of constraints per atom is given by;

$$N_c = N_a + N_b \tag{4.4}$$

Average coordination number represents the degree of crosslinking in the structure. The values of *m* are listed in Table 4.1 indicating that with the increasing *Sb* content, *m* increases. According to Phillips – Thorpe [153], for $x = 0$ and $m = 2.38$, composition lies in floppy mode. Floppy mode system consists of long polymeric chains, with few crosslinks in rigid region and hence, deformed easily [156]. For $x \geq 4$, the value of *m* exceeds 2.4 where there is a transition from floppy mode to rigid mode. As the *Sb* content is increased, there is a crosslinking of Se_n chains with possible formation of Sb_2Se_3 units. This increases the rigidity of the structure. Further, this increase in rigidity for compositions $x \geq 4$ has been explained on the basis of average number of constraints. Average number of constraints (N_c) for $x \geq 4$ is greater than number of degrees of freedom (N_d) confirms the rigidity percolation [155]. In $Ge_{19}Se_{81-x}Sb_x$ the possible structural units are; $Ge(Se_{1/2})_4$ tetrahedral and Sb_2Se_3 trigonal. This shows that that there is structural transition from 2–D network to 3–D network.

Table 4.1 Values of average coordination number (m), number of bond bending (N_a), number of bond stretching (N_b), total number of constraints per atom (N_c) and mean bond energy ($\langle E \rangle$) for $Ge_{19}Se_{81-x}Sb_x$ (x = 0, 4, 8, 12, 16, 17.2, 20) system.

Samples	***m***	N_a	N_b	N_c	**$\langle E \rangle$ (eV)**
x = 0	2.38	1.19	1.76	2.95	2.3189
x = 4	2.42	1.21	1.84	3.05	2.3786
x = 8	2.46	1.23	1.92	3.15	2.4438
x = 12	2.50	1.25	2.00	3.25	2.5143
x = 16	2.54	1.27	2.08	3.35	2.5897
x = 17.2	2.55	1.28	2.10	3.38	2.6133
x = 20	2.58	1.29	2.16	3.45	2.1972

4.1.2.2 Lone–pair electrons, deviation to stoichiometry, mean coordination number and glass transition temperature

Lone–pair electrons (L) play an important role in chalcogenide glass formation. The lone–pair electrons have a character of flexibility. To calculate the number of lone–pair electrons of chalcogenide glass system, the average coordination number is used as;

$$L = V_a - m \tag{4.5}$$

where L and V_a are lone–pair electrons and valence electrons, respectively. The number of lone–pair electrons decrease with increasing content of Sb (Figure 4.1).

This is due to the reason that with increasing concentration of *Sb*, the interaction between *Sb* and *Se* atoms increase and hence number of lone–pair electrons decrease [158]. In $Ge_{19}Se_{81-x}Sb_x$, number of lone–pair electrons is greater than 1, which is the necessary condition for stability of ternary chalcogenide glasses, indicates that the system under investigation is a good glass former [159].

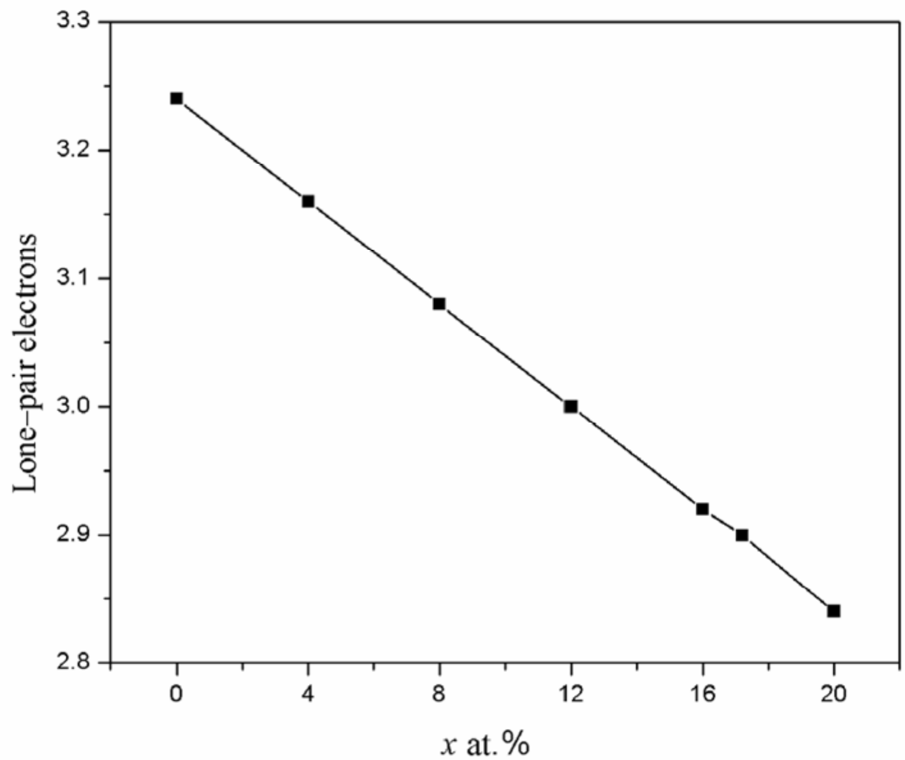

Figure 4.1 Variation of lone–pair electrons with x at.% for $Ge_{19}Se_{81-x}Sb_x$ (x = 0, 4, 8, 12, 16, 17.2, 20) system.

Deviation to stoichiometry (R) is expressed by the ratio of covalent bonding possibilities of chalcogen atom to non–chalcogen atom. For $Ge_uSe_vSb_w$ system, R is defined as [160, 161];

$$R = \frac{vN_{Se}}{uN_{Ge} + wN_{Sb}} \tag{4.6}$$

The mean bond energy <*E*> depends upon the factors like average coordination number, degree of crosslinking, type of bond and bond energy forming a network. The mean bond energy has been calculated by the relation [161];

$$\langle E \rangle = E_C + E_{rm} \tag{4.7}$$

where E_c is the overall contribution towards the mean bond energy arising from heteropolar bonds.

For system $Ge_uSe_vSb_w$, E_C is given as:

$$E_C = uN_{Ge}E_{Ge-Se} + wN_{Sb}E_{Sb-Se} \qquad R > 1$$

$$E_C = \frac{2v[uN_{Ge}E_{Ge-Se} + wN_{Sb}E_{Sb-Se}]}{N_{Ge} + N_{sb}} \qquad R < 1$$

The bond energy values of heteropolar bonds have been calculated using Pauling relation [162].

$$E(A-B) = [E(A-A) \times E(B-B)]^{0.5} + 30(\chi_A - \chi_B)^2 \tag{4.8}$$

where χ_A and χ_B are electronegativities of the atoms, *A* and *B* & *E*(*A*–*A*) and *E*(*B*–*B*) are the bond energies of *A*–*A* and *B*–*B* bonds, respectively.

The calculated values of *Ge*–*Se* and *Sb*–*Se* bonds are 49.42 kcal/mol and 43.96 kcal/mol respectively. E_{rm} is the contribution arising from weaker bonds and in our system it is given as:

$$E_{rm} = \frac{[vN_{Se} - uN_{Ge} - wN_{Sb}]E_{Se-Se}}{m} \qquad R > 1$$

$$E_{rm} = \frac{[uN_{Ge} - wN_{Sb} - vN_{Se}]E_{\langle\rangle}}{m} \qquad R < 1$$

$$E_{\langle\rangle} = \frac{[E_{Ge-Ge} - N_{Sb-Sb} - E_{Ge-Sb}]}{3}$$

E_{Ge-Ge} = 37 kcal/mol, E_{Se-Se} = 44 kcal/mol, E_{Sb-Sb} = 30.22 kcal/mol

The glass transition temperature (T_g) is an important parameter for the characterization of glassy state. There is an impressive relation between <*E*> and T_g given by Tichy and Ticha [160, 161];

$$T_g = 311[< E > -0.9] \tag{4.9}$$

The values of mean bond energy <*E*> are listed in Table 4.1. The values of <*E*> increase with the increasing content of *Sb* upto x =17.2 at.% and then decreases. The divalent *Se* atom and trivalent *Sb* atom is saturated at x = 17.2 and in the composition $Ge_{19}Se_{38}Sb_{17.2}Se_{25.8}$, Se_n chain is completely crosslinked and structural units of tetrahedral $Ge(Se_{1/2})_4$ and trigonal Sb_2Se_3 units have been formed.

For R = 1, system contains only heteropolar bonds and glass transition temperature is maximum for x = 17.2.

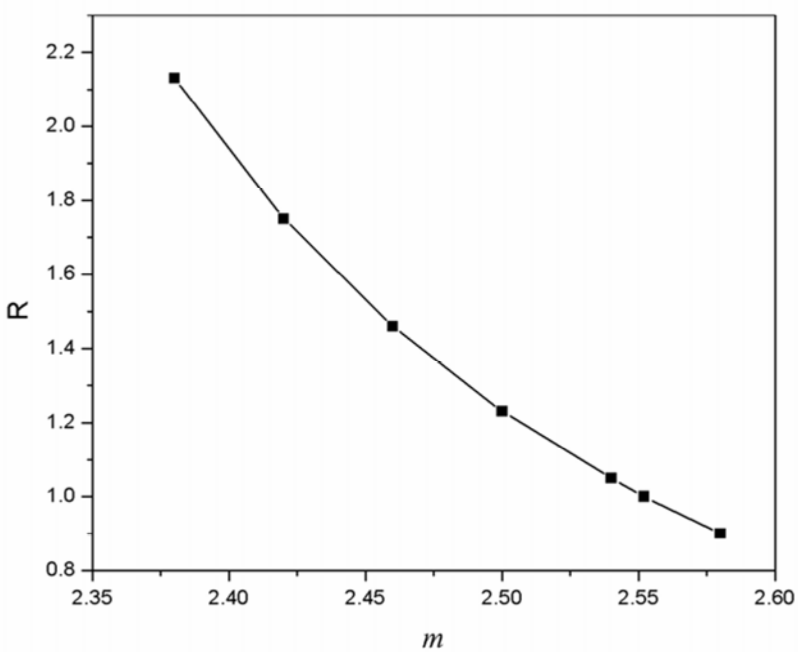

Figure 4.2 Variation of R with *m* for $Ge_{19}Se_{81-x}Sb_x$ (x = 0, 4, 8, 12, 16, 17.2, 20) system.

For R > 1, the heteropolar bonds *i.e.* *Ge–Se* and *Sb–Se* bonds are formed but *Se–Se* homopolar bonds have a share of ~ 25 % to 53 %.

For R < 1, metallic *Sb–Sb* bonds (~ 12 % for x = 20) has been formed along with the heteropolar bonds. Since, heteropolar bonds are more stable than homopolar bonds so the system with R = 1 is most stable in comparison to R > 1 and R < 1. The values of R have been found to decrease with increasing *m* while T_g shows maximum at $m = 2.55$ (Figure 4.2 and Figure 4.3). This can be correlated with the stability of the composition *i.e.* with R = 1

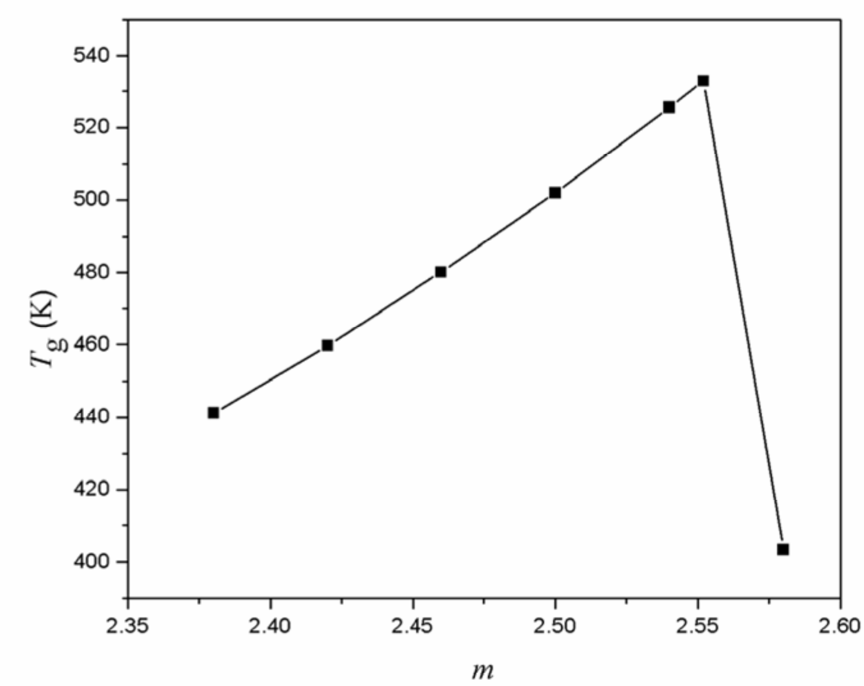

Figure 4.3 Variation of T_g with m for $Ge_{19}Se_{81-x}Sb_x$ (x = 0, 4, 8, 12, 16, 17.2, 20) system.

4.1.2.3 Distribution of chemical bonds, cohesive energy, electronegativity, theoretical energy gap and heat of atomization

According to chemical bond approach [163], atoms combine more favorably with the atoms of different kind rather than the same kind. The bonds are formed in the sequence of decreasing bond energy until the available valence of atoms is saturated. The bond energy of *Ge–Se* bonds is high and formed first followed by *Sb–Se* bonds having slightly low energy. When the *Se* is completely satisfied by *Ge* and *Sb* then remaining bonds *i.e.* *Sb–Sb* bonds have been formed.

The distribution of possible chemical bonds has been given in Table 4.2. Cohesive energy (*CE*) measures the average bond strength of the system. Cohesive energy has been calculated by the summing the bond energies of the bonds present in the system; $CE = \sum C_i E_i$, where C_i is number of expected chemical bonds and E_i is the energy of corresponding bonds [164]. In $Ge_{19}Se_{81-x}Sb_x$ alloy, *CE* has been found to increase (Table 4.2) with increasing content of *Sb* upto 17.2 at.% due to the formation of heteropolar bonds. After $x > 17.2$ at.% of *Sb*, formation of *Sb–Sb* bonds lower down the cohesive energy. The electronegativity has been calculated using Sanderson's principle [164]. According to this principle, electronegativity of the alloy is the geometric mean of electronegativity of its constituents; $\chi = (\chi_{Ge})^{(u_{Ge})} * (\chi_{Se})^{(v_{Se})} * (\chi_{Sb})^{(w_{Sb})}$. The electronegativity of the system is decreasing with increasing content of *Sb* (Table 4.2).

Table 4.2 Distribution of chemical bonds, cohesive energy (*CE*) and electronegativity (χ) for $Ge_{19}Se_{81-x}Sb_x$ (x = 0, 4, 8, 12, 16, 17.2, 20) system.

Samples	**Distribution of chemical bonds**				***CE*** **(kcal/mol)**	χ
	Ge-Se	***Sb-Se***	***Se-Se***	***Sb-Sb***		
$x = 0$	0.46914	-	0.53086	-	46.54	2.437
$x = 4$	0.49351	0.07792	0.42857	-	46.67	2.416
$x = 8$	0.52055	0.16438	0.31507	-	46.81	2.395
$x = 12$	0.55072	0.26087	0.10841	-	46.98	2.374
$x = 16$	0.58462	0.36923	0.04615	-	47.16	2.354
$x = 17.2$	0.59561	0.40439	-	-	47.22	2.347
$x = 20$	0.62210	0.25140	-	0.1265	45.62	2.333

The theoretical energy gap (E_g^{th}) is the energy difference between the top of valence band and bottom of the conduction band. Theoretical energy gap has been calculated using Shimakawa's relation [123],

$$E_g^{th}(Ge - Se - Sb) = \xi E_g(Ge) + \psi E_g(Se) + \kappa E_g(Sb) \tag{4.10}$$

where ξ, ψ, κ are the volume fractions and $E_g\,(Ge)$, $E_g\,(Se)$, $E_g\,(Sb)$ are the energy gaps of *Ge*, *Se* and *Sb* respectively. There is a correlation between the electronegativity and energy gap given by Kastner [165]. In chalcogenide glasses valence band is formed by the unshared or lone–pair electron of p–orbital. *Se* is an electronegative element with χ = 2.55 and have a lone–pair electron in its p–orbital and the energy of this lone–pair electron is high. *Sb* whose electronegativity (χ = 2.05) is less than *Se* element acts like an electropositive element. On the addition of such electropositive element, the energy of lone–pair state further increases. This leads to the broadening of valance band inside the forbidden gap. Hence, the energy gap and electronegativity decreases with the addition of *Sb* content.

Heat of atomization (H_s) is defined as the change in enthalpy when one mole of compound converts into gas atoms (*i.e.* free atoms). The average heat of atomization for a compound $Ge_uSe_vSb_w$ is a direct measure of the cohesive energy [166];

$$H_s = uH_s^{Ge} + vH_s^{Se} + wH_s^{Sb} \tag{4.11}$$

The values of heat of atomization of *Ge*, *Se*, and *Sb* are 90, 42.4, 62 kcal/g–atom respectively. The values of average heat of atomization increase with the addition of *Sb* content, this shows that the system move towards the more rigid side and hence rigidity of the system increases. The values of H_s are listed in Table 4.3.

Table 4.3 Values of average heats of atomization (H_s), density (ρ) and molar volume (V_m) for $Ge_{19}Se_{81-x}Sb_x$ (x = 0, 4, 8, 12, 16, 17.2, 20) system.

Samples	**H_s (Kcal/g–atom)**	**ρ (g/cm^3)**	**V_m (cm^3/mol)**
***x* = 0**	57.11	4.89	15.90
***x* = 4**	57.61	4.97	15.99
***x* = 8**	58.12	5.04	16.11
***x* = 12**	58.62	5.12	16.19
***x* = 16**	59.13	5.19	16.30
***x* = 17.2**	59.28	5.22	16.32
***x* = 20**	59.63	5.27	16.38

The variation of E_g^{th} and average single bond energy (H_s/m) with x at.% has been shown in Figure 4.4. It has been found that (H_s/m) decreases with *Sb* content, due to the decrease in average bond strength of the compound and hence energy gap also decreases [167]. The decrease in average bond strength can also be explained on the basis of repulsion of lone–pair electrons of *Se* element.

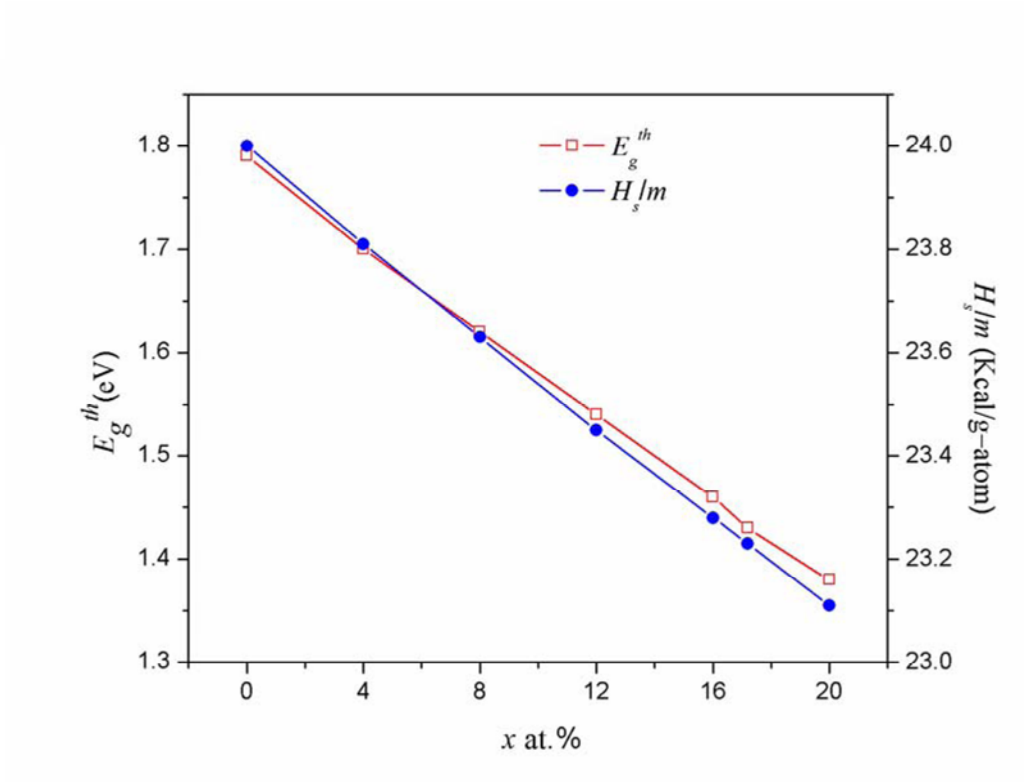

Figure 4.4 Variation of E_g^{th} and H_s/m with *Sb* content (*x* at.%) for $Ge_{19}Se_{81-x}Sb_x$ (x = 0, 4, 8, 12, 16, 17.2, 20) system.

4.1.2.4 Density and molar volume

Density (ρ) is an important physical parameter and it measures the rigidity of the system. ρ has been calculated using the formula [168];

$$\rho = \left(\sum \frac{m_i}{d_i} \right)^{-1} \tag{4.12}$$

where m_i is the fraction of mass and d_i is the density of i^{th} structural unit density.

Molar volume (V_m) has been calculated using value of density expression [168];

$$V_m = \frac{\left(\sum x_i M_i \right)}{\rho} \tag{4.13}$$

where x_i is the atomic fraction of i^{th} component and M_i is its atomic mass.

The values of ρ and V_m are listed in Table 4.3 and have been found to increase with increasing content of *Sb*. The density (4.79 g/cm^3) and mass (78.96 u) of the *Se* element is very low in comparison to heavier *Sb* element having density (6.684 g/cm^3) and mass (121.76 u). So, when *Se* is replaced with heavier and denser *Sb*, both the parameters *i.e.* ρ and V_m increase. Further, the addition of *Sb* content increases the crosslinking in the network and hence rigidity increases due to which density increases.

4.2 Structural studies of *Ge–Se–Sb* chalcogenide glasses

An understanding of structure of amorphous material is important in order to understand the various properties but is difficult to understand. There are two main reasons for this;

(i) The study of structure for crystals can be done using x–ray diffraction but in case of glasses there is no direct probe to understand the structure. This is due to the absence of long range order in glasses.

(ii) It has been emphasized that the glasses have metastable states with respect to crystalline material that forms the thermodynamic equilibrium state of lowest energy.

However, infrared absorption can provide the information about the structure of chalcogenide glasses. Several authors have studied the IR and Raman spectra in order to attain information about the structural arrangements in glasses [169–171]. In this section, $Ge_{19}Se_{81-x}Sb_x$ (x = 0, 4, 8, 12, 16, 17.2, 20) system has been studied for its structural nature and bonding arrangement using x–ray diffraction (XRD) and Far–IR spectroscopy respectively.

4.2.1 Experimental details

The detailed synthesis of bulk samples has been given in section 4.1.1. XRD has been used to characterize the nature of synthesized samples (X' Pert Pro). Bulk samples have been characterized using energy dispersive x–ray spectroscopy (EDAX) (Zeiss EVO 40 EP with EDAX attachment operated at 20 kV) for the analysis of compositions. The Far–IR absorption measurements have been obtained in spectral range 30–350 cm^{-1} at room temperature using FT–IR Spectrometer (Perkin Elmer–

Spectrum RX–IFTIR). The resolution during measurements has been set at 1 cm^{-1}. Measurements have been taken using polyethylene pellet (13 mm diameter). The pellets have been prepared by mixing 2 mg sample with 200 mg of spectroscopic grade polyethylene and pressed into pellets using hydraulic press (~ 10 ton). To take account of polyethylene absorption; the spectrum of polyethylene has been used as reference spectrum.

4.2.2 Results and discussion

Analysis of x–ray spectra (Figure 4.5) reveals that the samples are amorphous in nature as no distinguishable peaks have been observed. Energy dispersive x–ray spectroscopy results indicate that the atomic percentages of $Ge_{19}Se_{81-x}Sb_x$ compositions are close to starting elements (Table 4.4).

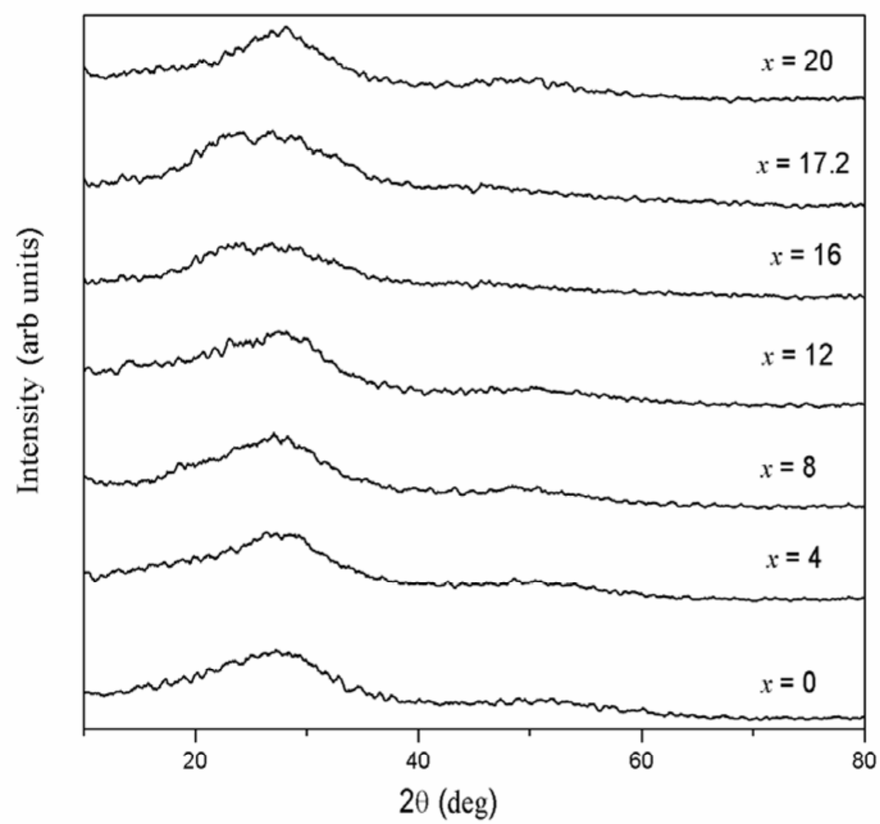

Figure 4.5 XRD spectra of $Ge_{19}Se_{81-x}Sb_x$ glasses.

Table 4.4 Elemental composition of $Ge_{19}Se_{81-x}Sb_x$ (x = 0, 4, 8, 12, 16, 17.2, 20) bulk glasses.

Samples	***Ge***	***Se***	***Sb***
x = 0	19.38	80.62	–
x = 4	19.18	77.43	3.39
x = 8	18.91	73.49	7.60
x = 12	19.14	68.77	12.09
x = 16	19.07	64.83	16.10
x = 17.2	19.29	63.73	16.98
x = 20	19.32	59.97	20.71

4.2.2.1 Far–IR spectral analysis and theoretical wavenumbers

Far–IR spectroscopy gives valuable information about the structural arrangements of glass system. The IR spectra of $Ge_{19}Se_{81-x}Sb_x$ system have been shown in Figure 4.6 for x = 0, 4, 8 and in Figure 4.7 for x = 12, 16, 17.2, 20.

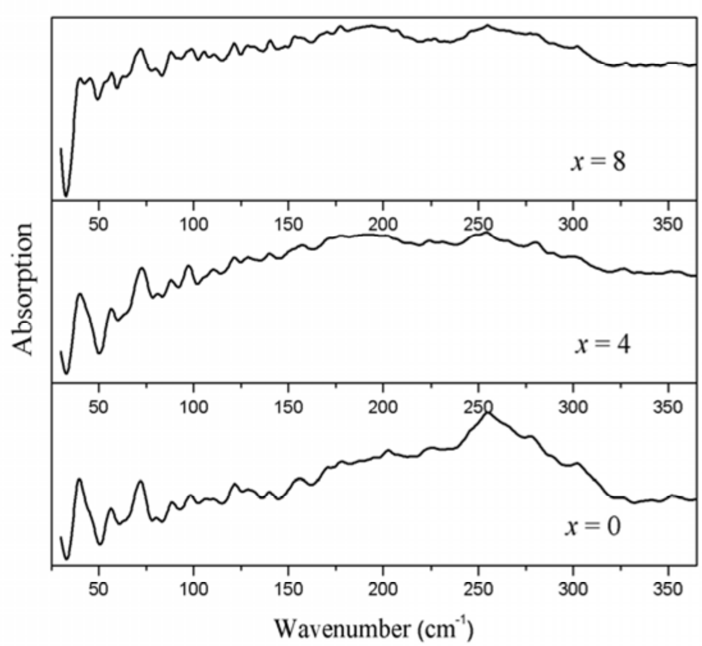

Figure 4.6 Far–IR absorption spectra of $Ge_{19}Se_{81-x}Sb_x$ (x = 0, 4, 8) glassy alloys. The ordinate scale for different x–values is shifted for clarity.

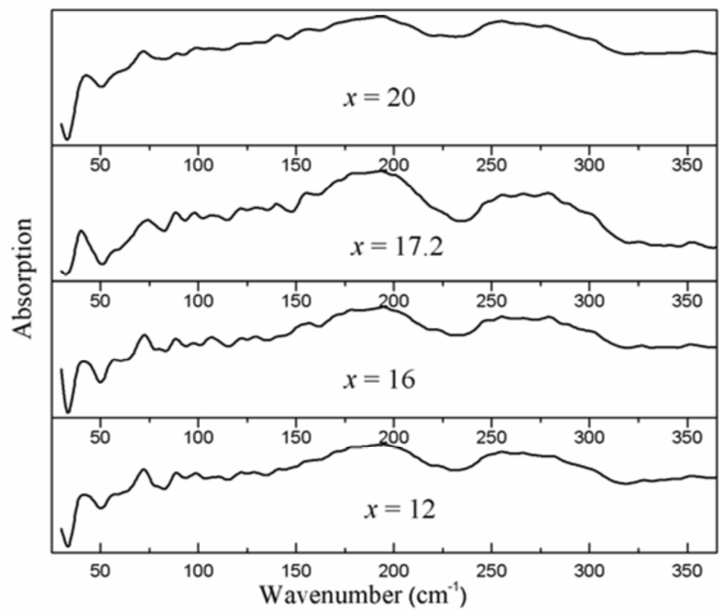

Figure 4.7 Far–IR absorption spectra of $Ge_{19}Se_{81-x}Sb_x$ (x = 12, 16, 17.2, 20) glassy alloys. The ordinate scale for different x–values is shifted for clarity.

Analysis of spectra reveals numerous small–scale features along with major absorption peaks. The possible bond energies of probable bonds in samples under investigation have been calculated using Pauling relation (equation (4.8)) [162]. The relative probability of bonds has also been calculated using probability function $\exp(E/k_BT)$ at room temperature and 1000 °C where the samples have been synthesized.

Far–IR transmission [172] measurement of the material has been discussed under two assumptions:

(1) The valence force field model (VFF); this model assumes that there is strong restoring force in the line of every valence bond if the distance of two atoms bound by this bond is changed [172].

(2) The position of the intrinsic IR features is influenced mainly by stretching force constants of the corresponding chemical bonds [172]. The wave number of the vibration modes in the IR spectra is determined by the mass of atoms and the interatomic force within the groups of atoms comprising the glass network.

The wave number (v) has been calculated by the following formula [172]:

$$v = \frac{1}{2\pi c}\left(\frac{k_r}{\mu}\right)^{1/2} \tag{4.14}$$

where K_r is the bending or stretching force constant of the bond and μ is the reduced mass of the molecule and is given as;

$$\mu = \frac{M_1 M_2}{M_1 + M_2} \tag{4.15}$$

where M_1 and M_2 are the atomic masses of the two atoms.

Force constant (K_{AB}) between the elements A and B has been calculated using Somyajulu method [173]. Using the elemental covalent force constants and electronegativities, K_{AB} has been expressed as [173];

$$K_{AB} = (K_{AA}K_{BB})^{1/2} + (\chi_A - \chi_B)^2 \tag{4.16}$$

where K_{AA}, K_{BB} are the force constants for bonds A–A and B–B respectively and the values are 1.29 eV for *Ge–Ge*, 0.87 eV for *Sb–Sb* and 1.91 eV for *Se–Se* [172]. Calculated values of wavenumbers, reduced mass and force constant of the probable bonds have been listed in Table 4.5.

Table 4.5 Values of bond energy, reduced mass (μ), force constant (K_{AB}), wavenumbers (v), relative probability of bond formation at 27 °C and 1000 °C for various bonds in $Ge_{19}Se_{81-x}Sb_x$ (x = 0, 4, 8, 12, 16, 17.2, 20) glassy alloys.

Bonds	**Bond energy (kcal/mol)**	**μ (10^{-26}Kg U^1)**	**K_{AB} (eV)**	**v (cm^{-1})**	**Relative probability of bond formation at**	
					27 °C	**1000 °C**
Ge–Se	49.42	6.28	1.86	289	1	1
Sb–Se	43.96	6.56	1.91	287	1.13×10^{-4}	1.17×10^{-1}
Se–Se	44.00	7.95	1.54	234	1.05×10^{-4}	1.15×10^{-1}
Ge–Ge	37.00	6.03	1.29	246	2.47×10^{-9}	9.3×10^{-3}
Ge–Sb	33.76	7.55	1.06	199	3.95×10^{-12}	2.05×10^{-3}
Sb–Sb	30.22	10.11	0.87	156	1.04×10^{-14}	5.05×10^{-4}

For *Ge–Se* glasses, Tronc and Lucovsky have proposed models in order to understand the structure of glasses [113, 114]. When *Ge* is introduced into *Se*, $GeSe_4$ tetrahedral molecules are formed having four fundamental modes (ν_1, ν_2, ν_3, ν_4) [174]. Although only bond stretching modes (ν_3) and bond bending modes (ν_4) are infrared active in $GeSe_4$ molecules. For $Ge_{19}Se_{81}$ bulk glass, the sharp absorption peaks have been observed at ~ 40 cm^{-1}, 72 cm^{-1}, 88 cm^{-1}, 99 cm^{-1}, 121 cm^{-1}, 156 cm^{-1}, 254 cm^{-1} along with one shoulder at 278 cm^{-1}. One weak absorption peak around 225 cm^{-1} has been found. The existence of sharp absorption peak at 40 cm^{-1} indicates Se_8 (E_2 mode). The absorption peak at 40 cm^{-1} is in good agreement with earlier reported result [113]. Absorption peak at ~72 cm^{-1} has been designated to $GeSe_4$ (ν_2 mode) [175]. Absorption peak at 88 cm^{-1} has been observed and designated as transverse optical (TO) of $GeSe_2$ crystal mode. Absorption peak situated at 99 cm^{-1} indicates Se_8 (E_2 mode) and Se_8 rings. The existence of peak at 99 cm^{-1} is in accordance with earlier reported results by Ball *et al.* [175], Lucovsky [114] and Ohsaka [174].

Absorption peaks appearing at 121 cm^{-1} and 156 cm^{-1} have been assigned to $GeSe_2$ (Raman mode) [175]. A weak absorption peak corresponding to 223 cm^{-1} has been attributed to be $GeSe_2$ mode along with the vibrations of *Ge–Ge* bonds [176]. Weak absorption peaks in IR spectra may come from the Raman–allowed modes of small crystal–like remnants [177]. This may be due to the relaxation of selection rules. Absorption peak at 254 cm^{-1} has been obtained along with its shoulder around 278 cm^{-1}. This absorption peak may be assigned as Se_8 (A_1, E modes) [175]. Shoulder may indicate F_2–mode of $GeSe_{4/2}$ tetrahedron [175] and $GeSe_2$ (Raman mode) [175].

When *Sb* is incorporated to $Ge_{19}Se_{81}$ alloy, weak absorption peak at 110 cm^{-1}, 140 cm^{-1}, broad band 163–219 cm^{-1}, peak at 254 cm^{-1} along with its shoulder at 278 cm^{-1} have been observed. The existence of weak absorption peak at 110 cm^{-1} indicating $SbSe_3$ pyramidal unit is in accordance with earlier results obtained by Kumar *et al.* [178]. For x = 12, absorption peak at 110 cm^{-1} does not show its appearance but for x = 16 it appears again. For x = 17.2, this peak shifts toward the lower wavenumber 107 cm^{-1} and becomes comparatively prominent. At $Ge_{19}Se_{63.8}Sb_{17.2}$ there is a possibility of $GeSe_4$ (ν_4 mode) and $SbSe_3$ pyramidal unit [175,178]. Further, for x = 20 it shifts to higher wavenumber 109 cm^{-1}. A new absorption peak has been observed with *Sb* addition at 140 cm^{-1} which is attributed to

Se polymeric chain (E mode). For $x = 16$, absorption peak becomes weak and disappears for $x = 17.2$. The disappearance of peak is due to the crosslinkage of *Se* chains with *Ge* and *Sb* elements making the composition stable. This absorption peak again appears for $x = 20$. A new broad band originates in the range 163–219 cm^{-1} with few features. This band contributes to symmetric stretching mode of $GeSe_4$, Raman mode of $GeSe_2$ and *Sb–Se* bonds. These features are in good agreement with previously obtained results [177,179,180]. This band becomes broad for $x = 16$ and 20, but remains at the same position for other compositions. The absorption peak at 254 cm^{-1} and its shoulder at 278 cm^{-1} have become broad and get enhanced in the range 239 cm^{-1} – 272 cm^{-1} along with a peak at 279 cm^{-1} on addition of 4 at. % *Sb*. This absorption peak becomes a part of the band which gets broader for $x \geq 8$ addition of *Sb*. These features are associated with pyramidal $SbSe_3$ [172], F_2–mode of $GeSe_{4/2}$ tetrahedron [176] and $GeSe_2$ (Raman mode) [175]. For $x = 20$, a new fine feature at 266 cm^{-1} has been appeared in the band and assigned as ν_3 mode of $GeSe_4$. This feature is in good agreement with previous reported result [175].

Other absorption peaks at 40 cm^{-1}, 72 cm^{-1} 88 cm^{-1} and 98 cm^{-1} remains at the same position with the substitution of *Sb* for *Se*. Absorption peak at 40 cm^{-1} gets slightly broaden and at 98 cm^{-1} peak becomes very weak for $x = 17.2$. The absorption peak at 88 cm^{-1} becomes weak for $x = 8$ and 12 but appears to be intense for other compositions. Absorption peak at 121 cm^{-1} remains at the same position for $x = 4$ and 8, but for $x \geq 12$ peak becomes weak. The peak at 156 cm^{-1} takes the same position for $x = 4$ and shifts little towards lower wavenumber with *Sb* addition for $x \geq 8$. The theoretical result shows that the absorption peak at 156 cm^{-1} corresponds to *Sb–Sb* homopolar bonds. This may also contribute to $GeSe_2$ (Raman mode) [175]. Peak becomes a shoulder of broad band ranging from 147–233 cm^{-1} for $x = 16$, 17.2 and 20.

Table 4.5 signifies bond energies and relative probability of bond formation that shows *Se* atom will saturate *Ge* atom first and then *Sb*. For $Ge_{19}Se_{81}$ system only *Ge–Se* and *Se–Se* bonds have been formed. With the addition of *Sb,* some of the *Ge–Se* and *Se–Se* bonds disappear and *Sb–Se* bond formation takes place. For $x = 17.2$ only heteropolar bonds *i.e.* *Ge–Se* and *Sb–Se* have been formed. With further addition of *Sb*, homopolar *Sb–Sb* bonds have been formed. Theoretically calculated *Sb–Sb* bond wavenumber coincides with that obtained from Far–IR study at 156 cm^{-1}.

4.3 Thermal properties of *Ge–Se–Sb* chalcogenide glasses

Glass has been used as an industrial material for centuries but in relatively recent years the ''glass science'' has emerged as a field of study. Thus, the knowledge of glassy materials is one of the most active fields of research in the physics of condensed matter today [66]. Although, traditionally the meaning of solid–state physics and crystal physics has same and hence, solidity and crystallinity have been considered as synonymous. Therefore, the solid–state research in recent years has played an important role in the study of solids for which the arrangement of the atoms lacks the long–range order. To analyze the nature of glass, it is important to perform calorimetric measurement. Two basic methods that can be used are: isothermal and non–isothermal. In the isothermal regime [182, 183, 66] the glass samples are quickly heated up and held a temperature above glass transition temperature. However, in the non–isothermal regime [182, 183, 66] the glass samples are heated up at a fixed heating rate. Using these methods, various thermal parameters have been deduced and hence, behavior of glass can be studied. In this section, differential thermal analysis has been used to analyze the $Ge_{19}Se_{81-x}Sb_x$ (x = 0, 4, 8, 12, 16, 17.2, 20) system for various thermal parameters.

4.3.1 Experimental details

The freshly prepared samples (section 4.1.1) have been ground to fine powder and are taken in the alumina pan for the differential thermal analysis (DTA) (EXSTAR TG/DTA 6300). For each DTA scan, 10 mg of powder has been used with different heating rates, 5 K/min, 10 K/min, 15 K/min and 20 K/min. The melting temperature and melting enthalpy of high purity *In*, *Zn* and *Pb* has been used to calibrate the instrument and the measurements have been carried out in nitrogen atmosphere at a flow rate of 200 ml/min.

4.3.2 Results and discussion

4.3.2.1 Glass transition temperature, crystallization temperature and melting temperature

Figure 4.8 to Figure 4.14 show DTA thermograms of $Ge_{19}Se_{81-x}Sb_x$ (x = 0, 4, 8, 12, 16, 17.2, 20) alloys, having well defined endothermic step at glass transition temperature (T_g) and exothermic at crystallization temperature (T_c) at the heating rate of 5, 10, 15, 20 K/min. T_g represents the strength and rigidity of glass structure.

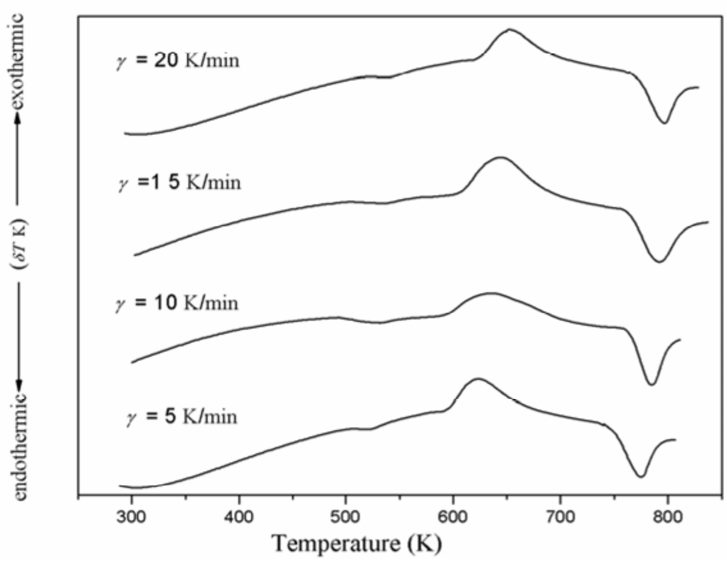

Figure 4.8 DTA thermograms for $Ge_{19}Se_{81}$ alloys at heating rate of 5, 10, 15 and 20 K/min.

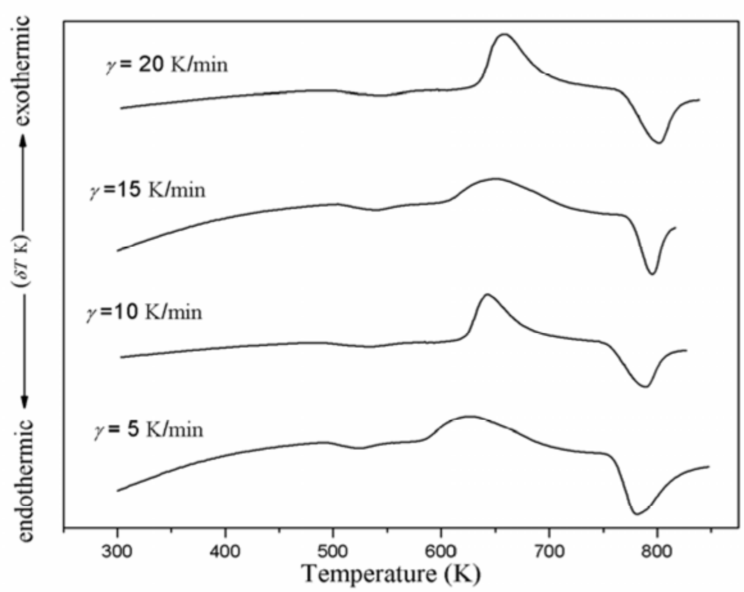

Figure 4.9 DTA curves for $Ge_{19}Se_{77}Sb_4$ alloys at heating rate of 5, 10, 15 and 20 K/min.

An exothermic peak (originated from the amorphous–crystalline phase) gives the value of crystallization temperature. Third peak is endothermic that indicates the melting temperature (T_m).

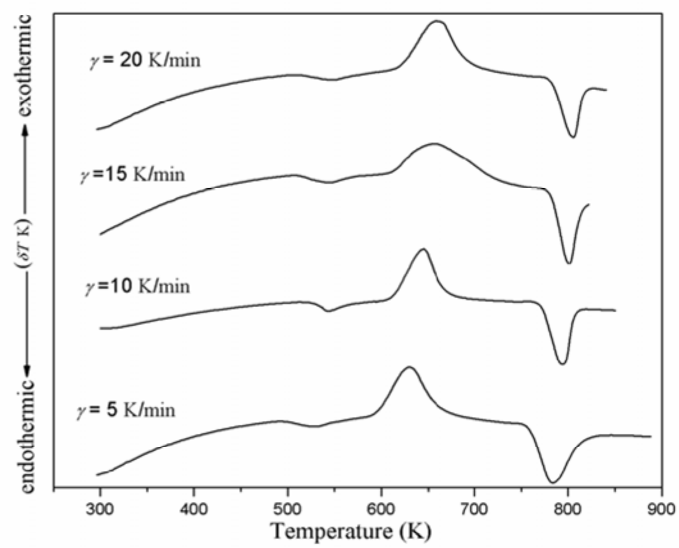

Figure 4.10 DTA trace for $Ge_{19}Se_{73}Sb_8$ alloys at heating rate of 5, 10, 15 and 20 K/min.

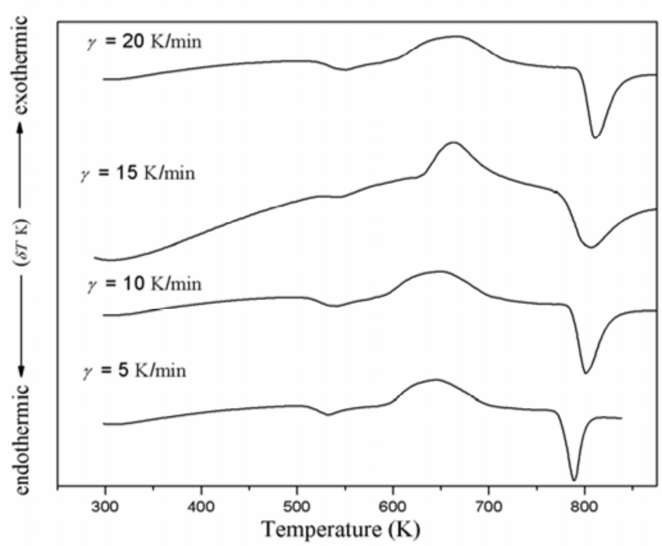

Figure 4.11 DTA thermograms for $Ge_{19}Se_{69}Sb_{12}$ alloys at heating rate of 5, 10, 15 and 20 K/min.

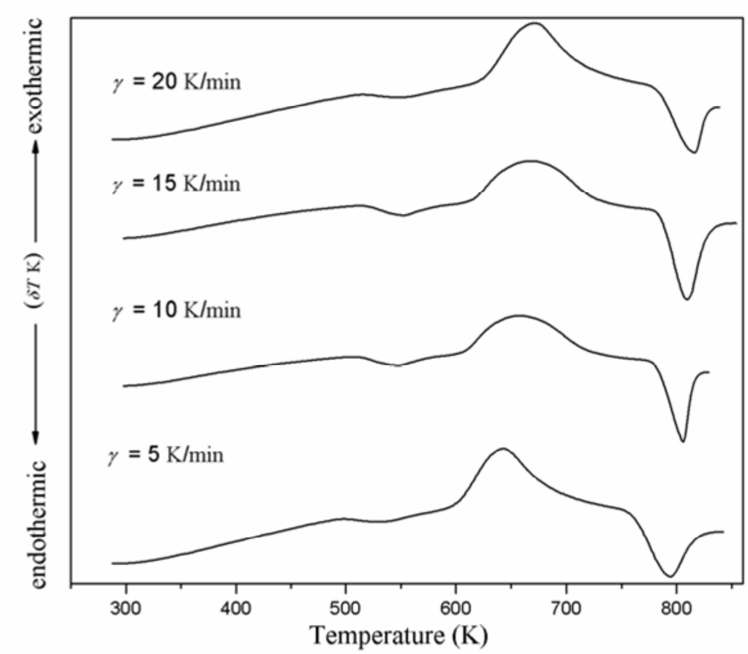

Figure 4.12 DTA curves for $Ge_{19}Se_{65}Sb_{16}$ alloys at heating rate of 5, 10, 15 and 20 K/min.

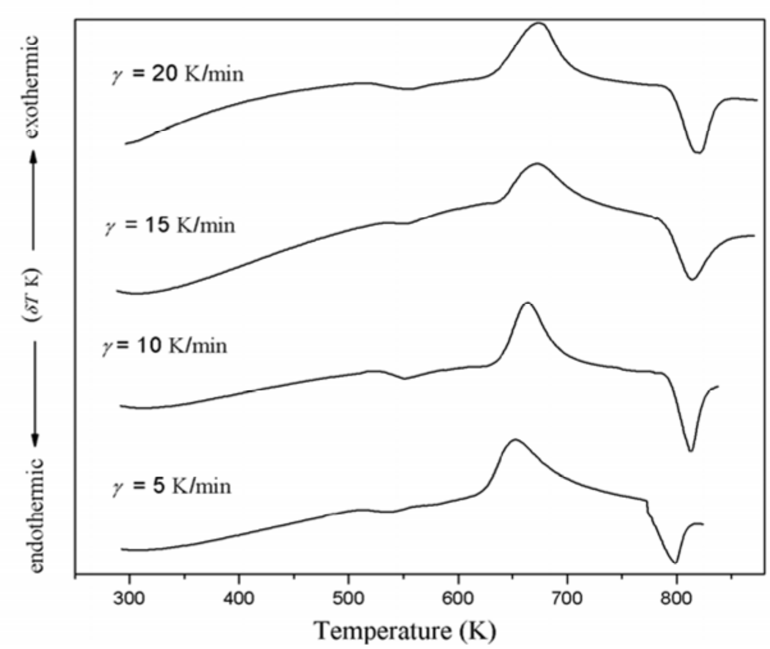

Figure 4.13 DTA trace for $Ge_{19}Se_{63.8}Sb_{17.2}$ alloys at heating rate of 5, 10, 15 and 20 K/min.

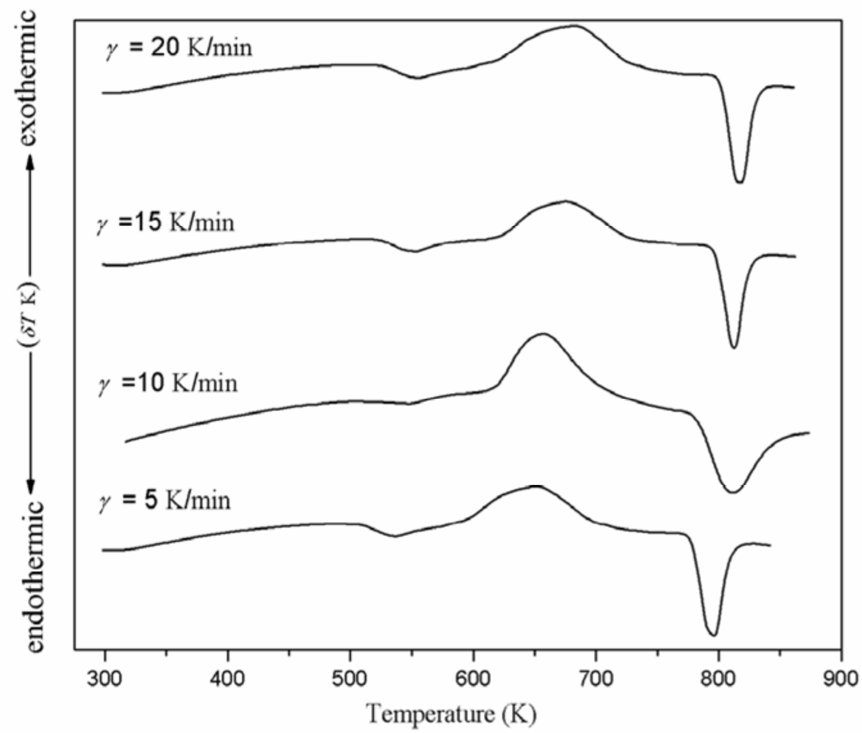

Figure 4.14 DTA thermograms for $Ge_{19}Se_{61}Sb_{20}$ alloys at heating rate of 5, 10, 15 and 20 K/min.

The values of T_g, T_c and T_m have been determined from Figures 4.8 to 4.14 and are given in Tables 4.6. The values of T_g, T_c and T_m (Table 4.6) have been found to increase up to $x = 17.2$ and thereafter decrease. T_c, T_g and T_m increase with increase in heating rate. Hence, peaks shift towards the higher temperature. T_g shows maximum at $x = 17.2$ which is similar to the result obtained from the physical study (section 4.1.2.2). The maximum value of T_g indicates that the polymeric chains get reduced and system becomes crosslinked. For $x = 17.2$, *Se* chains are completely crosslinked and structural units of tetrahedral $Ge(Se_{1/2})_4$ and trigonal Sb_2Se_3 are formed. Hence, system changes from two dimensional to three dimensional network. The maximum value of T_g at $x = 17.2$ may also be explained on account of presence of stable heteropolar bonds only. This makes the $x = 17.2$ composition most stable.

Table 4.6 Values of glass transition temperature (T_g), crystallization temperature (T_c) and melting temperature (T_m) for $Ge_{19}Se_{81-x}Sb_x$ (x = 0, 4, 8, 12, 16, 17.2, 20) glassy alloys at different heating rates (γ).

Samples	γ (K/min)	T_g (K)	T_c (K)	T_m (K)
x = 0	5	520.00	622.00	775.00
	10	530.00	636.00	784.00
	15	536.00	645.48	792.00
	20	540.00	654.34	799.00
x =4	5	524.00	627.00	780.00
	10	533.00	642.00	790.00
	15	540.00	651.00	796.00
	20	543.27	659.00	802.00
x =8	5	529.00	634.00	784.00
	10	537.00	647.00	795.00
	15	544.35	657.00	801.00
	20	548.00	665.00	806.00
x = 12	5	531.00	640.00	789.00
	10	540.00	653.5	801.00
	15	546.59	662.00	806.00
	20	549.67	671.00	811.00
x = 16	5	534.00	645.00	792.00
	10	543.00	657.61	806.00
	15	549.70	668.00	810.00
	20	552.00	675.00	817.00
x = 17.2	5	537.00	649.00	798.00
	10	546.00	663.72	812.00
	15	551.81	672.25	815.00
	20	555.44	679.18	821.00
x = 20	5	535.00	646.76	797.00
	10	544.00	659.93	810.00
	15	550.47	670.00	813.00
	20	553.00	676.82	819.00

4.3.2.2 Glass forming ability and reduced glass transition temperature

The glass forming ability (K_{gl}) is calculated from Hruby's parameter [183];

$$K_{gl} = \frac{T_c - T_g}{T_m - T_c} \tag{4.17}$$

where T_c-T_g represents the nucleation process and T_m-T_c indicates the growth process.

Reduced glass transition temperature (T_{rg}) has been calculated as [184];

$$T_{rg} = \frac{T_g}{T_m} \tag{4.18}$$

It has been observed that the obtained values (Table 4.7) obey the two third rule [184] which is; $T_g/T_m = 2/3$. T_{rg} values indicate the ease of glass formation in all samples.

The value of K_{gl} (Table 4.7) increases with the addition of *Sb* content till $x = 17.2$ and with further *Sb* addition K_{gl} decreases. The kinetic resistance towards the crystallization is higher for larger differences between T_c and T_g. There is an increase in difference between T_c and T_g up to $x = 17.2$ due to delay in nucleation process (slow crystallization). This leads to enhanced thermal stability and hence increases the glass forming ability.

Table 4.7 The characteristic parameters K_{gl} and T_{rg} at $\gamma = 10$ K/min. Values of A' and B' for $Ge_{19}Se_{81-x}Sb_x$ (x = 0, 4, 8, 12, 16, 17.2, 20) glassy alloys.

Samples	K_{gl}	T_{rg}	A'	B'
x = 0	0.716	0.676	496.72	14.47
x = 4	0.736	0.675	501.00	14.16
x = 8	0.743	0.675	506.11	13.93
x = 12	0.769	0.674	508.83	13.72
x = 16	0.772	0.674	512.49	13.39
x = 17.2	0.794	0.672	515.40	13.38
x = 20	0.773	0.672	513.59	13.32

The decreased nucleation rate leads to an increase in viscosity [185], implying that the glass forming ability increases up to x = 17.2 of *Sb*. With further addition of *Sb*, x = 20, difference between the two temperatures decreases causing rapid crystallization. On the basis of conductivity, *Sb* is semi–metal with higher conductivity. This decreases the difference between crystalline and glassy states and makes the glass less stable.

The dependence of glass transition temperature (T_g) on heating rate has been analyzed using empirical relation [186];

$$T_g = A' + B' \ln(\gamma) \tag{4.19}$$

where A', B' are constants and γ is the heating rate for the given chalcogenide glass compositions.

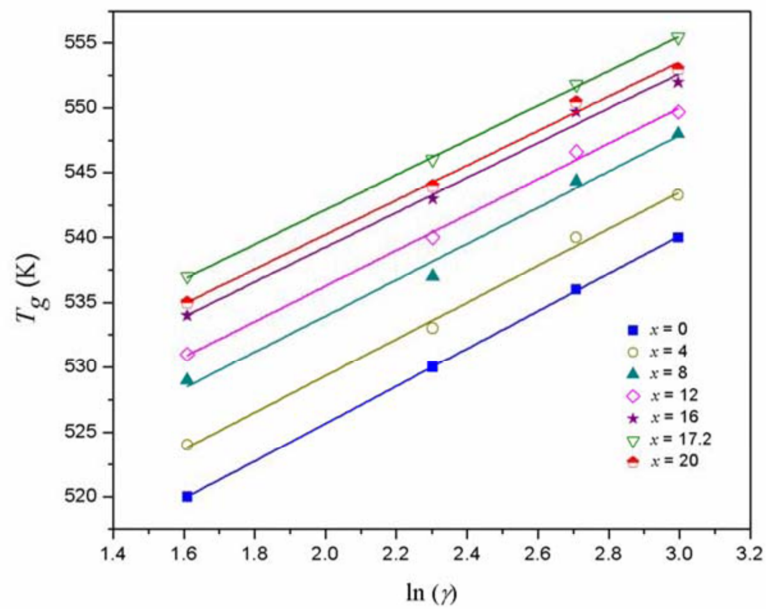

Figure 4.15 Plot of T_g *vs.* ln (γ) for $Ge_{19}Se_{81-x}Sb_x$ glasses.

The values of A' and B' have been obtained from the intercept and slope from Figure 4.15. The value of A' indicates the glass transition temperature and B' is related to the cooling rate of the melt. The lower the cooling rate of the melt, the lower will be the value of B'. The value of A' increases up to x = 17.2 and then decreases

(Table 4.7). The values of B' decrease from 14.47 to 13.32 with increase in *Sb* content indicating higher cooling rate of melt for the base composition.

4.3.2.3 Activation energy of glass transition temperature and crystallization temperature

The activation energy for glass transition temperature (E_g) is the amount of energy absorbed by a group of atoms in glassy region to jump from one metastable state to another. Two approaches have been used for the analysis of E_g depending on heating rate.

The first approach uses the Moynihan method (equation (2.1)) which is based on the theory of structural relaxation [124]. A plot between ln (γ) and $1000/T_g$ has been used to obtain E_g values (Figure 4.16).

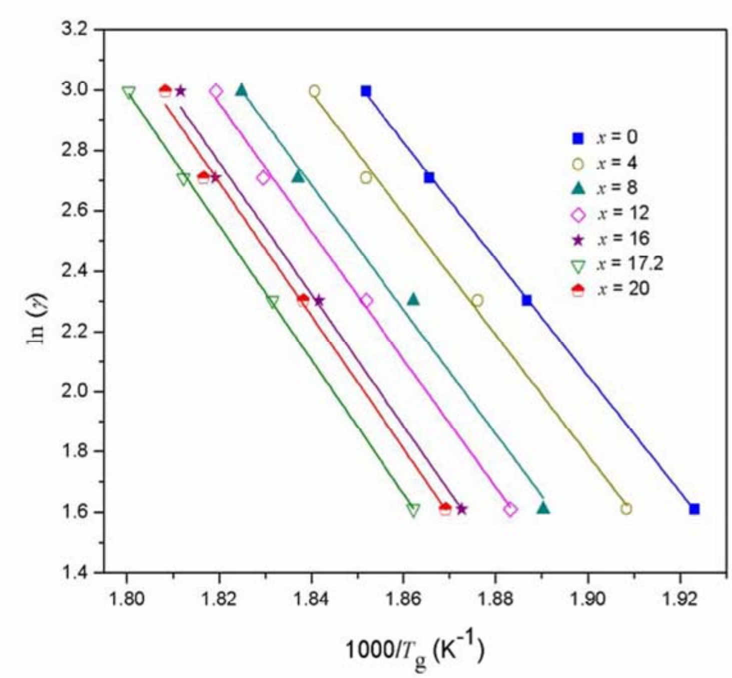

Figure 4.16 Variation of ln (γ) *vs.* $1000/T_g$ for $Ge_{19}Se_{81-x}Sb_x$ glasses.

The second approach utilizes Kissinger method (equation (2.3)). The slope of straight line in Figure 4.17 gives the value of E_g [125–127]. The values of E_g increases with *Sb* addition up to x = 17.2 and then decreases (Table 4.8). Heating rate dependence of T_g for chalcogenides has been interpreted in terms of thermal relaxation.

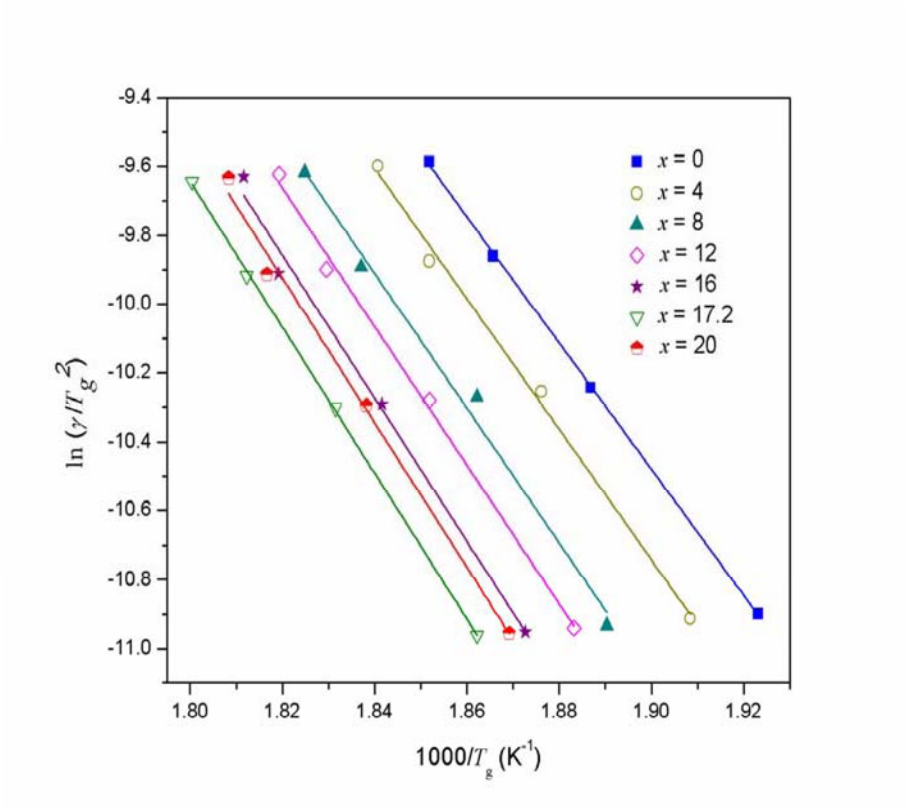

Figure 4.17 Plot of ln (γ/T_g^2) *vs.* 1000/T_g for $Ge_{19}Se_{81-x}Sb_x$ alloys.

The values in Table 4.8 obtained from the two methods are in good agreement with each other. This shows that the change of $\ln\left(\gamma/T_g^2\right)$ with 1000/T_g is negligibly small compared with the change of ln (γ). When the sample is heated in the furnace, atoms undergo transitions between the local potential minima (or metastable states). Hence, a structural change occurs in the glass and eventually leads to crystallization [73].

The activation energy for crystallization (E_c) deals with the nucleation and growth process that dominates the devitrification of most glassy solids. E_c has been analyzed using two methods. The first method, an approximation of Mahadevan, is obtained from Kissinger equation (equation (2.4)) [128]. The values of activation energy for the $Ge_{19}Se_{81-x}Sb_x$ system have been obtained from the plot of ln (γ) versus 1000/T_c (Figure 4.18).

Table 4.8 Values of activation energy for glass transition temperature (E_g) and activation energy for crystallization temperature (E_c) for $Ge_{19}Se_{81-x}Sb_x$ (x = 0, 4, 8, 12, 16, 17.2, 20) glassy alloys.

Samples	E_g kJmol^{-1} (Moynihan method)	E_g kJmol^{-1} (Kissinger method)	E_c kJmol^{-1} (Augis and Bennett method)	E_c kJmol^{-1} (Mahadevan method)
x = 0	161.24	152.42	146.52	141.27
x = 4	166.48	157.58	150.34	144.93
x = 8	171.64	162.66	157.00	151.67
x =12	176.30	167.32	162.08	156.67
x = 16	181.79	172.72	166.07	160.66
x = 17.2	185.29	176.22	169.31	163.82
x = 20	183.71	174.64	167.65	161.57

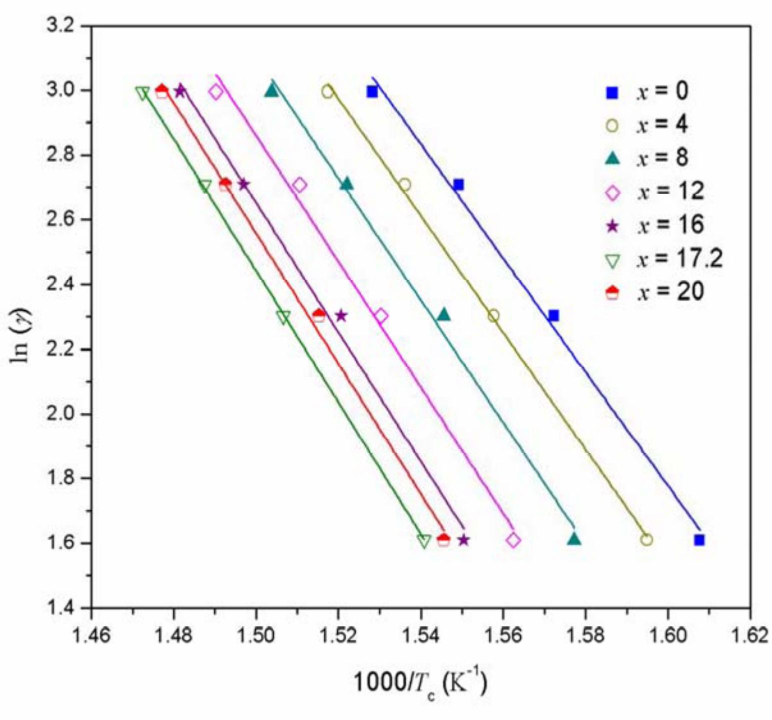

Figure 4.18 Plot of ln (γ) *vs.* 1000/T_c for $Ge_{19}Se_{81-x}Sb_x$ glasses.

The second method is an approximation developed by Augis and Bennett (equation (2.5)) [129]. Plot of $\ln(\gamma/T_c)$ versus $1000/T_c$ yield straight lines and the slope of lines give the value of activation energy (Figure 4.19). The intercept of plots give the values of K_o which measures the probability of a molecule with energy E_c to participate in a reaction. The values of activation energy for crystallization (E_c) from the two mentioned methods are in good agreement with each other. The value of E_c (Table 4.8) is maximum for x = 17.2 which can be explained on the basis of cohesive energy (*CE*). The values of *CE* are listed in Table 4.2 and are found to increase up to x = 17.2 followed by a decrease. The increase in E_c may be related to nucleation and growth process that requires more energy for the devitrification due to increasing value of *CE* of the glassy network. The glasses having *Sb* more than 17.2 at.% has higher tendency towards crystallization and therefore, the stability of glasses decreases for x > 17.2. Thus, for 20 at.% of *Sb,* the probability of the system towards devitrification increases and hence E_c decreases.

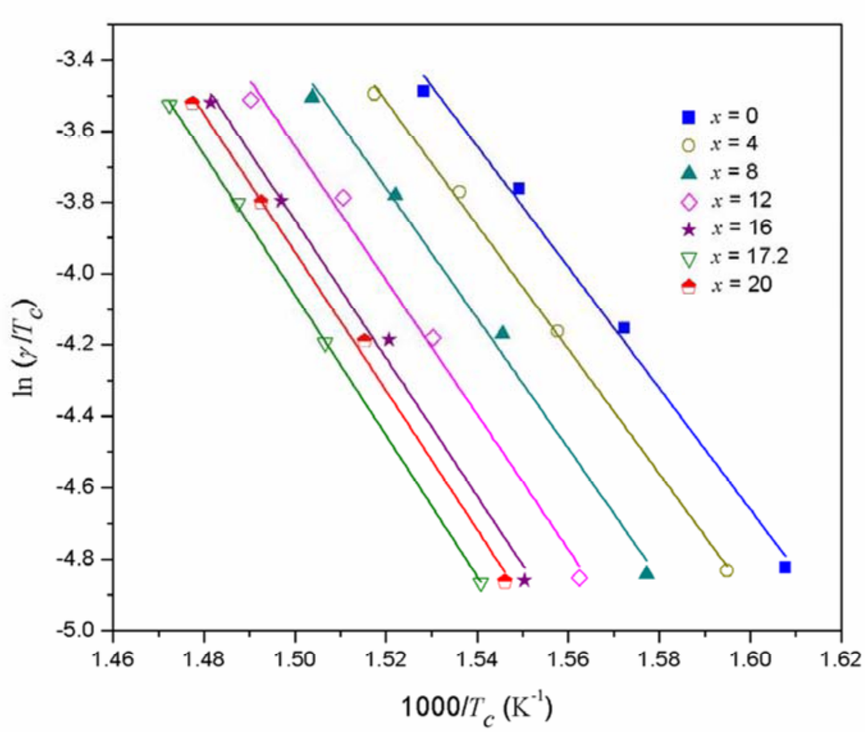

Figure 4.19 Variation of $\ln(\gamma/T_c)$ *vs.* $1000/T_c$ for $Ge_{19}Se_{81-x}Sb_x$ alloys.

4.4 Optical properties of *Ge–Se–Sb* thin films

Chalcogenide glasses have gained interest in the field of optics due to their numerous applications such as communication, sensing, imaging and etc [52, 61]. It is essential to know various parameters that are useful for fabrication and designing of devices. Two most important parameters are refractive index and optical band gap. Due to high refractive index and optical band gap lying in the sub–band gap region, chalcogenide glasses are used as core materials for optical fibres transmission purpose, especially when flexibility is required [187]. The influence of impurities in chalcogenide glasses is important with respect to the study of optical parameters. In this section, optical parameters of $Ge_{19}Se_{81-x}Sb_x$ (x = 0, 4, 8, 12, 16, 17.2, 20) thin films have been examined using UV–Vis–NIR spectroscopy.

4.4.1 Experimental details

Thin films of $Ge_{19}Se_{81-x}Sb_x$ glasses have been deposited on well cleaned microscopic glass substrates using vacuum thermal evaporation technique at a background pressure of ~10^{-4} Pa (Hindhivac Model No. 12A4D). The films have been kept inside the deposition chamber for 24 h to achieve metastable equilibrium. The transmission spectra of the thin films have been obtained using a double beam UV–Vis–NIR spectrophotometer (Perkin Elmer Lambda – 750). The slit width has been kept at 1 nm and all the measurements have been performed at room temperature (300K).

4.4.2 Results and discussion

4.4.2.1 Refractive index, absorption coefficient and optical band gap

Figure 4.20 shows the transmission spectra of $Ge_{19}Se_{81-x}Sb_x$ (where x = 0, 4, 8, 12, 16, 17.2, 20) thin films. From the spectra it is clear that with the addition of *Sb* to $Ge_{19}Se_{81}$ binary alloy, transmittance shifts to higher wavelengths *i.e.* red shift (Figure 4.21). The existence of red shift has also been confirmed from the Far–IR study. There is a shifting of absorption peaks toward the lower wavenumber with *Sb* addition.

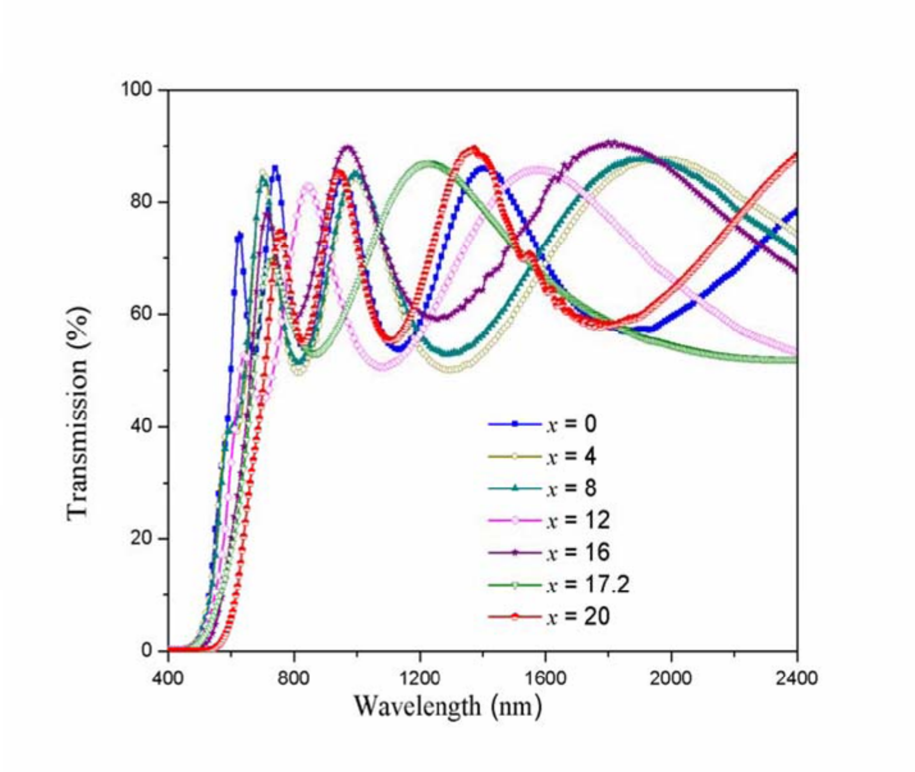

Figure 4.20 Transmission spectra for $Ge_{19}Se_{81-x}Sb_x$ thin films.

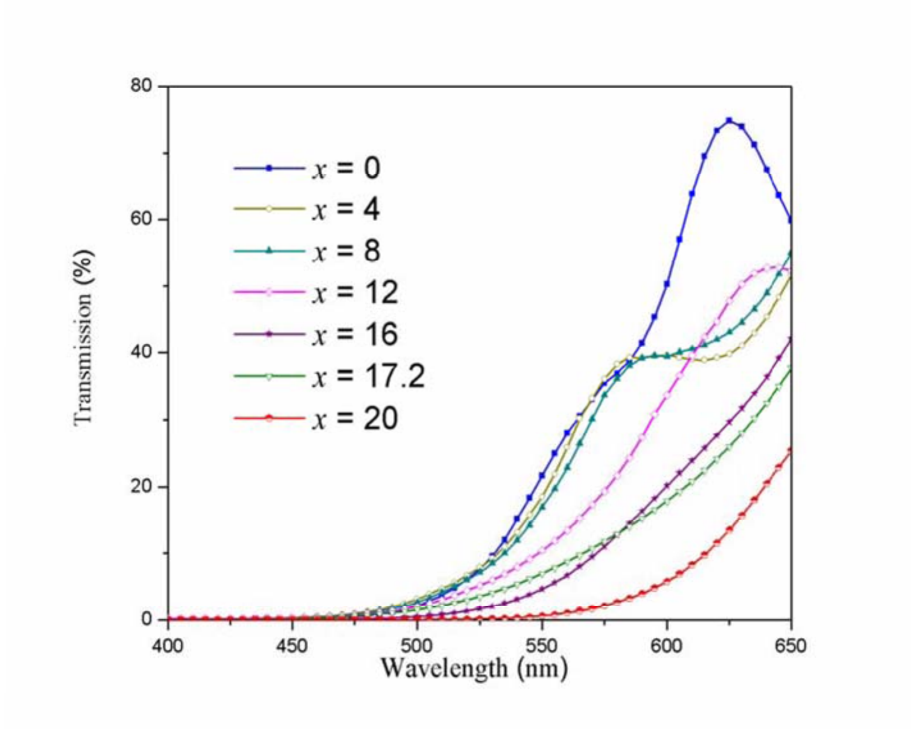

Figure 4.21 Transmission spectra showing a red shift for $Ge_{19}Se_{81-x}Sb_x$ thin films.

The shifting of spectra may be explained according to fundamental Kramers–Kronig relation that the red shift in spectrum must necessarily result in an increase in refractive index [188]. The refractive index (n) (equation (2.11)) and film thickness (equation (2.15)) of $Ge_{19}Se_{81-x}Sb_x$ system have been calculated from transmission spectra using Swanepoel's method [137], based on the approach of Manifacier [189].

The values of thickness (t) calculated from equation (2.15) have been used to determine t_{correc} by making use of the basic interference equation (Table 4.9) [138];

$$2nt_{correc} = m_o \lambda \tag{4.20}$$

where t_{correc} is corrected thickness, m_o the order parameter is an integer for maxima and a half order for minima in transmission spectra.

Table 4.9 Values of thickness (t_{correc}) and optical band gap (E_g^{opt}) for $Ge_{19}Se_{81-x}Sb_x$ thin films.

Samples	t_{correc} (nm)	E_g^{opt} (eV)
x = 0	576	1.96
x = 4	384	1.90
x = 8	368	1.86
x =12	304	1.77
x = 16	352	1.71
x = 17.2	227	1.57
x = 20	448	1.66

The values of refractive index have been fitted to Cauchy dispersion relationship (equation (2.12)). This relation has been used for extrapolation of the values of refractive index to all wavelengths. The refractive index of the system has been found to increase with the increasing content of Sb (Figure 4.22). The increase in refractive index has been explained on the basis of increased polarizability (α_p), *i.e.* the atom with larger atomic radius have large polarizability. Polarizability and refractive index are linked by Lorentz–Lorentz relation [190]

$$\frac{n^2 - 1}{n^2 + 2} = \frac{1}{3\varepsilon_0} \sum_j N_j \alpha_{p,j} \tag{4.21}$$

where ε_0 is the vacuum permittivity and N_j the number of polarizable units of type j per volume unit, with polarizability $\alpha_{p,j}$.

The atomic radius of *Se* is 1.15Å and *Sb* is 1.38Å. On replacing *Se* with *Sb* having higher atomic radius, increases the polarizability of system leading to an increase in refractive index of the system.

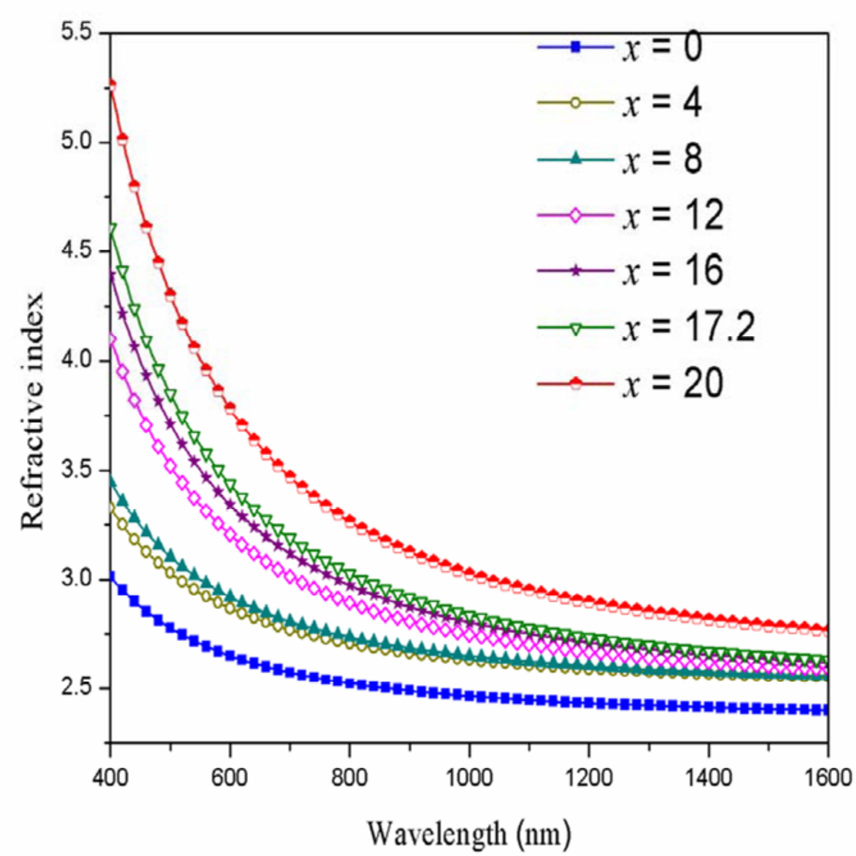

Figure 4.22 Variation of refractive index with wavelength for $Ge_{19}Se_{81-x}Sb_x$ thin films.

The extinction coefficient has been calculated using equation (2.14). From Figure 4.23, extinction coefficient as a function of wavelength shows a maximum for x = 17.2 at.% of *Sb* addition. The absorption coefficient (α) has been calculated using equation (2.16). Absorption coefficient has been found to increase up to x = 17.2 (Figure 4.24).

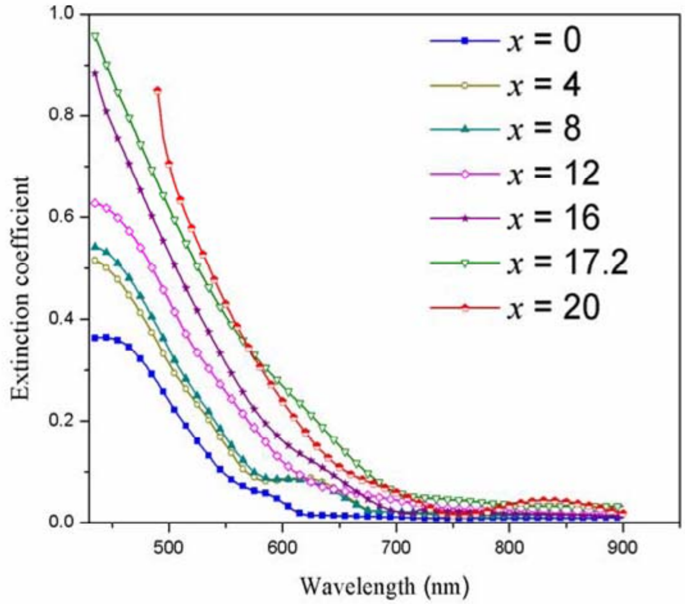

Figure 4.23 Variation of extinction coefficient with wavelength for $Ge_{19}Se_{81-x}Sb_x$ thin films.

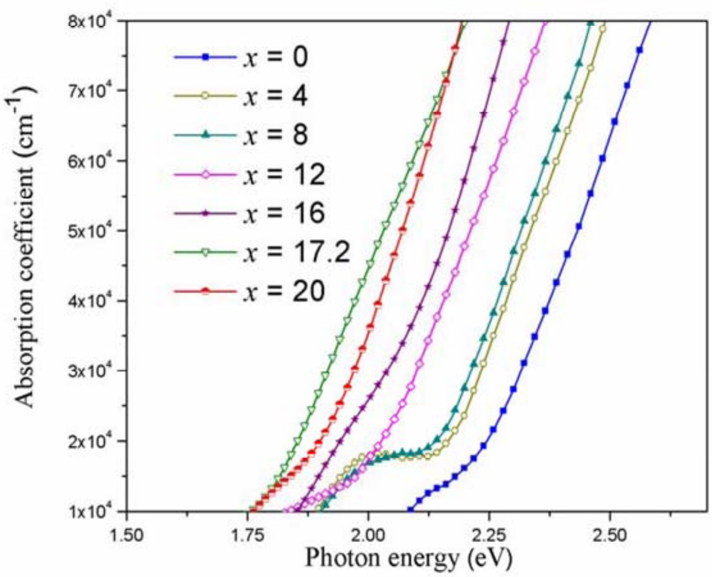

Figure 4.24 Variation of absorption coefficient with photon energy for $Ge_{19}Se_{81-x}Sb_x$ thin films.

Optical band gap (E_g^{opt}) has been determined according to the 'non–direct transition' model for amorphous semiconductors proposed by Tauc as given in equation (2.17) [143]. Variation of $(\alpha h\nu)^{0.5}$ with $h\nu$ has been shown in Figure 4.25. The optical band gap for non–direct transition has been obtained from intercept (extrapolation) $(\alpha h\nu)^{0.5}$ vs $h\nu$ with energy axis at $(\alpha h\nu)^{0.5} \rightarrow 0$. It has been clear from the figure that E_g^{opt} decreases to minimum at x = 17.2 followed by an increase on further addition of *Sb* content (Table 4.9). Decrease in optical band gap up to x = 17.2 at.% of *Sb* addition has been explained on the basis of valence alternation pair (D^+, D^-). These strained and dangling bonds lead to the formation of localized states in the gap, which ultimately decreases the optical band gap of the system.

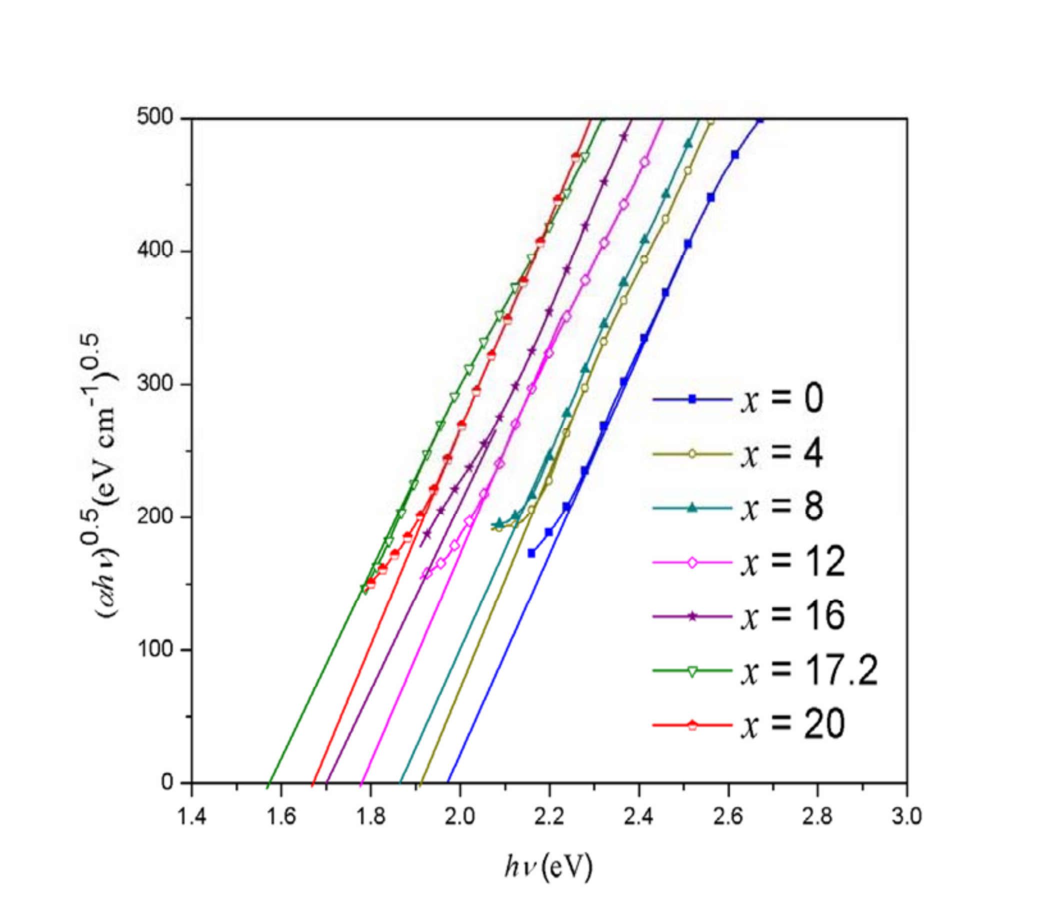

Figure 4.25 Variation of $(\alpha h\nu)^{0.5}$ with $h\nu$ for $Ge_{19}Se_{81-x}Sb_x$ thin films.

4.4.2.2 Dispersion parameters and optical conductivity

Dispersion of refractive index has been analysed using Wemple Di–Domineco single–effective–oscillator (WDD) model (equation (2.19)) [145, 146]. The values of average energy gap (E_o) and dispersion energy (E_d) have been calculated by fitting a straight line in graph between $(n^2-1)^{-1}$ and $(hv)^2$ as shown in Figure 4.26.

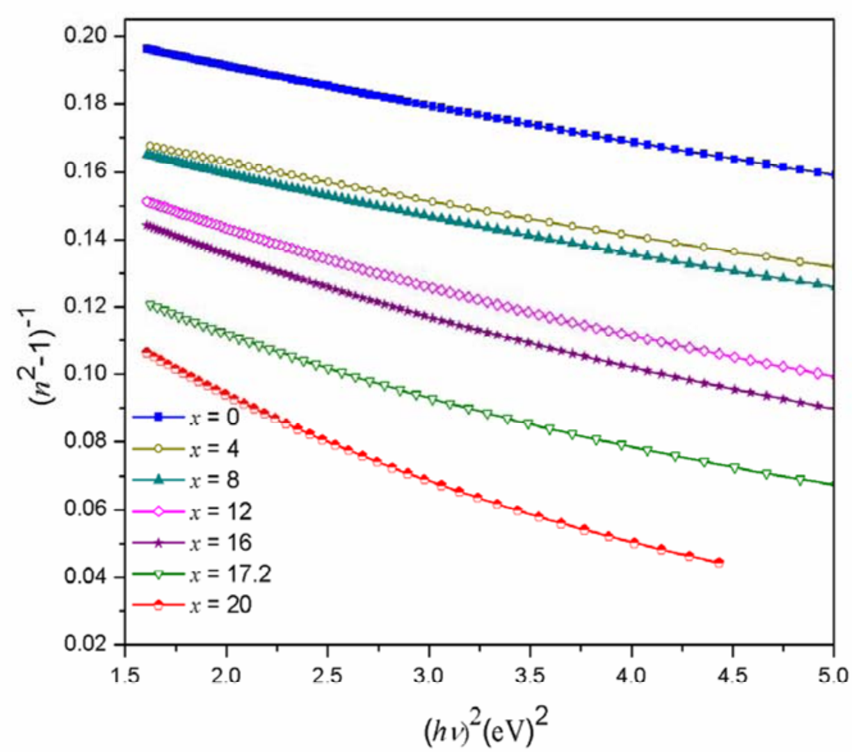

Figure 4.26 Plot of $(n^2-1)^{-1}$ with $(hv)^2$ for $Ge_{19}Se_{81-x}Sb_x$ thin films.

The values for static refractive index (n_o) have been calculated from E_o and E_d parameters using the relation [146];

$$n_0 = \left(1 + \frac{E_d}{E_o}\right)^{1/2} \tag{4.22}$$

The values of n_o have been calculated by extrapolating the WDD dispersion equation to $hv \to 0$. The values of E_d, E_o and static refractive index have been given in Table 4.10.

Table 4.10 Values of dispersion energy (E_d), average energy gap (E_o) and static refractive index (n_o) for $Ge_{19}Se_{81-x}Sb_x$ thin films.

Samples	E_d (eV) WDD	E_o (eV)	n_o
$x = 0$	21.9	4.60	2.40
$x = 4$	24.9	4.46	2.54
$x = 8$	23.5	4.19	2.56
$x = 12$	21.69	3.61	2.65
$x = 16$	21.87	3.48	2.70
$x = 17.2$	21.88	3.41	2.72
$x = 20$	24.54	3.27	2.92

An important achievement of WDD model is that it relates the dispersion energy to other physical parameters of the material through the relation given in equation 2.20 [146]. The values coordination number of the cation nearest neighbor to anion (N_c'), effective number of valence electrons per anion (N_e), formal chemical valency of anion (Z_a) for $Ge_{19}Se_{81}$ have been calculated by rewriting the chemical composition as $(Ge_1)_{19}(Se_1)_{81}$, $N_c' = 1*4 = 4$, $N_e = (19*4 + 81*6)/81 = 6.94$, $Z_a = 2$, $E_d = 22.21$ eV. By considering one more composition containing *Sb*, $Ge_{19}Se_{69}Sb_{12}$ with chemical composition $(Ge_{0.613}Sb_{0.387})_{31}Se_{69}$, $N_c' = 0.613*4 + 0.387*3 = 3.6$, $N_e = (19*4 + 69*6 + 12*5)/69 = 8.0$, $E_d = 23.12$ eV. The value of E_d increases with the increase of *Sb* content. It is known that the larger the difference in electronegativity (χ) (Pauling electronegativity) between the two atoms involved in a bond; the more is the ionic character. The addition of *Sb* causes the system to be less ionic, because *Sb–Se* bond is less ionic than the *Ge–Se* bond and hence smaller s–p splitting increases the parameter N_e [145]. This shows that the N_e in the system increases with the increasing content of *Sb*. The addition of *Sb* to *GeSe* matrix increases one or other quantity on the right hand side of equation (2.20) [190]. In *Ge–Se–Sb* glassy alloys, dispersion energy increases due to increasing value of parameter N_e with *Sb* addition.

The Kramers–Kronig relation, $n_o = 1 + \left(\frac{1}{2\pi^2}\right)\int_0^\infty \alpha(\lambda) d\lambda$, checks the consistency of the values of static refractive index and relative positions of the optical absorption edges [191]. In this system, the values of n_o are increasing which shows the area under the absorption curve is larger. Hence, it is clear that the transmittance shifts to the longer side of the wavelength. As the real and imaginary part of dielectric constant is related to refractive index and absorption coefficient (α) respectively, hence, an increase in the value of α indicates that the absorption edge shifts towards the longer wavelength. The occurrence of the red shift with the addition of *Sb* content signifying an increased in density of localized states in forbidden gap up to $x = 17.2$.

According to Tanaka, average energy gap is related to optical band gap by the relation $E_0 \approx 2\times E_g^{opt}$ [192]. It has been clear from the Table 4.10 that the values obtained by Tanaka's relation are in good agreement with those obtained from Tauc extrapolation. The decrease in optical band gap has been explained on the fact that with the addition of *Sb* there is sharp change in mobility gap which causes large disorder. Band tail of valence band and conduction band overlap in mobility gap and leads to decrease of optical band gap. The parameter *B* in equation (2.17) indicates the degree of structural randomness of amorphous semiconductors [188], and is related with the localized–state tail width (ΔE), through the relationship suggested by Mott and Davis [193]:

$$B = \frac{4\pi\sigma_{\min}}{n_o c\Delta E} \tag{4.23}$$

where σ_{min} is the minimum electrical conductivity, n_o is static refractive index and c is the speed of light in vacuum. The values of $B^{1/2}$ has been derived from Tauc's plots are listed in Table 4.11. The values of $B^{1/2}$ decreases up to $x = 17.2$ and then increases. It has been observed that the degree of structural randomness decreased to a minimum for x =17.2 due to which localized–state tail width increases and with the further addition of *Sb*, ΔE decreases. The variation in E_g^{opt} can also be explained on the basis of variation in localized–state tail width. Since, E_g^{opt} varies inversely with ΔE.

The complex dielectric constant is a fundamental intrinsic material property [48]. The real part of the dielectric constant is related to the energy stored with in the medium and the imaginary part is related to the dissipation (or loss) of energy with in the medium. The complex dielectric constant [146]; $\varepsilon = \varepsilon_r - \varepsilon_i = (n - ik)^2$ where

ε_r is the real part of dielectric constant $(\varepsilon_r = n^2 - k^2)$ & ε_i is the imaginary part of dielectric constant $(\varepsilon_i = 2nk)$.The loss factor has been expressed on the basis of real and imaginary part of dielectric constant and defined as the ratio of imaginary part of dielectric to the real part of dielectric constant. The larger the imaginary constant, larger will be the loss factor.

Dielectric loss tangent (*tan δ*) can be calculated [194];

$$\tan\delta = \frac{\varepsilon_i}{\varepsilon_r} \tag{4.24}$$

The dissipation energy (*tan δ*) of the system increases up to x = 17.2 and then decreases (Table 4.11). This shows an increase in loss of light up to x = 17.2 and thereafter decreases.

Table 4.11 Values of tailing parameter ($B^{1/2}$) and loss tangent (*tan δ*) for $Ge_{19}Se_{81-x}Sb_x$ (x = 0, 4, 8, 12, 16, 17.2, 20) thin films.

Samples	$B^{1/2}$ ($cm^{-1/2}$ $eV^{-1/2}$)	*tan δ*
x = 0	1212	0.0311
x = 4	1121	0.0586
x = 8	925	0.0598
x =12	762	0.0754
x = 16	734	0.0967
x = 17.2	683	0.1578
x = 20	784	0.1268

Optical conductivity (σ) of the material has been determined as [195];

$$\sigma = \frac{\alpha nc}{4\pi} \tag{4.25}$$

where α is absorption coefficient, n is refractive index and c is the velocity of light. It has the dimensions of frequency. Figure 4.27 shows that the σ increases up to x = 17.2 at.% of *Sb* addition and then decreases with increasing energy. The decrease in optical band gap (according to *density of states model*) affecting optical conductivity of the system, which has been found to increase [193]. Due to which the addition of *Sb* to *Ge–Se* system increases the number of charged defect states, which may affect the dielectric properties. These paired defect states behave as dipoles in present glassy alloys. With the increase in number of dipoles up to x = 17.2, dielectric loss also increases [196].

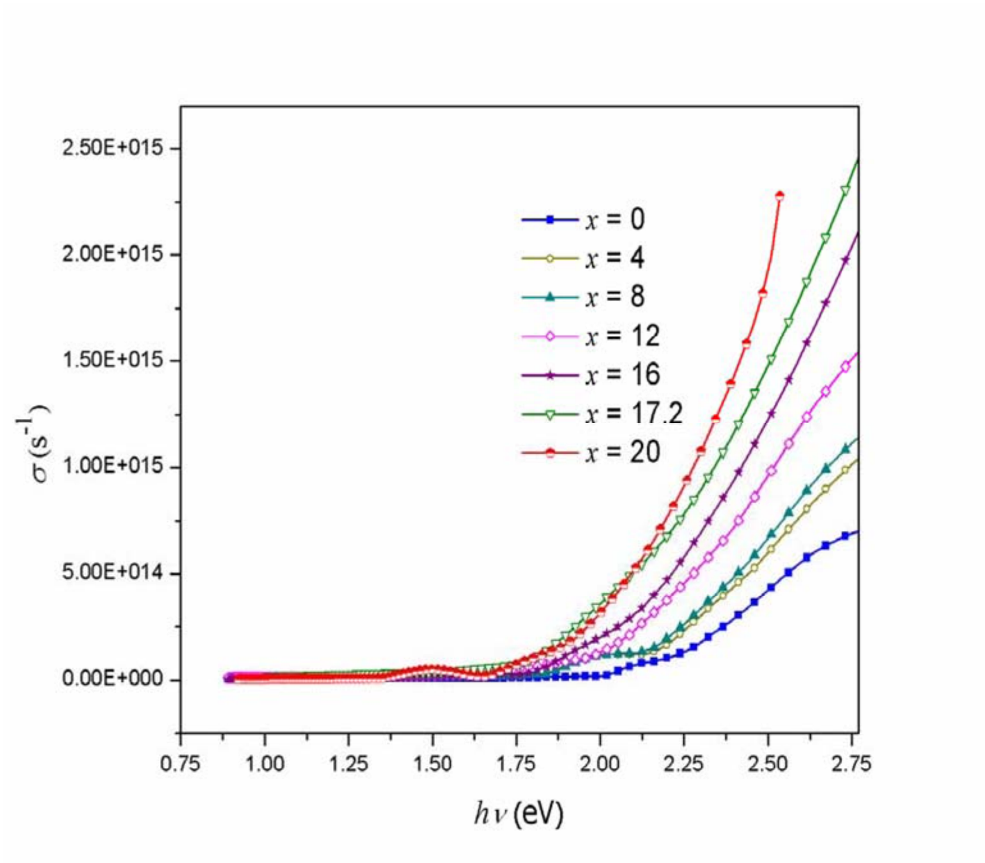

Figure 4.27 Variation of optical conductivity with photon energy for $Ge_{19}Se_{81-x}Sb_x$ thin films.

4.4.2.3 Non–linear refractive index

Chalcogenide glasses are highly dependent on intensity and show large values of non–linear refractive index (n_2). When matter is exposed to intense electric field, polarization is no longer proportional to electric field and the change in polarizability has to be extended by terms proportional to square of electric field. n_2 has been calculated using two methods; (a) Tichy and Ticha [197] (b) Fournier and Snitzer [198].

(a) Tichy and Ticha relation

This relation is a combination of Miller's generalized rule and static refractive index obtained from WDD model [197];

$$n_2 = \frac{12\pi\chi^{(3)}}{n_o} \tag{4.26}$$

where $\chi^{(3)}$ is third order susceptibility and n_0 is static refractive index. $\chi^{(3)}$ has been given by Miller's generalized rule: $\chi^{(3)} \cong A(\chi^1)^4$ where A is 1.7×10^{-10} (when χ is in esu) and $\chi^{(1)}$ is linear susceptibility [199]. $\chi^{(3)}$ is given as;

$$\chi^{(3)} = \frac{A}{(4\pi)^4}\left(n_o^2 - 1\right)^4 \tag{4.27}$$

Values of $\chi^{(3)}$ have been found to increase with *Sb* addition as can be seen from Figure 4.28. Values of n_2 have been listed in Table 4.12 and are found to increase.

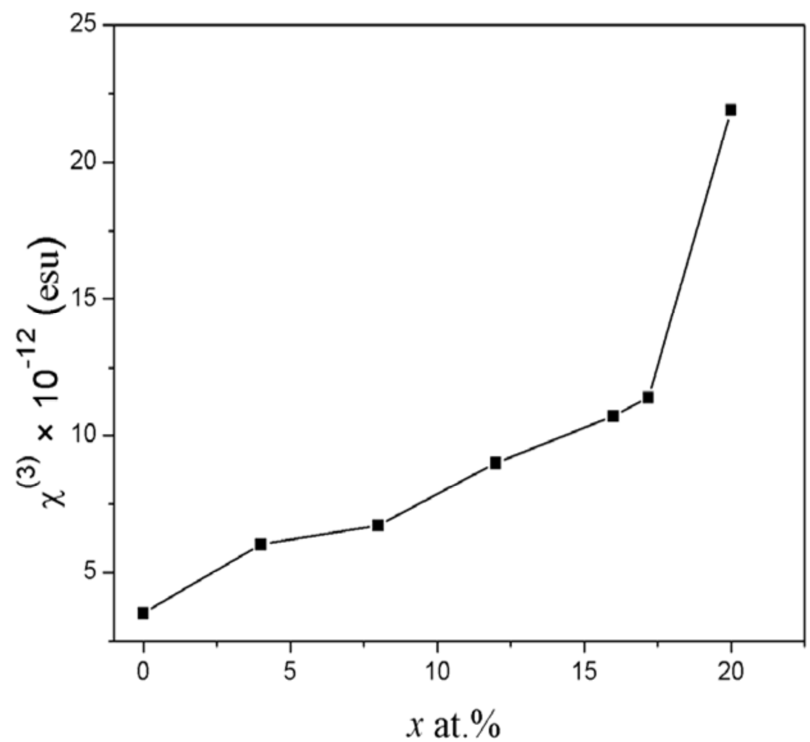

Figure 4.28 Variation of $\chi^{(3)}$ with *Sb* composition for $Ge_{19}Se_{81-x}Sb_x$ (x = 0, 4, 8, 12, 16, 17.2, 20).

Table 4.12 Values of non–linear refractive index (Tichy and Ticha method), *N′* and non–linear refractive index (Fournier and Snitzer method) for $Ge_{19}Se_{81-x}Sb_x$ (x = 0, 4, 8, 12, 16, 17.2, 20).

Samples	n_2 (esu) (Tichy and Ticha method)	$N'\times10^{22}$ (cm^{-3})	$n_2\times10^{-09}$ (esu) at 1.55 eV (Fournier and Snitzer method)
$x = 0$	5.52×10^{-11}	3.787	2.55×10^{-10}
$x = 4$	8.95×10^{-11}	3.766	4.23×10^{-10}
$x = 8$	9.88×10^{-11}	3.740	4.78×10^{-10}
$x = 12$	1.28×10^{-10}	3.719	7.67×10^{-10}
$x = 16$	1.49×10^{-10}	3.694	9.49×10^{-10}
$x = 17.2$	1.59×10^{-10}	3.693	1.07×10^{-9}
$x = 20$	2.83×10^{-10}	3.680	1.85×10^{-9}

(b) Fournier and Snitzer

Fournier and Snitzer proposed a formula to determine n_2 using linear refractive index and WDD parameters (E_o, E_d) in following relation [198];

$$n_2 = \frac{(n^2+2)^2(n^2-1)E_d}{48\pi nN'(E_o)^2} \tag{4.28}$$

where *N′* is density of polarizable constituents. *N′* has been found to decrease with increasing *Sb* content (Table 4.12). The values of n_2 have been found to increase with the addition of *Sb* content (Figure 4.29).

According to Moss rule, non–linearity can be determined from optical band gap values as; $n_2 \propto 1/(E_g^{opt})^4$ [200]. The optical band gap of $Ge_{19}Se_{81-x}Sb_x$ (x = 0, 4, 8, 12, 16, 17.2, 20) system decreases with the addition of *Sb* content. Also the formation of homopolar bonds is responsible for the decrease in optical band gap that ultimately increases the non–linear refractive index.

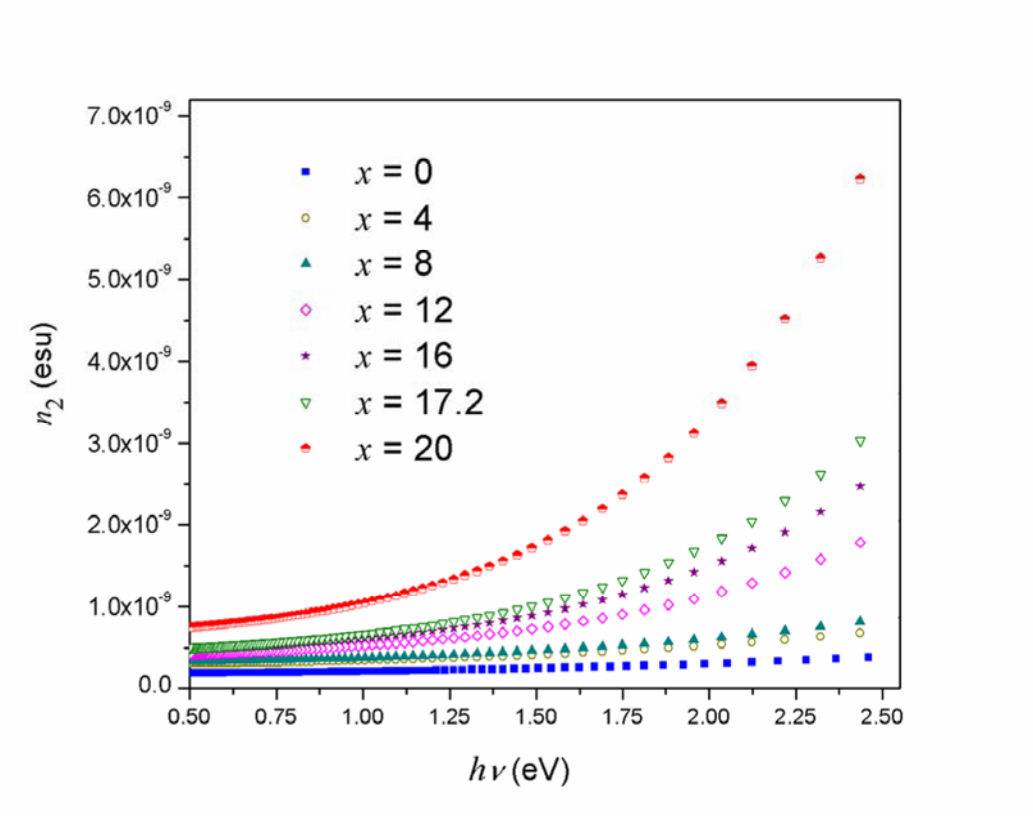

Figure 4.29 Variation of n_2 with $h\nu$ for $Ge_{19}Se_{81-x}Sb_x$ system.

5. Conclusion

- Physical parameters indicate that with the addition of *Sb* content, crosslinking of the structure increases due to which average coordination number and rigidity increase. Lone–pair electrons decrease with *Sb* addition. Glass transition temperature and cohesive energy is maximum at the stoichiometric composition (x = 17.2 at.%). Theoretical energy gap and electronegativity have been found to decrease with the addition of *Sb* content. Density and molar volume of the system increase with increasing *Sb* content.
- Far–IR study indicates that with the addition of *Sb* new modes $SbSe_3$ and *Sb*–*Se* bonds have been observed. The prominent structural units are $GeSe_4$ and $SbSe_3$ and for x = 17.2 system gets crosslinked. From the relative bond distribution, it has been observed that for x > 17.2, *Sb*–*Sb* homopolar bonds appear which are in good agreement with the result obtained from Far–IR study at 156 cm^{-1}.

- Thermal analysis reveals that T_g, T_c and T_m shows maximum at x = 17.2 for $Ge_{19}Se_{81-x}Sb_x$ glassy alloys. These three parameters increase with increasing heating rate. The results indicate that both the thermal stability and glass forming ability are maximum for 17.2 at.% of *Sb* content. The values of activation energy of glass transition temperature and crystallization temperature show maximum for x = 17.2 at.% of *Sb*.
- In optical study a red shift has been observed with increasing *Sb* additive. The refractive index and extinction coefficient have been found to increase with increasing *Sb* content. The optical band gap has been observed to decrease up to x = 17.2 and thereafter increases. Dielectric loss tangent and optical conductivity increase to a maximum for 17.2 at.% of *Sb*. The non–linear refractive index and susceptibility increase when *Se* is substituted with *Sb*.

CHAPTER 5

Physical, structural, thermal and optical properties of quaternary chalcogenide glassy semiconductors

- **Neha Sharma**, Sunanda Sharda, S.C. Katyal, Vineet Sharma and Pankaj Sharma, "*Effect of Te on linear and non-linear optical properties of new quaternary Ge−Se−Sb−Te chalcogenide glasses*" 2013 **Electronic Materials Letters** DOI: http://dx.doi.org/10.1007/s13391-013-3168-1 (*in press*).
- **Neha Sharma**, Sunanda Sharda, Vineet Sharma and Pankaj Sharma, "*Far−Infrared Investigation of Ternary Ge−Se−Sb and Quaternary Ge−Se−Sb−Te Chalcogenide Glasses*" **Journal of Non–Crystalline Solids**, 375 (2013) 114–118.
- **Neha Sharma**, Sunanda Sharda, Vineet Sharma and Pankaj Sharma, "*Evaluation of Physical Parameters for New Quaternary $Ge_{19-y}Se_{63.8}Sb_{17.2}Te_y$ Chalcogenide Glasses*" **Chalcogenide Letters,** 9 (2012) 355–363.
- **Neha Sharma**, Sunanda Sharda, Vineet Sharma and Pankaj Sharma, "*Glass transition and crystallization kinetics for $Ge_{19-y}Se_{63.8}Sb_{17.2}Te_y$ multi−component glassy alloys*" (2013) [**communicated**].

This chapter describes the physical and structural properties of the $Ge_{19\text{-}y}Se_{63.8}Sb_{17.2}Te_y$ (y = 0, 2, 4, 6, 8, 10) system. The thermal and optical characteristics have also been studied and presented.

The physical, structural, thermal and optical properties for $Ge_{19}Se_{81\text{-}x}Sb_x$ (x = 0, 4, 8, 12, 16, 17.2, 20) system discussed in chapter 4 indicate that ternary glasses with 19 at.% of *Ge* has the highest glass transition temperature at an *Sb* content of x = 17.2 at.%. This is also consistent with the network backbone being fully polymerized (Figure 4.3). Two intrinsic factors restricting the transparency of glasses in UV–Visible and infrared region. (i) Electronic absorption that affects the transparency in UV–Visible region. (ii) Phonon absorption (due to vibrational modes) which occurs in infrared region [136]. *Te* has low phonon energy due to its high atomic weight and has transparency up to 25 μm [61]. Hence, *Te*–based glasses find applications at longer wavelength in IR region such as CO_2 infrared sensing at 15 μm and outer space life detection [61]. *Te* based glasses are suitable for integrated optics and optical storage due to high refractive index, photosensitivity and rapid amorphous–to–crystalline transformation [201]. Therefore, *Te* has been added to the most stable composition of ternary system. For the understanding of thermal and optical properties for $Ge_{19\text{-}y}Se_{63.8}Sb_{17.2}Te_y$ (y = 0, 2, 4, 6, 8, 10) system, it is important to determine the physical parameters. In the first section, physical parameters for $Ge_{19\text{-}y}Se_{63.8}Sb_{17.2}Te_y$ (y = 0, 2, 4, 6, 8, 10) system have been calculated.

5.1 Physical properties of *Ge–Se–Sb–Te* chalcogenide glasses

The physical parameters have been determined for $Ge_{19\text{-}y}Se_{63.8}Sb_{17.2}Te_y$ (y = 0, 2, 4, 6, 8, 10) system. These parameters are; average coordination number (m), number of constraints (N_c), lone–pair of electrons (L), mean bond energy $\langle E \rangle$ and glass transition temperature (T_g). The cohesive energy (CE), heat of atomization (H_s) and theoretical energy gap (E_g^{th}), electronegativity (χ), density (ρ) and molar volume (V_m) have been evaluated.

5.1.1 Experimental details

Bulk samples of $Ge_{19\text{-}y}Se_{63.8}Sb_{17.2}Te_y$ (y = 0, 2, 4, 6, 8, 10) have been synthesized in which constituent elements *viz. Ge*, *Se*, *Sb*, *Te* weighed according to their atomic weight percentage and sealed in quartz ampoules evacuated to ~ 10^{-4} Pa. The detail of melt quench technique has been explained in section 4.1.1.

5.1.2 Results and discussion

5.1.2.1 Average coordination number and number of constraints

The bonding character in the nearest–neighbor region, *i.e.* average coordination number (m), characterizes the electronic properties of semiconducting materials. In the quaternary glasses, the average coordination number for covalently bonded materials has been calculated using equation (4.1) [202]. The *Ge* element with higher coordination number has been replaced with *Te* having lower coordination number (N_{Te} = 2,) due to which the average coordination number of the system decreases.

Table 5.1 Values of average coordination number (m), number of constraints (N_c), mean bond energy <E> and degree of covalency (C_c) (%) for $Ge_{19-y}Se_{63.8}Sb_{17.2}Te_y$ (y = 0, 2, 4, 6, 8, 10).

Samples	m	N_a	N_b	N_c	<E> (eV)	Bonds	C_c (%)
y = 0	2.55	1.28	2.10	3.38	2.61	*Ge–Se*	92.97
y = 2	2.51	1.26	2.02	3.28	2.55	*Te–Se*	95.06
y = 4	2.47	1.24	1.94	3.18	2.49	*Sb–Se*	93.94
y = 6	2.43	1.22	1.86	3.08	2.42	*Te–Ge*	99.80
y = 8	2.39	1.20	1.78	2.98	2.36	*Sb–Ge*	99.96
y = 10	2.35	1.18	1.70	2.88	2.30	*Te–Sb*	99.94

The total number of constraints per atom has been calculated using equation (4.4). According to constraints theory, chalcogenides has been classified into three groups:

(1) floppy or under–coordinated glasses with $m < 2.4$ and $N_c < 3$;

(2) optimally–coordinated or ideal glasses with $m = 2.4$ and $N_c = 3$;

(3) stressed–rigid and over–coordinated glasses with $m > 2.4$ and $N_c > 3$.

The values of m and N_c decrease from 2.55 to 2.35 and 3.38 to 2.88 respectively with increasing Te content (Table 5.1). Pure Se consists of mixture of polymeric chain and rings. On the addition of Te to Ge–Se–Sb ternary system, $Ge(Se_{1/2})_4$ tetrahedral units, Se_6Te_2 rings and Sb_2Se_3 trigonal units are expected to be formed. For $Te \leq 6$, system has been found to be stressed–rigid or over–coordinated and when $Te > 6$, the system behaves as floppy or under–coordinated glasses. This system has been found to be highly defective due to the deviation of the value of number of constraints from $N_c = 3$ [201].

5.1.2.2 Lone–pair electrons, deviation to stoichiometry, mean coordination number, degree of covalency and glass transition temperature

Lone–pair electrons indicate the flexibility in the system and have been calculated from equation (4.5). Lone–pair electrons increase with the addition of Te (Figure 5.1) to the ternary glass system.

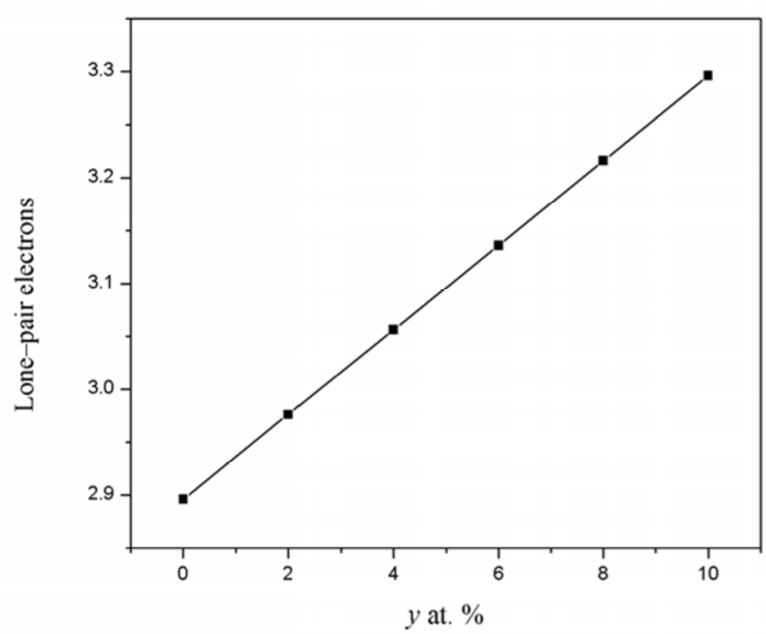

Figure 5.1 Lone–pair electrons variation with Te content for $Ge_{19-y}Se_{63.8}Sb_{17.2}Te_y$ (y = 0, 2, 4, 6, 8, 10).

This is due to the increase in interaction between *Ge* atoms and lone–pair electrons of *Te*. Strain energy in the glass system decreases with increasing number of lone–pair electrons. So, the larger number of lone–pair electrons in the structure favors stable glass formation [203].

Parameter R determines the deviation from stoichiometry and is expressed by the ratio of covalent bonding possibilities of chalcogen atom to non–chalcogen atom (equation (4.6)). The increase in the value of R on *Te* addition indicates that the system is chalcogen rich.

Mean bond energy $<E>$ (equation (4.7)) is the sum of mean bond energy of the average crosslinking per atom (heteropolar bonds) $<E_c>$ and the average bond energy per atom of the remaining matrix $<E_{rm}>$. The value of $<E>$ has been calculated using equation (4.7) [178]. Bond energy values of heteropolar bonds have been calculated using Pauling relation (equation (4.8)) [162]. The values of $<E>$ have been listed in Table 5.1.

The degree of covalency (C_c) of bonds has been calculated using relation [201];

$$C_c = 100\exp\left[\frac{-(\chi_A - \chi_B)^2}{4}\right] \tag{5.1}$$

where χ_A, χ_B are the electronegativities of involved *A* and *B* atoms. The values of C_c have been listed in Table 5.1 and are found to increase with *Te* addition. C_c depends on the electronegativity and it increases with the smaller χ difference between the bonds.

The glass transition temperature (T_g) is an important parameter that represents the strength and rigidity of glass structure. Glass transition temperature has been calculated using Gibbs–DiMarzio model [204]. Gibbs and DiMarzio proposed an empirical relationship between the transition temperature and the density of crosslinking agents embedded inside a system. The modified Gibbs–DiMarzio equation is [204]

$$T_g = \frac{T_o}{1-\beta(m-2)} \tag{5.2}$$

where T_o is the glass transition temperature of the chalcogenide element and β is a system constant. Figure 5.2 indicates that R increases while T_g decreases with decreasing value of m (Figure 5.3).

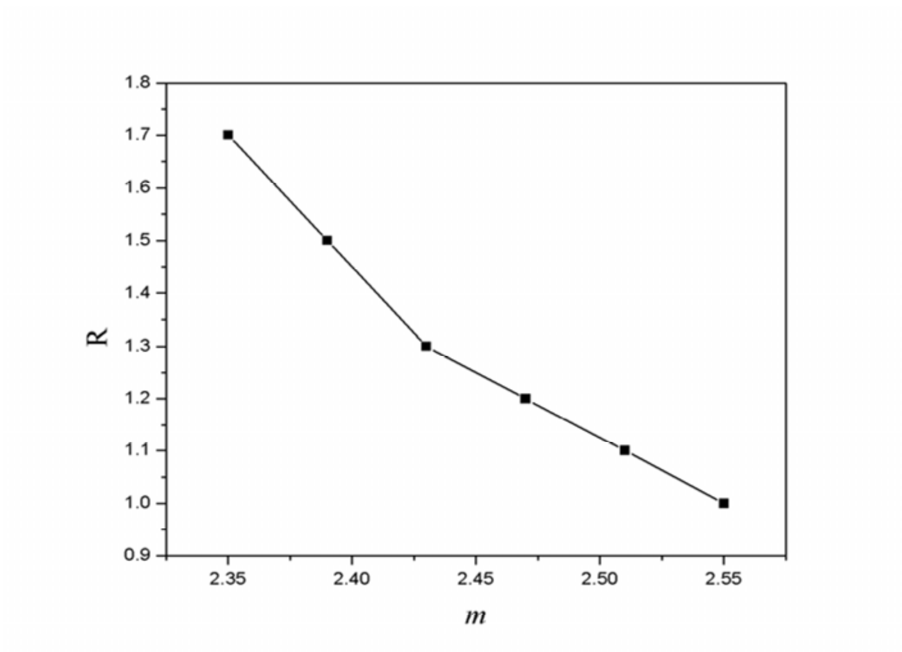

Figure 5.2 Variation of R with m for $Ge_{19-y}Se_{63.8}Sb_{17.2}Te_y$ (y = 0, 2, 4, 6, 8, 10).

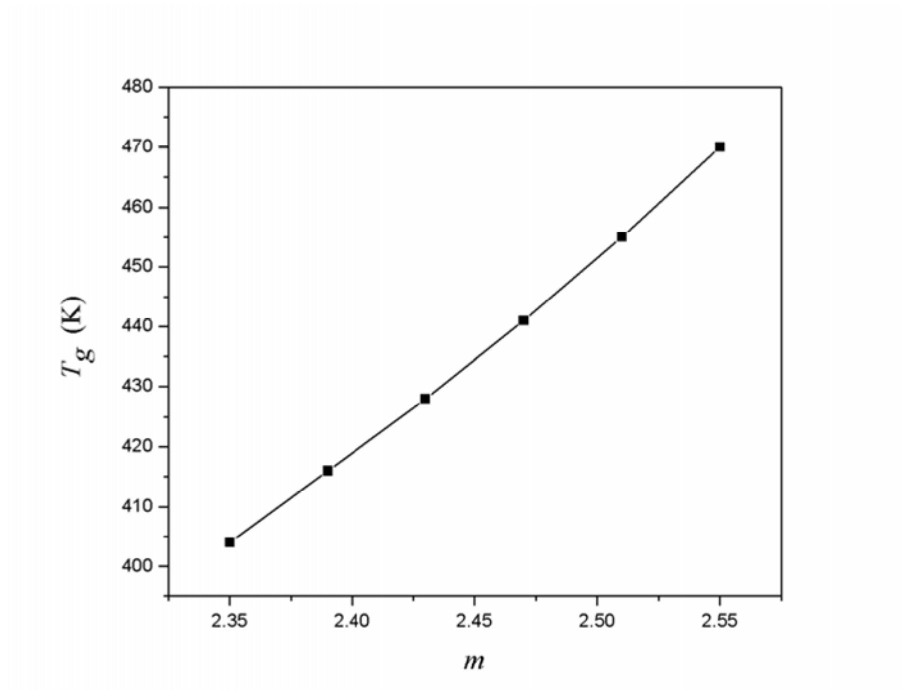

Figure 5.3 T_g variation with m for $Ge_{19-y}Se_{63.8}Sb_{17.2}Te_y$ (y = 0, 2, 4, 6, 8, 10).

For $y = 0$, system is fully crosslinked with the presence of stable heteropolar bonds. *Te* has a strong metallic character in comparison to other chalcogen elements, so when *Te* replaces *Ge* in the ternary glass, new structural units of *Te–Se* bonds are formed. The mean bond energy of the system decreases for R > 1 and makes the system chalcogen rich. Increasing the content of *Te* requires more edge sites for its accommodation leading to the decrease of average cluster size in the glass. Hence, T_g decreases due to weakening of average bond strength on *Te* addition [203].

5.1.2.3 Cohesive energy, heat of atomization, theoretical energy gap, distribution of chemical bonds and electronegativity

Heat of atomization (H_s) is a measure of cohesive energy (*CE*) and has been calculated from equation (4.10). The values of *CE* have been listed in Table 5.2 and found to decrease with the addition of *Te* (Figure 5.4). The theoretical energy gap (E_g^{th}) values have been calculated using equation (4.10) and plotted in Figure 5.4 with increasing *Te* content.

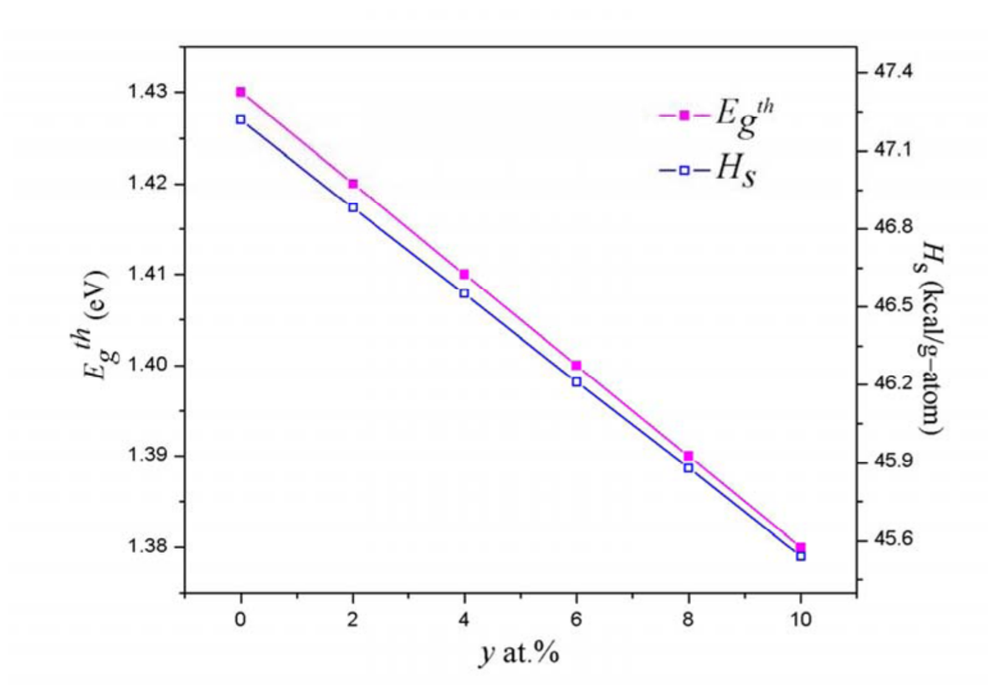

Figure 5.4 Variation of E_g^{th} and H_s with *Te* content for $Ge_{19-y}Se_{63.8}Sb_{17.2}Te_y$ ($y = 0, 2, 4, 6, 8, 10$).

According to chemical bond approach, *Ge–Se* and *Sb–Se* bonds are formed for $y = 0$ (Table 5.2). When *Ge* is replaced with *Te*, the probability of *Ge–Se* bond formation decreases leading to an increase in *Te–Se* bonds along with low energy homopolar bonds. The cohesive energy of the system decreases. The decrease in E_g^{th} is due to the reduction of average stabilization energy on *Te* incorporation [205]. There exists a linear correlation between the average heat of atomization and energy gap [201]. The energy gap strongly depends on the H_s for over constrained material with higher connectivity than for glasses with lower connectivity [201]. There is high connectivity in the system up to $y = 6$, so that E_g^{th} decreases with decreasing values of H_s and *CE*. The values of electronegativity (χ) have been listed in Table 5.2 and found to increase when *Te* is substituted for *Ge*.

Table 5.2 Values of cohesive energy (*CE*), distribution of chemical bonds and electronegativity (χ) for $Ge_{19-y}Se_{63.8}Sb_{17.2}Te_y$ ($y = 0, 2, 4, 6, 8, 10$).

Samples	***CE* (kcal/mol)**	**Distribution of chemical bonds**				χ
		Ge–Se	***Te–Se***	***Sb–Se***	***Se–Se***	
$y = 0$	47.22	0.59561	–	0.40439	–	2.347
$y = 2$	46.88	0.5329	0.03135	0.4044	0.03135	2.350
$y = 4$	46.55	0.4702	0.0627	0.4044	0.0627	2.353
$y = 6$	46.21	0.40752	0.09404	0.4044	0.09404	2.354
$y = 8$	45.21	0.34483	0.1254	0.4044	0.1254	2.356
$y = 10$	45.54	0.28213	0.15674	0.4044	0.15674	2.358

The electronegativity of *Te* is high, therefore, the defect states may increase with increase in electronegativity difference and hence, E_g^{th} decreases. The decrease in E_g^{th} with *Te* addition has been explained on the basis of alloying effect *i.e.* the compositional change of material due to variation in bond angle or bond length, disturbing the order of glass, and thus modifying the structure [206]. *Te* has a tendency to make defect states and create chemical disordering in the system [206]. The number of lone–pair electrons increases with *Te* addition, which indicates that more defects states are formed, increasing disorder in the glasses [206].

5.1.2.4 Density and molar volume

Density (ρ) is related to the change in atomic weight and atomic volume of the elements constituting the system given by equation (4.12) and molar volume (V_m) from equation (4.13). Both the parameters have been found to increase with increasing *Te* content (Table 5.3). Density and mass of the *Te* element is higher than *Ge* due to which ρ increases.

Table 5.3 Values of density (ρ) and molar volume (V_m) for $Ge_{19\text{-}y}Se_{63.8}Sb_{17.2}Te_y$ (y = 0, 2, 4, 6, 8, 10).

Samples	ρ (g/cm^3)	V_m
***y* = 0**	5.22	16.32
***y* = 2**	5.24	16.47
***y* = 4**	5.25	16.62
***y* = 6**	5.27	16.77
***y* = 8**	5.29	16.92
***y* = 10**	5.31	17.07

5.2 Structural properties of *Ge–Se–Sb–Te* chalcogenide glasses

The knowledge of bonding arrangements for $Ge_{19\text{-}y}Se_{63.8}Sb_{17.2}Te_y$ (y = 0, 2, 4, 6, 8, 10) glasses have been obtained from the structural study. In this section, $Ge_{19\text{-}y}Se_{63.8}Sb_{17.2}Te_y$ (y = 0, 2, 4, 6, 8, 10) chalcogenide glasses have been studied for their structure using x–ray diffraction (XRD) and bonding arrangement using Far–IR spectroscopy.

5.2.1 Experimental details

The samples of $Ge_{19\text{-}y}Se_{63.8}Sb_{17.2}Te_y$ (y = 0, 2, 4, 6, 8, 10) have been synthesized using melt quench technique as given in section 4.2.1. The structural nature of samples has been characterized using XRD (X' Pert Pro). Energy dispersive x–ray spectroscopy (EDAX) (Zeiss EVO 40 EP with EDAX attachment operated at 20 kV) has been used for the compositional characterization. The Far–IR absorption measurements have been taken in spectral range 30–350 cm^{-1} at room temperature using FT–IR Spectrometer (Perkin Elmer – Spectrum RX–IFTIR). The details of Far–IR characterization are given in section 4.2.1.

5.2.2 Results and discussion

The analysis of x–ray spectra (Figure 5.5) shows that the sharp peaks are lacking which confirms the amorphous nature of samples. Energy dispersive x–ray spectroscopy results confirm that the presence of *Ge*, *Se*, *Sb*, *Te* elements with the atomic percentages is close to the starting compositions (Table 5.4).

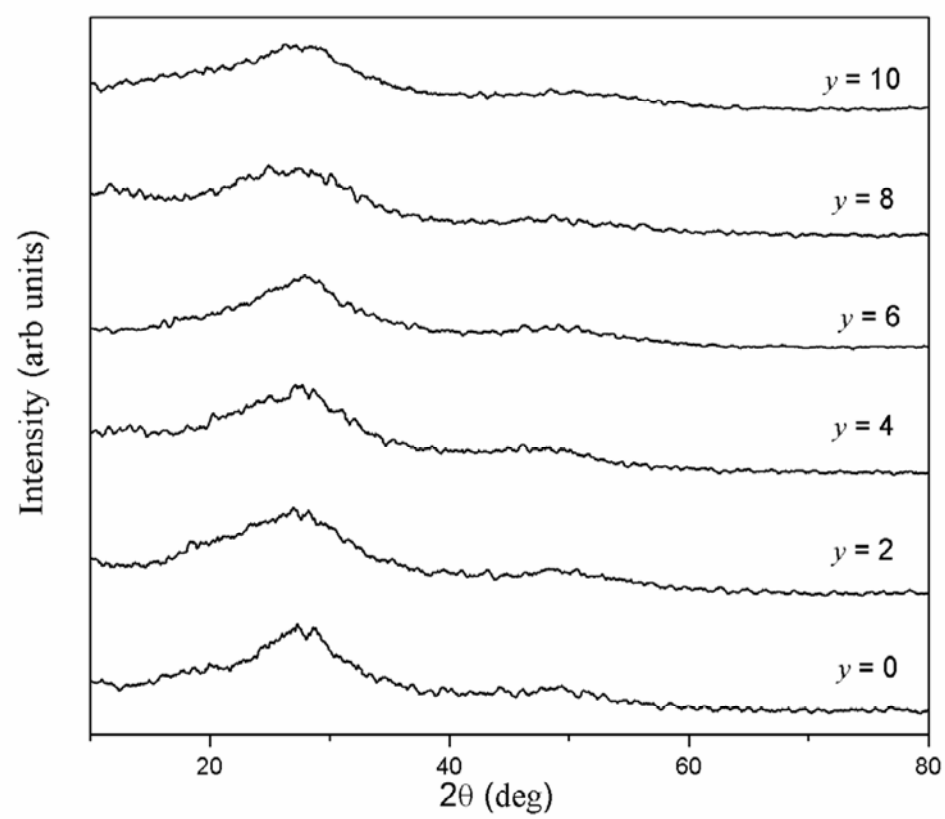

Figure 5.5 XRD spectra of $Ge_{19\text{-}y}Se_{62.8}Sb_{17.2}Te_y$ glasses.

5.2.2.1 Far-IR spectral analysis and theoretical wavenumbers

The relative probability of bonds has been calculated and listed in Table 5.5. Theoretical values of wavenumbers (v), reduced mass (μ) and force constant (K_{AB}) have been calculated from equation (4.14) to equation (4.16) (Table 5.5).

Table 5.4 Elemental composition of $Ge_{19-y}Se_{62.8}Sb_{17.2}Te_y$ (y = 0, 2, 4, 6, 8, 10) bulk glasses.

Samples	*Ge*	*Se*	*Sb*	*Te*
y = 0	19.29	63.73	16.98	–
y = 2	16.88	63.77	17.18	2.17
y = 4	15.33	63.78	17.19	3.7
y = 6	12.92	63.76	17.18	6.14
y = 8	11.28	63.79	17.15	7.78
y = 10	9.12	63.75	17.17	9.96

Table 5.5 Values of bond energy, reduced mass (μ), force constant (K_{AB}), wavenumber (v), relative probability of bond formation at 27 °C and 1000 °C for bonds in $Ge_{19-y}Se_{63.8}Sb_{17.2}Te_y$ (y = 0, 2, 4, 6, 8, 10) alloys.

Bonds	Bond energy (kcal/mol)	μ (10^{-26}Kg U^{1})	K_{AB} (eV)	v (cm^{-1})	Relative probability of bond formation at	
					27 °C	**1000 °C**
Ge–Se	49.42	6.28	1.86	289	1	1
Te–Se	44.18	8.10	1.75	247	1.52×10^{-4}	1.25×10^{-1}
Sb–Se	43.96	7.95	1.54	234	1.05×10^{-4}	1.15×10^{-1}
Se–Se	44.00	6.56	1.91	287	1.13×10^{-4}	1.17×10^{-1}
Ge–Ge	37.00	6.03	1.29	246	2.47×10^{-9}	9.3×10^{-3}
Ge–Te	35.47	7.69	1.28	217	6.95×10^{-11}	4.0×10^{-3}
Ge–Sb	33.76	7.55	1.06	199	3.95×10^{-12}	2.05×10^{-3}
Te–Te	33.00	10.60	1.28	182	1.10×10^{-12}	1.5×10^{-3}
Sb–Te	31.50	10.34	1.05	169	8.93×10^{-14}	8.38×10^{-4}
Sb–Sb	30.22	10.11	0.87	156	1.04×10^{-14}	5.05×10^{-4}

The values of force constant and electronegativity for *Te* are 1.26 and 2.1 respectively. IR spectra of $Ge_{19\text{-}y}Se_{62.8}Sb_{17.2}Te_y$ (y = 0, 2, 4) has been shown in Figure 5.6 and $Ge_{19\text{-}y}Se_{62.8}Sb_{17.2}Te_y$ (y = 6, 8, 10) in Figure 5.7.

When *Te* is substituted for *Ge* in $Ge_{19\text{-}y}Se_{63.8}Sb_{17.2}Te_y$, a new shoulder at 95 cm^{-1} and a peak at 121 cm^{-1} along with a shoulder at 128 cm^{-1}, two shoulders at 140 cm^{-1} and 151 cm^{-1} in the band ranging from 136 cm^{-1} to 236 cm^{-1} have been observed. A well resolved triplet corresponding to 255 cm^{-1}, 267 cm^{-1} and 280 cm^{-1} has been observed in the absorption band extending from 237 cm^{-1} to 320 cm^{-1}. Shoulder at 95 cm^{-1} indicates E mode of trigonal *Te* which is strongly infrared active [174]. For y = 4, there is an appearance of well resolved triplet that includes 88 cm^{-1}, 98 cm^{-1} and 106 cm^{-1}. Absorption peak at 88 cm^{-1} has been assigned as transverse optical mode (TO) of $GeSe_2$ crystal mode [175]. Peak at 98 cm^{-1} is in accordance with earlier reported result [171, 174, 175]. Peak at 106 cm^{-1} may be designated as $GeSe_4$ (ν_4 mode) and $SbSe_3$ pyramidal unit. Shoulder becomes a weak absorption peak for y = 6 and shifts little towards higher wavenumber, but for y = 8, triplet again shows its existence and does not appears for y = 10. Shoulder at 140 cm^{-1} has been observed for y = 2, 6, 8, 10 but for y = 4 it becomes an absorption peak and indicates *Se* polymeric chain (E mode) [175]. Sharp absorption peak at 121 cm^{-1} and its shoulder at 128 cm^{-1} has been observed up to y = 4. For y = 6 and 8, peak diminishes and shoulder appears to be a weak peak.

For 10 at.% of *Te*, peak shifts toward lower wavenumber and appears at 121 cm^{-1}. Peak at 121 cm^{-1} indicates $GeSe_2$ (Raman mode) and at 128 cm^{-1} peak may be assigned as ν_1 (A_1) mode of $GeTe_4$ tetrahedron [207]. Absorption peak at 128 cm^{-1} is in good agreement with the results obtained by Andrikopoulos *et al.* [207]. With addition of *Te* (y = 2), absorption shifts little towards lower wavenumber (Figure 5.6). This shows that when *Ge* is substituted with *Te*, bonds with low energy have been formed. This has been confirmed from the physical study as discussed in section 5.1.2.3. Shoulder at 151 cm^{-1} indicates symmetric stretching vibration of *Te–Te* bonds [207, 208]. For 4 at.% addition of *Te*, shoulder shifts towards higher wavenumber side and again moves back for $y \geq 6$. The *Te–Te* bonds occur at 150 cm^{-1} for *a–Te* while for *c-Te* at about 123 cm^{-1}. Depending on the degree of disorder, *Te–Te* bonds occur towards higher wavenumber [207].

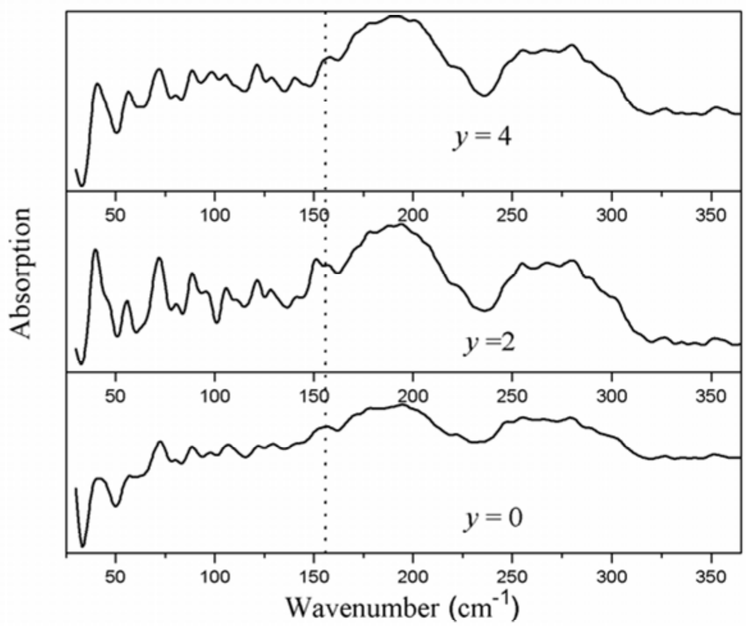

Figure 5.6 Far–IR absorption spectra of $Ge_{19\text{-}y}Se_{63.8}Sb_{17.2}Te_y$ (y = 0, 2, 4) glasses. The ordinate scale for different x–values is shifted for clarity.

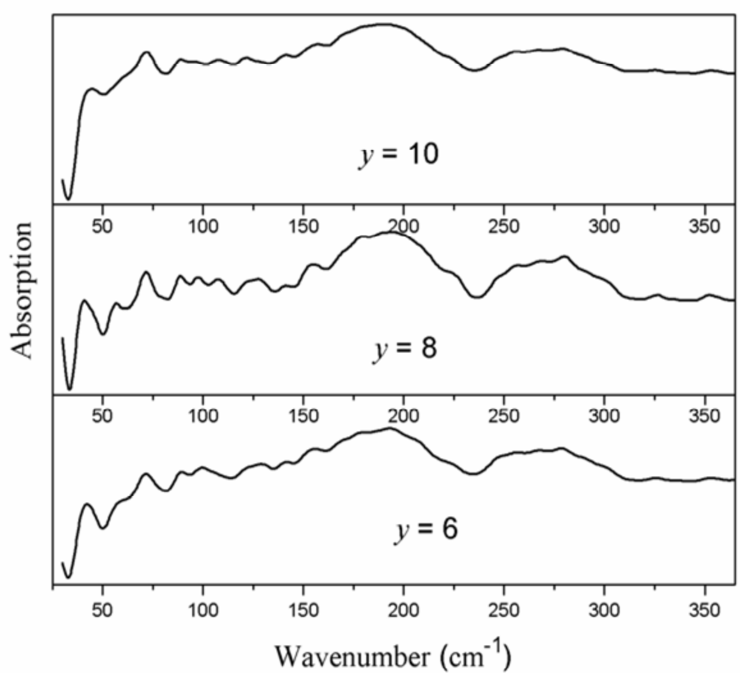

Figure 5.7 Far–IR absorption spectra of $Ge_{19\text{-}y}Se_{63.8}Sb_{17.2}Te_y$ (y = 6, 8, 10) glasses. The ordinate scale for different x–values is shifted for clarity.

Triplet in band ranging from 237 cm^{-1} to 320 cm^{-1} gets weak for $y \geq 4$, but for $y = 4$ and 8, feature at 280 cm^{-1} becomes sharp. This triplet may be assigned as pyramidal $SbSe_3$ [172], F_2–mode of $GeSe_{4/2}$ tetrahedron [176], $GeSe_2$ (Raman mode) and ν_3 mode of $GeSe_4$ [175].

Other absorption peaks such as 40 cm^{-1}, 72 cm^{-1} remain at the same position. The intensity of the peak at 40 cm^{-1} increases for y = 2, 4, 6, 8. For y = 10 the absorption peak gets broaden and comparatively weak. Absorption peak at 72 cm^{-1} may be attributed to the bending mode of $GeTe_2$ structural unit [152], $GeSe_4$ (ν_2 mode) and $SbSe_3$ pyramidal unit. Band in the range of 135–236 cm^{-1} remains at the same position for y = 2, 6, 8, 10. At y = 4, band becomes narrower in the range of 148 cm^{-1} to 236 cm^{-1}. The weak features may show the presence of symmetric stretch ν_1 (A_1) vibrational modes for $GeTe_2$ [152], $Se_{8-x}Te_x$ mixed rings [176], vibrations of Se–Te bonds [209], $Se_{8-x}Te_x$ rings and probably as Se_6Te_2 rings [210].

5.3 Thermal properties of *Ge–Se–Sb–Te* chalcogenide glasses

In chalcogenide glasses, it is important to understand the glass transition kinetics for the knowledge of thermal stability and glass forming ability. This is useful for the specific technological applications. The differential thermal analysis (DTA) has been performed on $Ge_{19-y}Se_{63.8}Sb_{17.2}Te_y$ system to study the glass transition temperature (T_g), crystallization temperature (T_c) and melting temperature (T_m), thermal stability and ease of glass formation at different heating rates (γ = 5, 10, 15, 20 K/min). The dependence of T_g on the heating rate has been investigated. The activation energy for glass transition and crystallization has been calculated using various methods [12–17]. For DTA study, non–isothermal method has been used due to its applicability on a wide range of temperature and quick analysis in shorter time period [18].

5.3.1 Experimental details

The powdered samples have been used to study the thermal properties of $Ge_{19-y}Se_{63.8}Sb_{17.2}Te_y$ (y = 0, 2, 4, 6, 8, 10) system. The detailed procedure for sample synthesis is given in section 4.1.1. DTA scans have been taken using differential thermal analysis (DTA) (EXSTAR TG/DTA 6300) at different heating rates, 5, 10, 15 and 20 K/min. All the measurements have been made under non–isothermal conditions.

5.3.2 Results and discussion

5.3.2.1 Glass transition temperature, crystallization temperature and melting temperature

DTA thermograms for $Ge_{19-y}Se_{63.8}Sb_{17.2}Te_y$ (y = 0, 2, 4, 6, 8, 10) alloys recorded at the heating rate of 5, 10, 15, 20 K/min have been shown in Figure 5.8 to Figure 5.13. The characteristic features of these curves are glass transition temperature (T_g), crystallization temperature (T_c) and melting temperature (T_m). The curves indicate an endothermic step at glass transition temperature and second peak is exothermic that takes place due to phase change. At this temperature, the amorphous material begins to crystallize and is called crystallization temperature. The third peak is again endothermic peak which occurs due to absorption of heat and the sample begins to melt. This peak is represented as melting temperature.

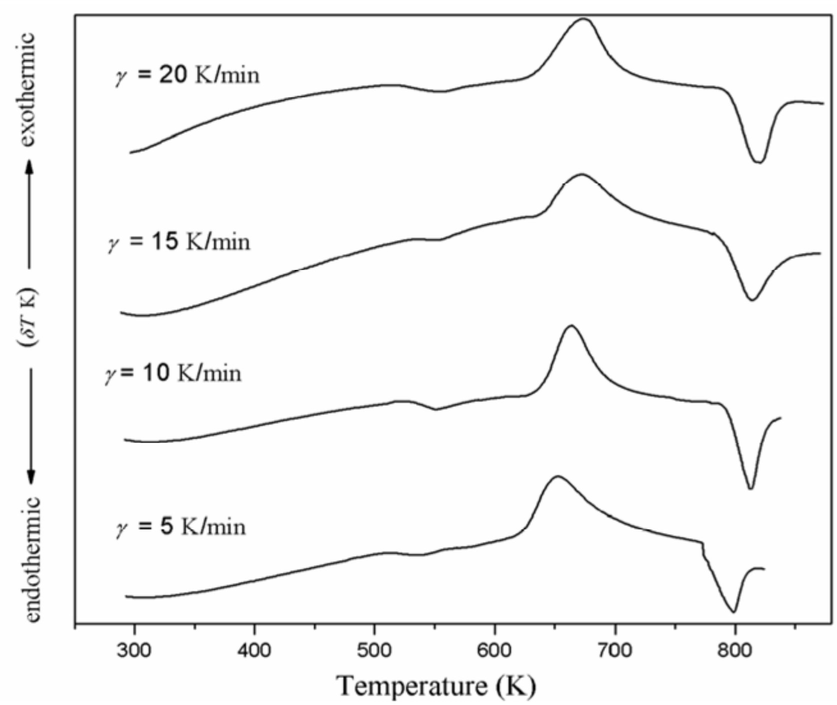

Figure 5.8 DTA trace for $Ge_{19}Se_{63.8}Sb_{17.2}$ alloys at heating rate of 5, 10, 15 and 20 K/min.

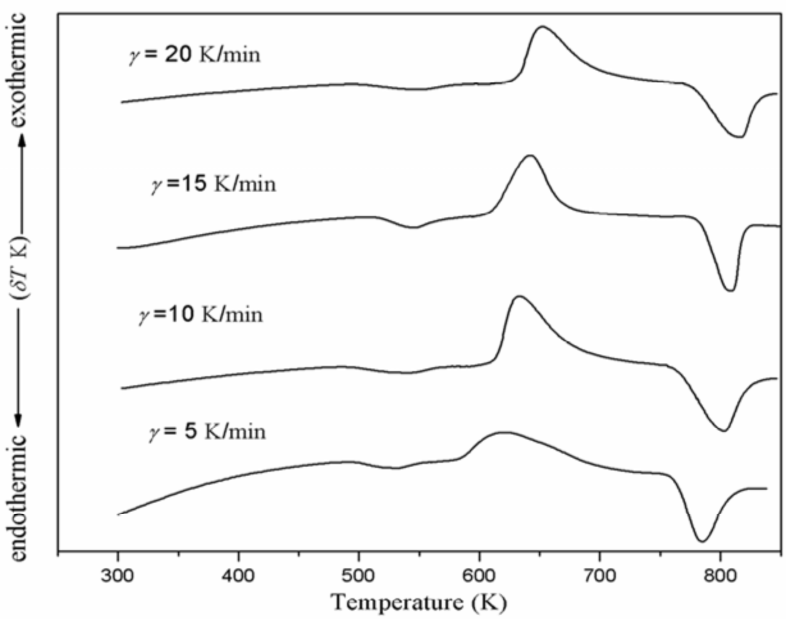

Figure 5.9 DTA thermograms for $Ge_{17}Se_{63.8}Sb_{17.2}Te_2$ alloys at heating rate of 5, 10, 15 and 20 K/min.

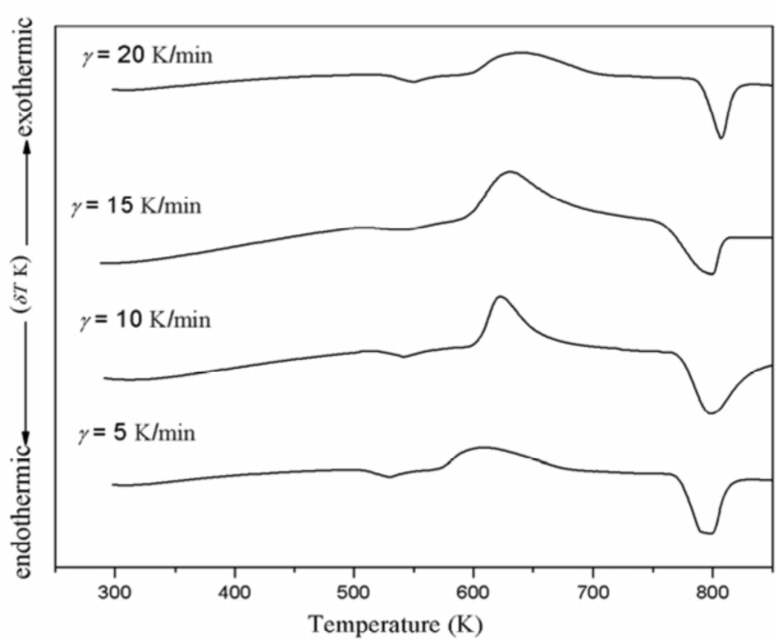

Figure 5.10 DTA trace for $Ge_{15}Se_{63.8}Sb_{17.2}Te_4$ alloys at heating rate of 5, 10, 15 and 20 K/min.

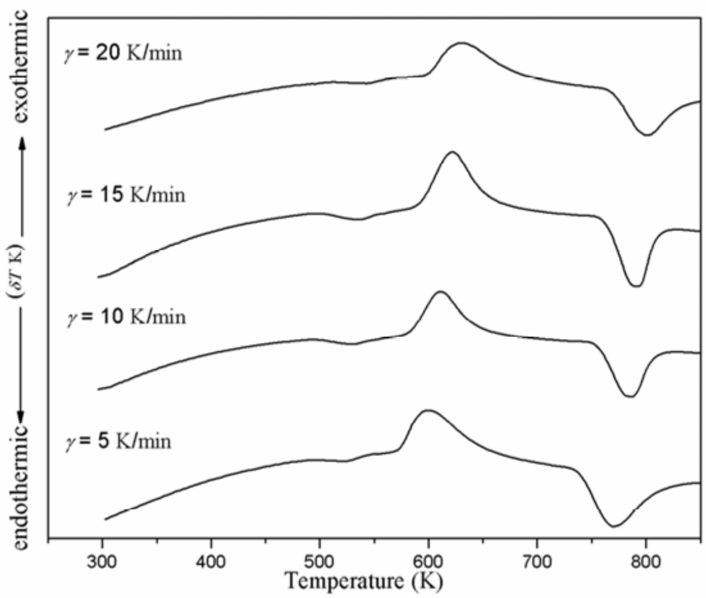

Figure 5.11 DTA thermograms for $Ge_{13}Se_{63.8}Sb_{17.2}Te_6$ alloys at heating rate of 5, 10, 15 and 20 K/min.

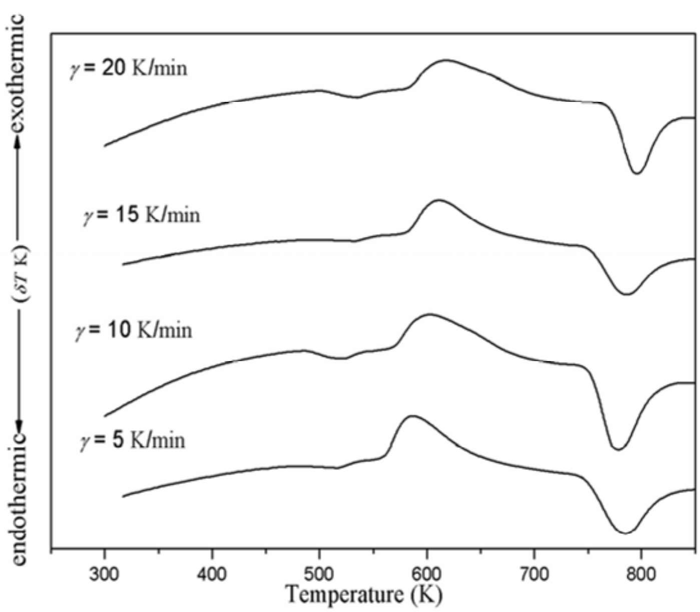

Figure 5.12 DTA thermograms for $Ge_{11}Se_{63.8}Sb_{17.2}Te_8$ alloys at heating rate of 5, 10, 15 and 20 K/min.

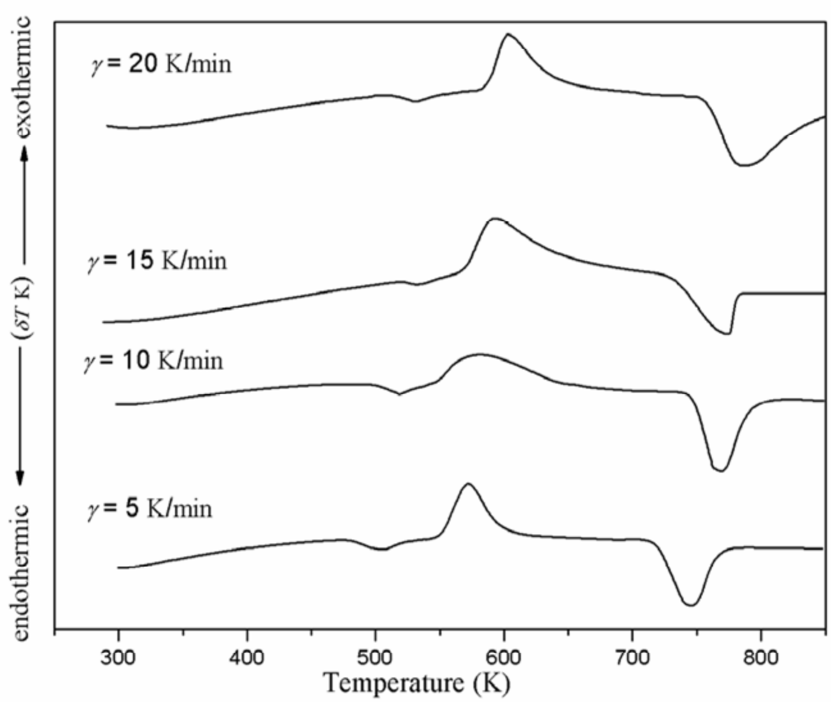

Figure 5.13 DTA trace for $Ge_9Se_{63.8}Sb_{17.2}Te_{10}$ alloys at heating rate of 5, 10, 15 and 20 K/min.

These three temperatures increase with increasing heating rate due to high flow of heat through the sample. The values of T_g, T_c and T_m have been evaluated from Figure 5.8 to 5.13 are given in Table 5.6. These values (Table 5.6) have been found to decrease with increasing content of *Te*. The values of T_g are in accordance with the values obtained from physical study of these glasses as discussed in section 5.1.2.2 (Figure 5.3).

5.3.2.2 Glass forming ability and reduced glass transition temperature

Thermal stability is an important parameter for the analysis of glasses. Two criteria have been used to measure the thermal stability of glasses.

First criterion is the difference between T_g and T_c [211]. Second criterion is Hruby parameter (equation (4.17)) that gives the glass forming ability (K_{gl}) [183].

Table 5.6 Values of glass transition temperature (T_g), crystallization temperature (T_c) and melting temperature (T_m) for $Ge_{19-y}Se_{63.8}Sb_{17.2}Te_y$ (y = 0, 2, 4, 6, 8, 10) glassy alloys at different heating rates γ.

Samples	γ (K/min)	T_g (K)	T_c (K)	T_m (K)
***y* = 0**	5	537.00	649.00	798.00
	10	546.00	663.72	812.00
	15	551.81	672.25	815.00
	20	555.44	679.18	821.00
***y* = 2**	5	532.00	620.00	785.00
	10	542.00	633.00	803.00
	15	547.00	643.00	810.00
	20	552.27	652.00	817.00
***y* = 4**	5	527.00	609.00	779.00
	10	536.00	622.00	796.00
	15	542.35	631.00	800.00
	20	547.00	640.00	807.00
***y* = 6**	5	522.00	592.00	769.00
	10	530.00	612.00	787.00
	15	536.59	621.00	793.00
	20	542.67	629.00	800.00
***y* = 8**	5	514.00	585.00	758.00
	10	522.00	602.00	778.00
	15	529.70	610.00	787.00
	20	534.00	617.00	796.00
***y* = 10**	5	506.00	571.29	746.00
	10	516.71	582.18	768.94
	15	521.00	592.94	775.78
	20	527.00	602.69	784.00

Kauzmann proposed the reduced glass transition temperature (T_{rg}) which is based on the theoretical relation between T_g and T_m and has been calculated using equation (4.18) [184]. According to the rule, T_{rg} should be constant nearly equal to 2/3 for glasses and is also called as two–third rule [184]. It has been observed that the obtained values obey the two–third rule (Table 5.7) indicating the ease of glass formation.

The larger difference between T_c and T_g indicate that the kinetic resistance towards the crystallization is higher or *vice−versa*. If glasses show the crystallization peak near the glass transition temperature then they are considered as unstable glasses while glasses having peak near the melting temperature are regarded as stable glasses. The difference between T_c and T_g decreases with the addition *Te* content indicating that the K_{gl} parameter decreases. Therefore, there is decrease in thermal stability and hence, the glass forming ability also decreases.

The heating rate dependence of the glass transition temperature has been interpreted using empirical relation given in equation (4.19). A plot between ln (γ) and T_g (Figure 5.14) has been used to obtain the values of A' and B'. The decrease in A' indicates that the glass transition temperature decreases with the increasing content of *Te*. The value of B' depends upon the cooling rate during the preparation of samples [212].

Table 5.7 The characteristic parameters K_{gl} and T_{rg} at γ = 10 K/min. Values of A' and B' for $Ge_{19-y}Se_{63.8}Sb_{17.2}Te_y$ (y = 0, 2, 4, 6, 8, 10) glassy alloys.

Samples	K_{gl}	T_{rg}	A'	B'
y = 0	0.794	0.672	515.40	13.38
y = 2	0.544	0.674	510.63	13.74
y = 4	0.489	0.674	504.94	14.05
y = 6	0.468	0.674	499.20	13.97
y = 8	0.450	0.671	490.41	14.32
y = 10	0.351	0.672	482.50	14.64

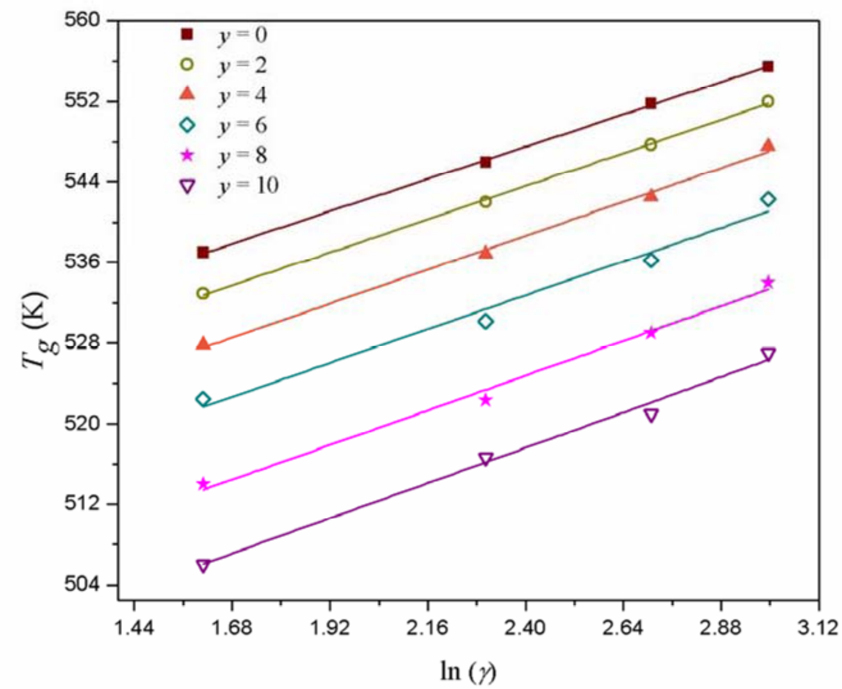

Figure 5.14 Plot of T_g *vs.* ln (γ) for $Ge_{19-y}Se_{63.8}Sb_{17.2}Te_y$ glasses.

5.3.2.3 Activation energy of glass transition temperature and crystallization temperature

The activation energy of glass transition temperature (E_g) has been analyzed using Moynihan [124] and Kissinger [127] approaches using equations (2.1) and (2.3). Plot of ln (γ) *vs* 1000/T_g for Moynihan approach [124] has been used to determine the values of activation energy of glass transition temperature (Figure 5.15). Plot of ln (α/T_g^2) against 1000/T_g in Kissinger method [127] yields a straight line and slope gives the value of activation energy of glass transition temperature (Figure 5.16). The calculated values of E_g have been found to decrease with addition of *Te* content (Table 5.8). The values obtained from two methods are in good agreement with each other. In glass transition region, the metastable states are separated by energy barriers. Atoms in these states try to attain stability by crossing the energy barriers. Energy needed to cross these energy barriers is known as activation energy of glass transition. Glass with minimum activation energy has more tendency to cross the energy barrier and hence, becomes stable. With the addition of *Te* content, E_g decreases and atoms of glasses have more probability to jump these metastable states.

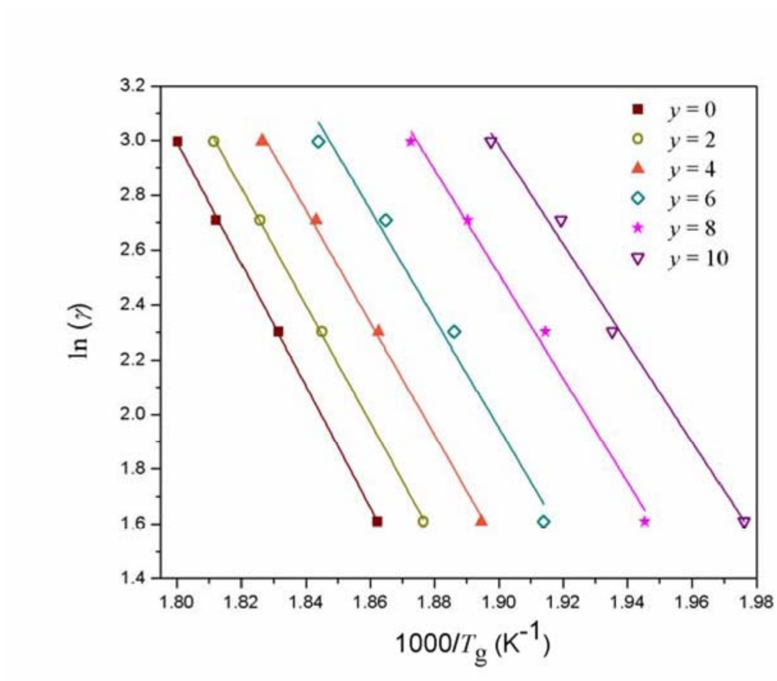

Figure 5.15 Variation of ln (γ) *vs.* 1000/T_g for $Ge_{19-y}Se_{63.8}Sb_{17.2}Te_y$ alloys.

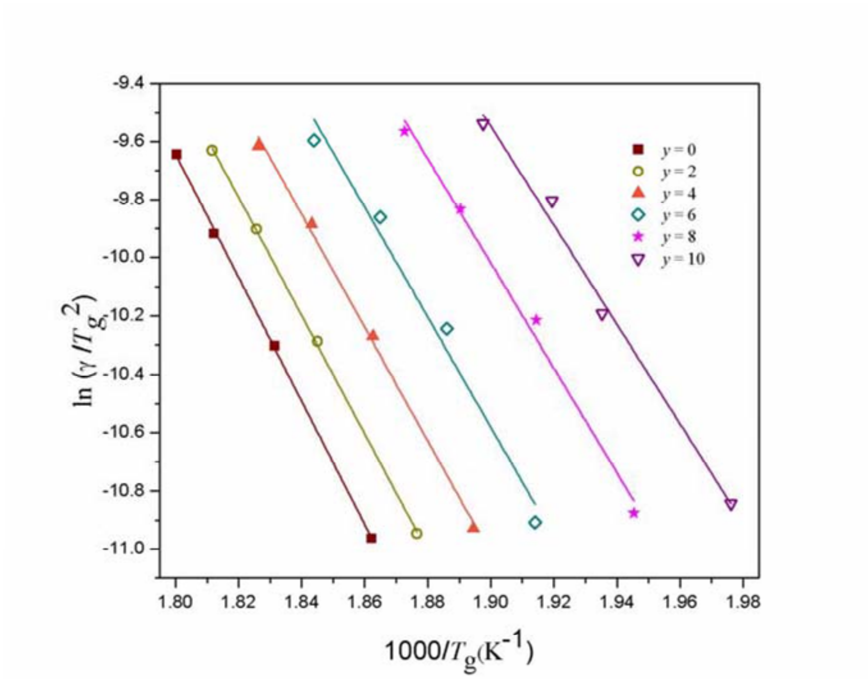

Figure 5.16 Plot of ln (γ/T_g^2) *vs.* 1000/T_g for $Ge_{19-y}Se_{63.8}Sb_{17.2}Te_y$ glasses.

Table 5.8 Values of activation energy for glass transition temperature (E_g) and activation energy for crystallization temperature (E_c) for $Ge_{19\text{-}y}Se_{63.8}Sb_{17.2}Te_y$ (y = 0, 2, 4, 6, 8, 10) glassy alloys.

y	E_g kJmol^{-1} [Moynihan method]	E_g kJmol^{-1} [Kissinger method]	E_c kJmol^{-1} [Augis and Bennett method]	E_c kJmol^{-1} [Mahadevan method]
0	185.29	176.22	169.31	163.82
2	177.88	168.81	150.23	144.93
4	170.56	161.57	144.61	139.44
6	165.57	156.67	138.03	132.87
8	158.08	149.43	131.04	126.05
10	150.09	141.52	125.38	120.47

The activation energy for crystallization temperature (E_c) has been determined using Mahdevan (equation (2.4)) and Augis and Bennett approaches (equation (2.5)) [128, 129]. Plot between ln(γ) versus 1000/T_c in Mahadevan's approach has been found to be straight lines and hence, the values of activation energy have been calculated from their slopes (Figure 5.17).

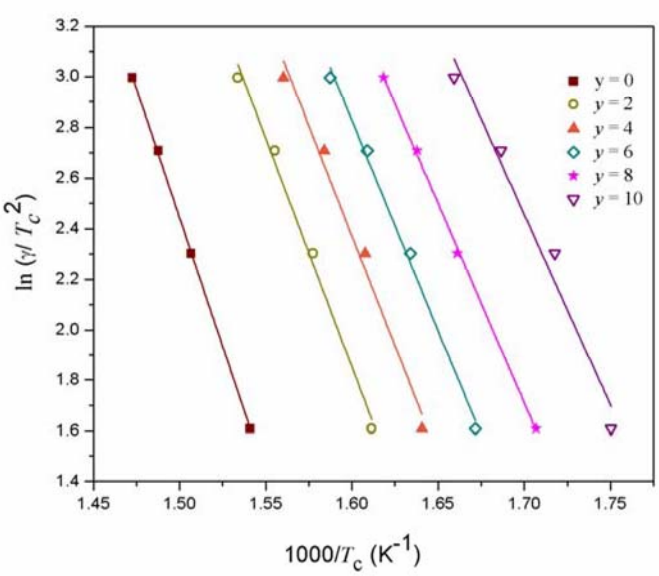

Figure 5.17 Plot of ln (γ) *vs.* 1000/T_c for $Ge_{19\text{-}y}Se_{63.8}Sb_{17.2}Te_y$ glassy alloys.

The slope of straight line using Augis and Bennett method in Figure 5.18 gives the value of E_c. The values of activation energy for crystallization from both the methods are in good agreement. The activation energy for crystallization during phase transformation decreases with increasing content of *Te* (Table 5.8) and has been explained on the basis of cohesive energy. The cohesive energy of the system decreases with *Te* content (Table 5.2). The decrease in E_c may be related to nucleation and growth process in which devitrification requires less energy due to decreasing value of *CE*. This shows that the probability of the system towards devitrification increases as the *Te* concentration increases in *Ge–Se–Sb–Te* quaternary glasses.

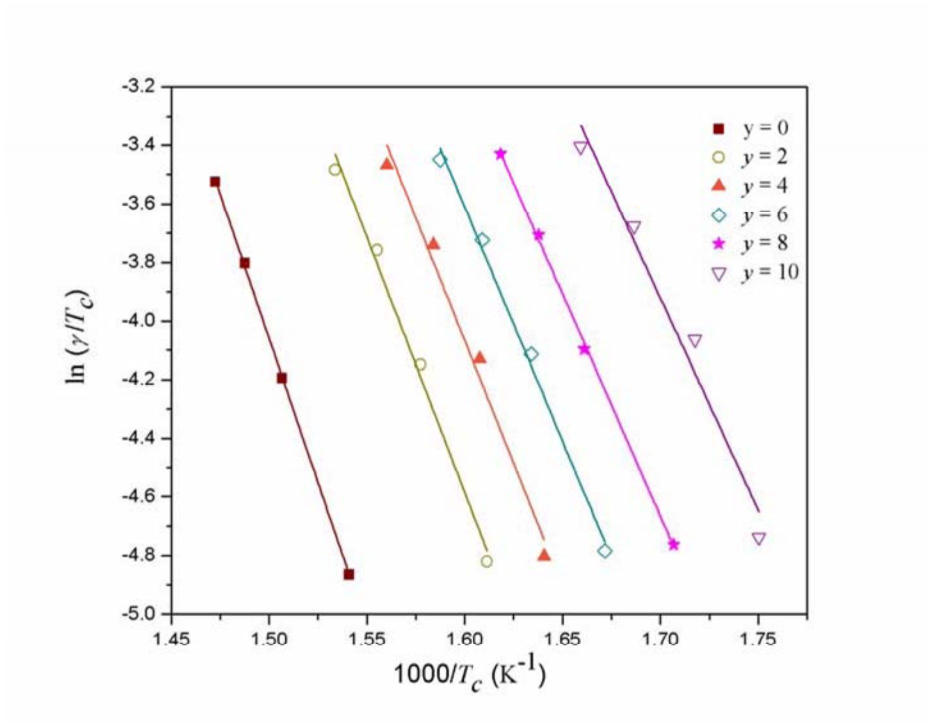

Figure 5.18 Variation of ln (γ/T_c) *vs.* 1000/T_c for $Ge_{19-y}Se_{63.8}Sb_{17.2}Te_y$ alloys.

5.4 Optical properties of *Ge–Se–Sb–Te* thin films

In this section, optical parameters of $Ge_{19}Se_{81-x}Sb_x$ (x = 0, 4, 8, 12, 16, 17.2, 20) thin films have been determined using UV–Vis–NIR spectroscopy. The parameters *viz.* refractive index, extinction coefficient, optical band gap, dispersion parameters, optical conductivity and non–linear refractive index have been evaluated.

5.4.1 Experimental details

Thin films of $Ge_{19-y}Se_{63.8}Sb_{17.2}Te_y$ (y = 0, 2, 4, 6, 8, 10) have been deposited using thermal evaporation technique. The details of film deposition are mentioned in section 4.4.1. The transmission spectra of these thin films have been obtained using a double beam UV–Vis–NIR spectrophotometer (Perkin Elmer Lambda – 750). The slit width has been kept at 1 nm and all the measurements have been performed at room temperature (300K).

5.4.2 Results and discussion

5.4.2.1 Refractive index, absorption coefficient and optical band gap

Transmission spectra of $Ge_{19-y}Se_{63.8}Sb_{17.2}Te_y$ (y = 0, 2, 4, 6, 8, 10) thin films shows that the transmission shifts towards longer wavelength with *Te* addition to the ternary system (Figure 5.19). A red shift has been observed in interference free region of spectra shown in Figure 5.20.

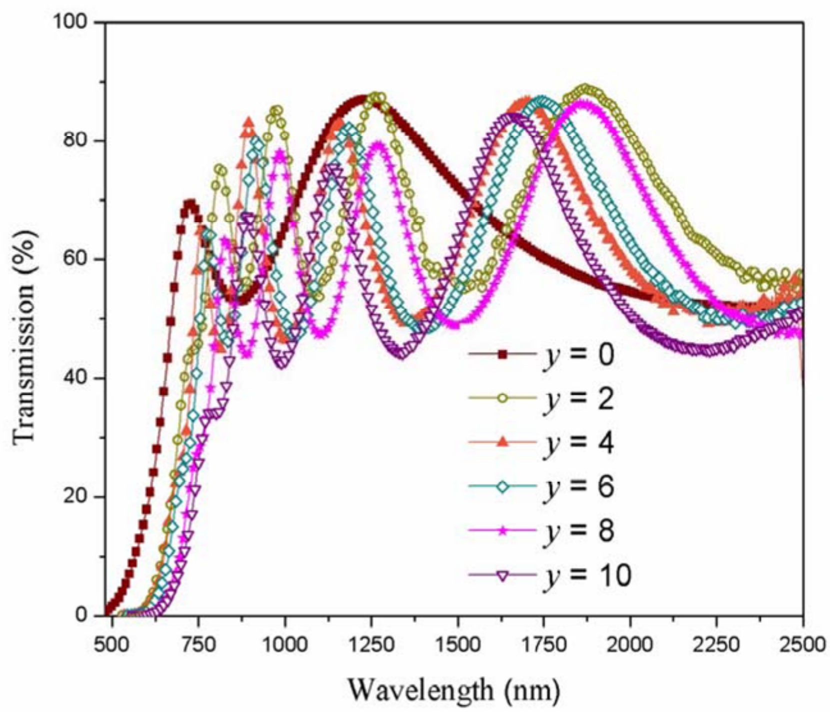

Figure 5.19 Transmission spectra for $Ge_{19-y}Se_{63.8}Sb_{17.2}Te_y$ (y = 0, 2, 4, 6, 8, 10) thin films.

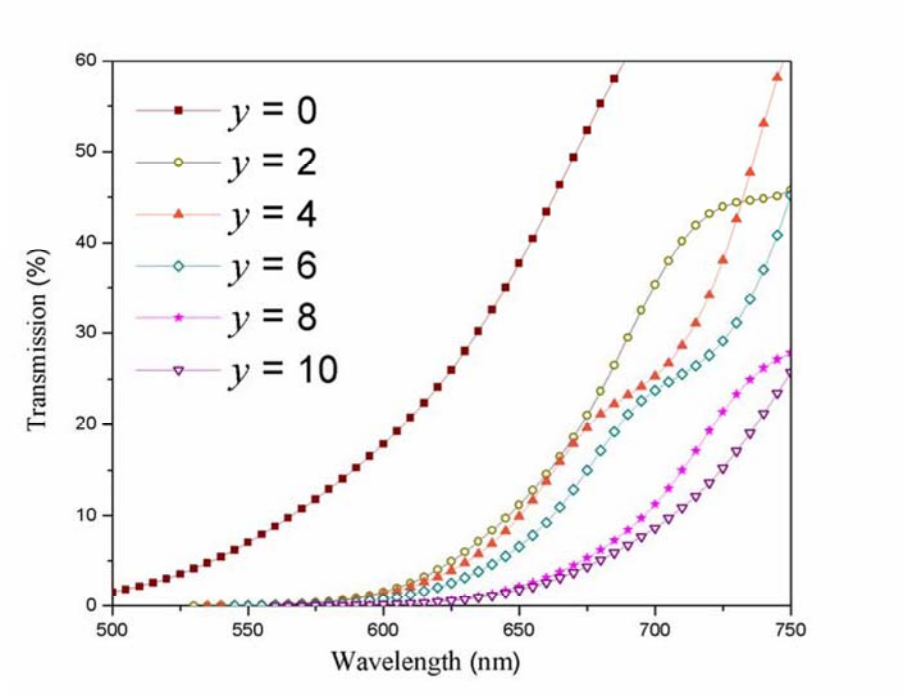

Figure 5.20 Transmission spectra showing a red shift for $Ge_{19-y}Se_{63.8}Sb_{17.2}Te_y$ (y = 0, 2, 4, 6, 8, 10) thin films.

The thickness of the films has been calculated using equation (4.20) (Table 5.9). Refractive index (n) and extinction coefficient (k) have been evaluated using envelope method employing equation (2.9) and equation (2.11) respectively [137,138].

Table 5.9 Values of thickness (t_{correc}) and optical band gap (E_g^{opt}) for $Ge_{19-y}Se_{63.8}Sb_{17.2}Te_y$ thin films.

Samples	t_{correc} (nm)	E_g^{opt} (eV)
***y* = 0**	227	1.57
***y* = 2**	662	1.55
***y* = 4**	593	1.52
***y* = 6**	596	1.51
***y* = 8**	617	1.46
***y* = 10**	538	1.42

Refractive index shows normal dispersion behavior and increases with increasing content of *Te* (Figure 5.21). The extinction coefficient also increases with *Te* concentration (Figure 5.22). The increase in refractive index has been explained using polarizability of atoms. The replacement of *Ge* (being less polarizable having atomic radius 1.22 Å) with *Te* (highly polarizable having 1.37 Å atomic radius) leads to an increase in refractive index of the system [213]. Increase in the value of *k* with addition of *Te* content indicates that loss of light increases due to scattering. A red shift evident from the Kramers–Kronig relation also supports the increased refractive index [188].

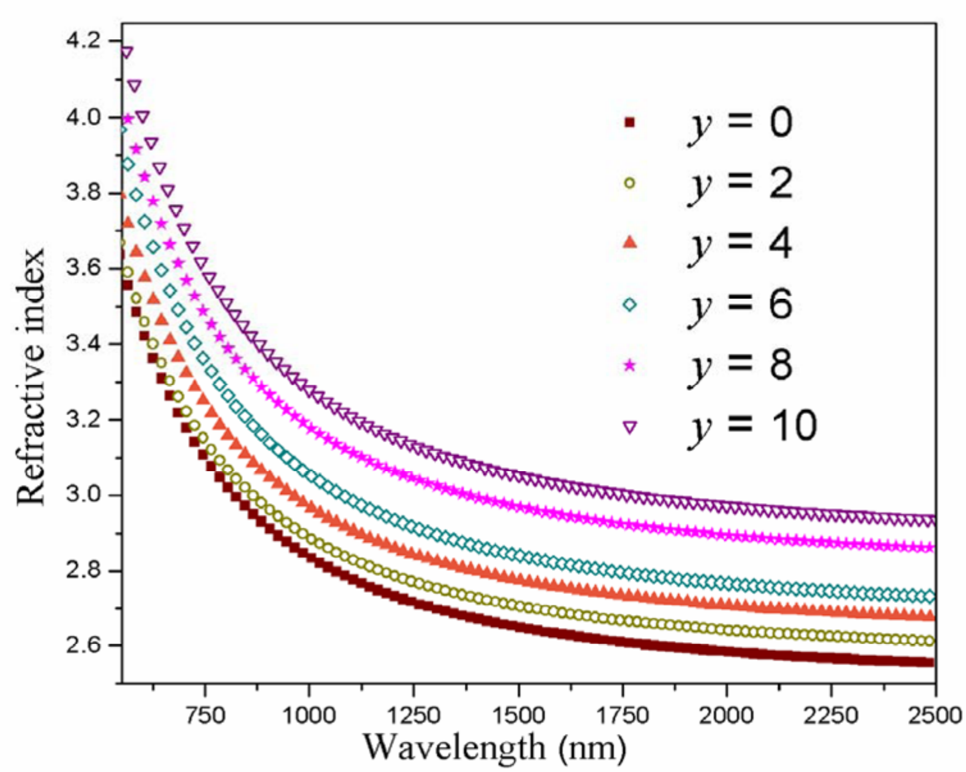

Figure 5.21 Variation of refractive index with wavelength for $Ge_{19-y}Se_{63.8}Sb_{17.2}Te_y$ system.

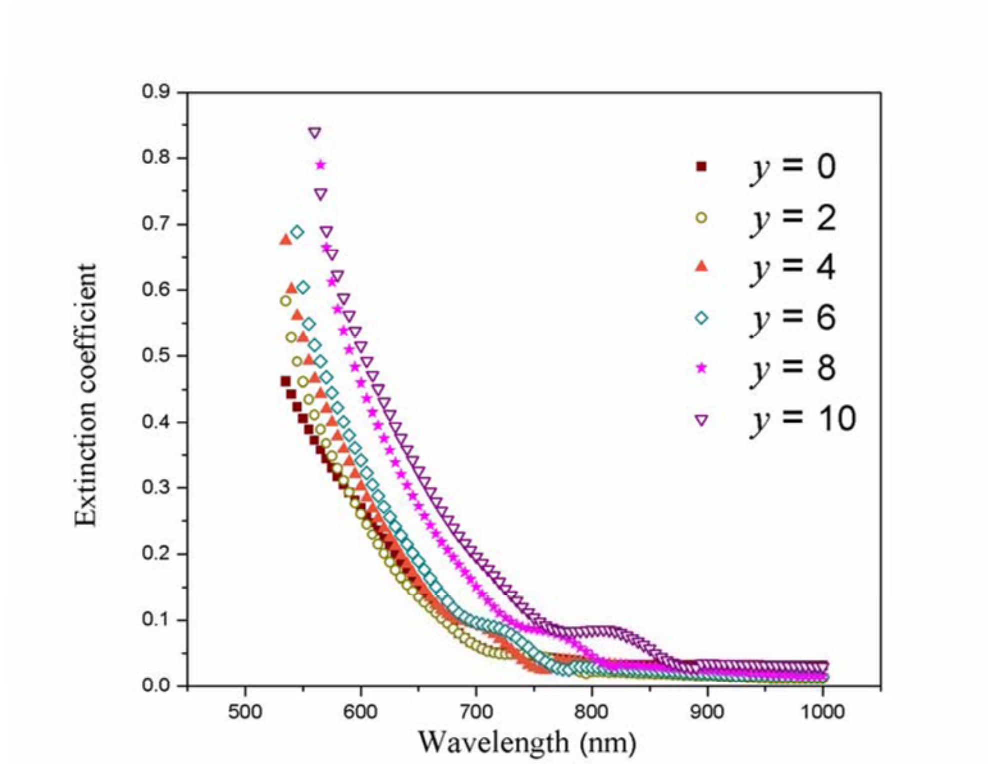

Figure 5.22 Variation of extinction coefficient with wavelength for $Ge_{19-y}Se_{63.8}Sb_{17.2}Te_y$ glasses.

The absorption coefficient (α) of thin films has been calculated using equation (2.13). The value of α increases with increasing energy and *Te* content (Figure 5.23). The E_g^{opt} has been calculated using equation (2.17). The relation $(\alpha h\nu)^{0.5} = f(h\nu)$ plotted in Figure 5.24 shows the non–linear nature for all quaternary compositions indicating indirect allowed transition [143]. E_g^{opt} has been found to decrease with increasing *Te* content (Table 5.9).

When *Ge* is replaced with *Te*, *Ge–Te* and *Te–Te* bonds appear along with some former bonds such as *Ge–Se*, *Sb–Se* and *Se–Se* (section 5.2.2.1). The bond energy of *Ge–Te* and *Te–Te* bonds is low in comparison to other bonds. Due to this low bond energy, the overall energy of the system decreases that lead the optical band gap to decrease (Table 5.2) with addition of *Te* to the $Ge_{19}Se_{63.8}Sb_{17.2}$ system.

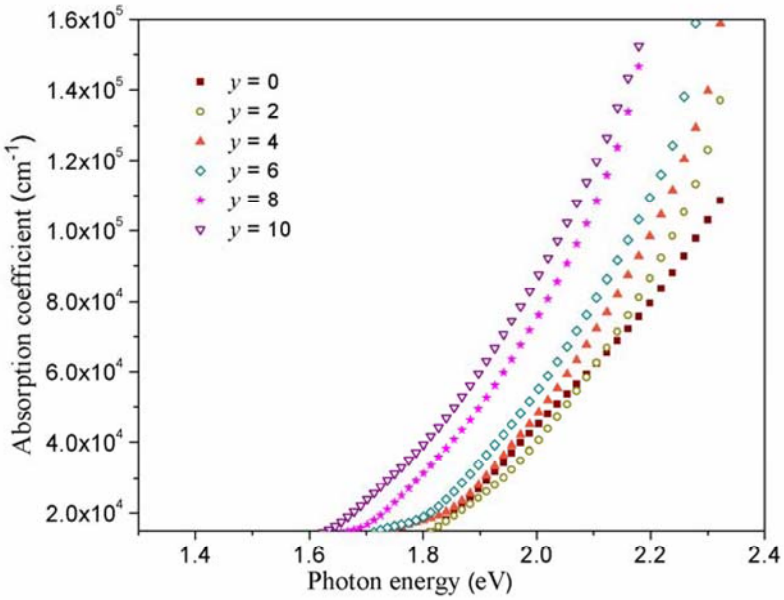

Figure 5.23 Variation of absorption coefficient with photon energy for $Ge_{19\text{-}y}Se_{63.8}Sb_{17.2}Te_y$ glasses.

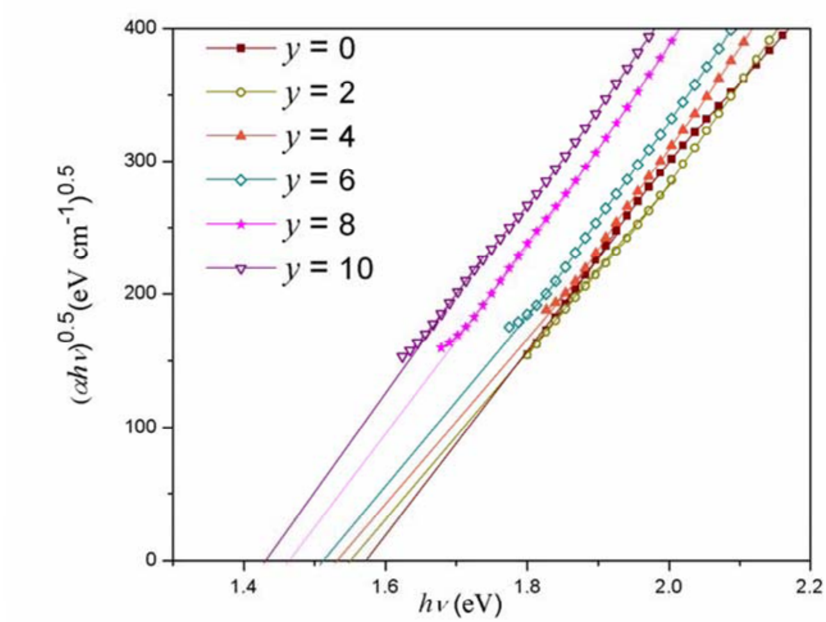

Figure 5.24 Variation of $(\alpha h\nu)^{0.5}$ with photon energy ($h\nu$) for $Ge_{19\text{-}y}Se_{63.8}Sb_{17.2}Te_y$ (y = 0, 2, 4, 6, 8, 10) thin films.

5.4.2.2 Dispersion parameters and optical conductivity

The dispersion of refractive index has been analyzed in terms of Wemple Di−Domineco single−effective−oscillator (WDD) model given in equation (2.19) [145−146]. Oscillator parameters (E_o, E_d) calculated from the linear fit of $(n^2\text{-}1)^{-1}$ and $(h\nu)^2$ (Figure 5.25) are given in Table 5.10. The values of static refractive index (n_o) (Table 5.10) have been determined by extrapolating the WDD dispersion equation for $h\nu \rightarrow 0$.

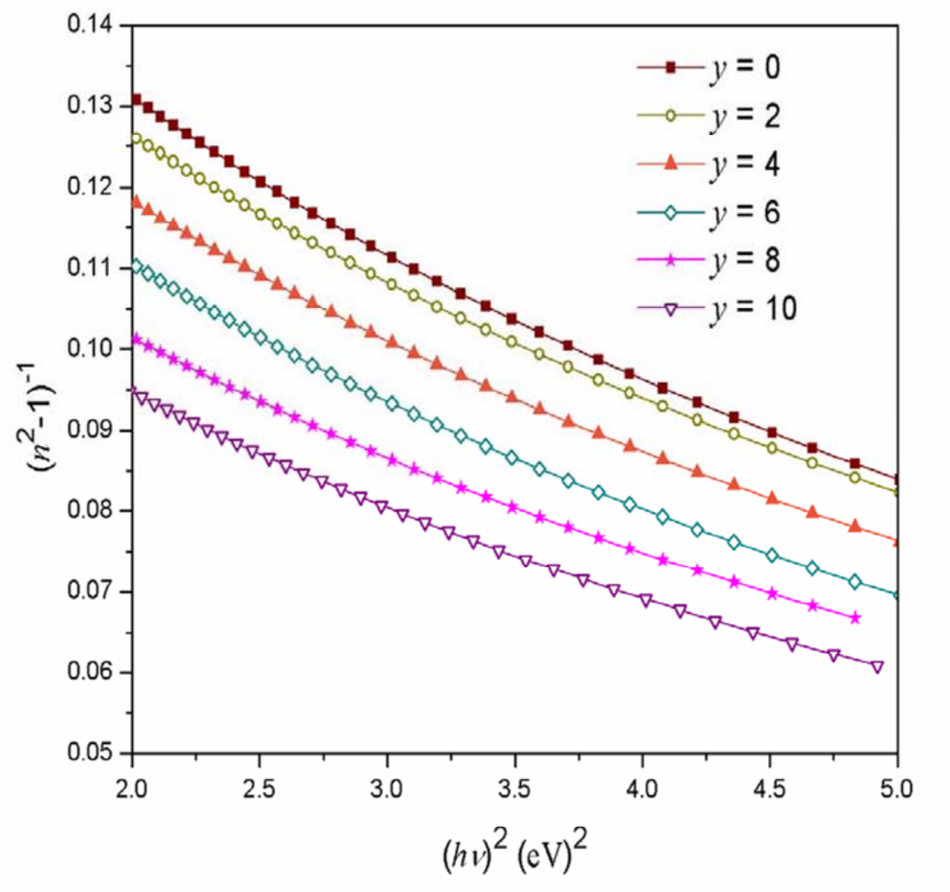

Figure 5.25 Plot of $(n^2\text{-}1)^{-1}$ with $(h\nu)^2$ for $Ge_{19\text{-}y}Se_{63.8}Sb_{17.2}Te_y$ (y = 0, 2, 4, 6, 8, 10) thin films.

Average energy gap E_o is related to the bond energy of chemical bonds present in system. The bond energy of the system decreases and hence, values of oscillator energy (E_o) have been found to decrease. Average energy gap is related to Tauc gap by Tanaka's relation $E_o \approx 2 \times E_g^{opt}$ [192]. The values obtained by Tanaka's relation are in agreement with those obtained from Tauc's relation (Table 5.9). The number of states in the conduction band depends upon the number of bonds and in the valence band due to the presence of lone−pair electrons [206]. From the physical study, it has been observed that lone−pair electrons increase with the increasing *Te* content. These lone−pair electrons increase the density of defects states so that there is an overlapping of mobility edges in the forbidden gap due to which E_g^{opt} decreases. The decrease in E_g^{opt} has also been explained on the basis of distribution of bonds. From Table 5.2, it has been found that the low energy *Te−Se* bonds replace the high energy *Ge−Se* bonds, due to which the bond energy of the system decreases on *Te* addition and hence, optical band gap decreases.

Dielectric loss tangent (*tan δ*) has been calculated from equation (4.24). In general, loss has been found to increase with increase in *Te* content (Table 5.10). The optical conductivity (σ) has been evaluated using equation (4.25), and found to increase with the addition of *Te* content (Figure 5.27). The increase in σ is due to increase in the density of number of states. These defects states behave as dipoles which increase the dielectric loss.

Table 5.10 Values of dispersion energy (E_d), average energy gap (E_o), static refractive index (n_o) and loss tangent (*tan δ*) for $Ge_{19-y}Se_{63.8}Sb_{17.2}Te_y$ (y = 0, 2, 4, 6, 8, 10) alloys.

Samples	**E_d (eV)**	**E_o(eV)**	**n_o**	***tan δ***
***y* = 0**	21.88	3.41	2.72	0.1578
***y* = 2**	20.07	3.17	2.71	0.1506
***y* = 4**	21.05	3.13	2.78	0.1696
***y* = 6**	21.66	3.06	2.84	0.1842
***y* = 8**	23.42	3.05	2.95	0.2414
***y* = 10**	25.30	3.04	3.05	0.2616

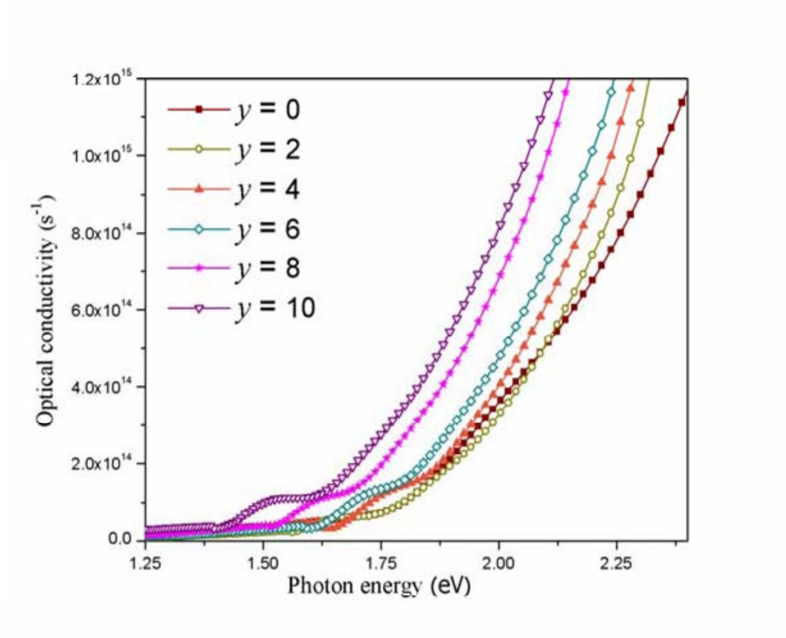

Figure 5.26 Variation of optical conductivity with photon energy for $Ge_{19\text{-}y}Se_{63.8}Sb_{17.2}Te_y$ (y = 0, 2, 4, 6, 8, 10) thin films.

5.4.2.3 Non–linear refractive index

Non–linear refractive index (n_2) has been calculated using Tichy and Ticha (equation (4.26)) & Fournier and Snitzer relation (equation (4.28)).

Table 5.11 Values of non–linear refractive index (Tichy and Ticha method), N' and non–linear refractive index (Fournier and Snitzer method) for $Ge_{19\text{-}y}Se_{63.8}Sb_{17.2}Te_y$ (y = 0, 2, 4, 6, 8, 10) thin films.

y	n_2×10^{-10} (esu) (Tichy and Ticha method)	N'×10^{22} (cm^{-3})	n_2×10^{-09} (esu) at 1.55 eV (Fournier and Snitzer method)
0	1.59	3.69	1.07
2	1.54	3.66	1.23
4	19.0	3.62	1.53
6	2.26	3.59	1.93
8	3.07	3.56	2.52
10	4.01	3.53	3.21

Non–linear susceptibility, $\chi^{(3)}$ has been evaluated using equation (4.27). $\chi^{(3)}$ increases with increasing *Te* content (Figure 5.28). Non–linear refractive index obtained from Fournier and Snitzer relation increases with increase in photon energy and with the concentration of *Te* (Figure 5.28). The values of n_2 for both the relations have been found to increase (Table 5.11). Non–linearity of glasses has been explained in terms of optical band gap and presence of defect states [214, 215]. With the increasing *Te* content, E_g^{opt} decreases and hence n_2 increases (section 4.4.2.3). Due to the presence of heteropolar and homopolar bonds, the probability of variety of defects gap states increase and this leads to an increase in non–linearity with increasing *Te* content in *Ge–Se–Sb–Te* glasses. [214, 215]. The presence of $GeSe_4$ (ν_2 mode), Se_6Te_2 rings, $GeTe_4$ tetrahedron, and *Te–Te* structural units (section 5.2.2.1) also increases the values of n_2.

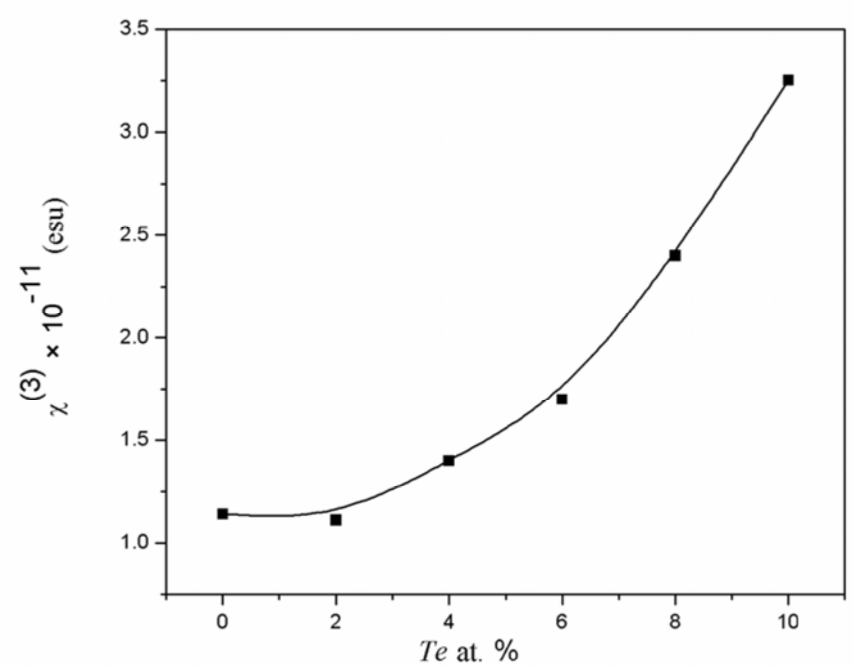

Figure 5.27 Variation of $\chi^{(3)}$ with *Te* concentration for $Ge_{19-y}Se_{63.8}Sb_{17.2}Te_y$ (y = 0, 2, 4, 6, 8, 10) alloys.

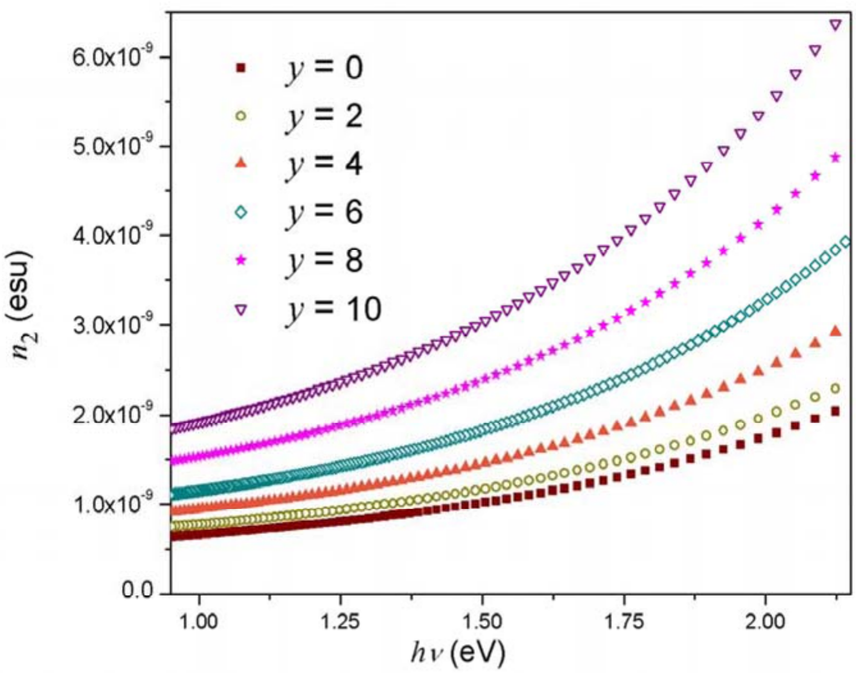

Figure 5.28 Variation of n_2 with $h\nu$ for $Ge_{19-y}Se_{63.8}Sb_{17.2}Te_y$ glassy alloys.

5. Conclusion

➢ For *Te* alloyed $Ge_{19}Se_{63.8}Sb_{17.2}$ system, average coordination number, number of constraints decreases. The lone–pair electrons and degree of covalency increase with increasing content of *Te*. There is decrease in mean bond energy due to which crosslinking between the network decreases and hence, rigidity of the system decreases. Therefore, parameter R increases while T_g decreases with decreasing value of average coordination number. Cohesive energy, heat of atomization and theoretical energy gap decrease. Electronegativity has been found to increase when *Te* is substituted for *Ge*.

➢ Structural results show that *Ge–Se*, *Te–Se*, *Se–Se* and *Sb–Se* have higher probability of bond formation in respective order. After formation of these bonds, the low energy bonds such as *Ge–Ge*, *Ge–Te*, *Te–Te*, *Sb–Te* and *Sb–Sb* have been formed. The addition of *Te* to $Ge_{19}Se_{63.8}Sb_{17.2}$ shows that the Far–IR absorption spectra shift a little towards the lower wavenumber side. *Te* impurity induces structural changes in the system with the formation of $GeTe_4$ units, $Te\text{–}Te$ bonds and $Se_{8-x}Te_x$ mixed rings.

- Thermal study reveals that three characteristic parameters *viz.* T_g, T_c and T_m decrease for $Ge_{19-y}Se_{63.8}Sb_{17.2}Te_y$ (y = 0, 2, 4, 6, 8, 10) system. The values of the glass transition temperature and crystallization temperature have been found to be dependent on heating rate and *Te* content. These parameters increase with increasing heating rate and decrease with *Te* addition. The value of glass forming ability decrease with increasing *Te* content. The activation energy of glass transition temperature and activation energy for crystallization temperature decrease with addition of *Te* content.
- Optical results show a red shift in $Ge_{19-y}Se_{63.8}Sb_{17.2}Te_y$ (y = 0, 2, 4, 6, 8, 10) thin films. Refractive index and extinction coefficient increase with increasing content of *Te*. Absorption coefficient increases with increasing photon energy. The optical band gap decreases while dielectric loss tangent and optical conductivity increase when *Ge* is replaced with *Te*. Non–linear refractive index and non–linear susceptibility increase with addition of *Te* content.

CHAPTER 6

Summary

The work has been carried out on ternary and quaternary chalcogenide glassy alloys. In ternary; *Ge–Se–Sb* system having composition $Ge_{19}Se_{81-x}Sb_x$ (x = 0, 4, 8, 12, 16, 17.2, 20) has been studied. In quaternary; *Ge–Se–Sb–Te* system with $Ge_{19-y}Se_{63.8}Sb_{17.2}Te_y$ (y = 0, 2, 4, 6, 8, 10) glassy alloys has been analyzed.

Ge–Se–Sb glasses have been studied for physical, structural, thermal and optical properties. Physical properties reveal that the average coordination number and number of constraints increase with increasing content of *Sb*. For x = 17.2, the parameter R = 1, there is no deviation in stoichiometry, showing it as a totally crosslinked composition. For R = 1, the values of mean bond energy, glass transition temperature and cohesive energy are highest. Theoretical energy gap has been found to decrease while density and molar volume of the system increase with increasing *Sb* content.

From the Far–IR study, $SbSe_3$ and *Sb–Se* bonds have been formed with the addition of *Sb* content. For x = 17.2 system gets crosslinked and having $GeSe_4$ and $SbSe_3$ structural units. The absorption peak at 156 cm^{-1} is attributed to *Sb–Sb* bonds.

The thermal study of *Ge–Se–Sb* alloys shows that thermal stability and glass forming ability are highest for 17.2 at.% of *Sb* content. The values of activation energy of glass transition temperature and crystallization temperature are maximum at x = 17.2 at.% of *Sb*. The crystallization results indicate that $Ge_{19}Se_{63.8}Sb_{17.2}$ composition is thermally stable.

Optical study reveals that transmission shifts toward the longer wavelength with *Sb* addition to *Ge–Sb* system. The extinction coefficient and absorption coefficient show maximum at x = 17.2. The interband transition is indirect and shows that optical band gap decreased up to x = 17.2. Average energy gap decreases and static refractive index increases with *Sb* addition. The dielectric loss and optical conductivity show maximum for x = 17.2. Non–linear refractive index and susceptibility increase with increasing content of *Sb*. Results show that the thin film sample for x = 17.2 has been found to be a good optical conductor.

The physical parameters, average coordination number and number of constraints decrease due to which crosslinking in the network decreases. The number of lone–pair electrons increase while mean bond energy, glass transition temperature and cohesive energy decrease. The values of electronegativity, density and molar volume increase while theoretical energy gap decreases with increasing *Te* content.

Far–IR absorption spectra shift a little towards the lower wavenumber side with the addition of *Te* content. With *Te* addition, new *Ge–Te* and *Te–Te* homopolar bonds have been formed.

Glass transition temperature, crystallization temperature and melting temperature decrease with the addition of *Te* content and increase with the increase in heating rate. The glass forming ability decreases with increasing *Te* content. The activation energy of glass transition temperature and crystallization temperature decrease with addition of *Te* content

Red shift has been observed when *Te* is incorporated in *Ge–Se–Sb–Te* system. Refractive index and extinction coefficient increase. Optical band gap decreases with addition of *Te* content. Average energy gap decreases while dispersion energy increases with addition of *Te* content. Dielectric loss tangent and optical conductivity increases with *Te* addition. Non−linear refractive index increases with increasing *Te* content. These glasses exhibit high linear and non−linear refractive index which may makes them potential candidates for integrated optics, ultrahigh−bandwidth signal processing and infrared optical sensors for medical applications.

$Ge_{19}Se_{81-x}Sb_x$ (x = 0, 4, 8, 12, 16, 17.2, 20) and $Ge_{19-y}Se_{63.8}Sb_{17.2}Te_y$ (y = 0, 2, 4, 6, 8, 10) systems can be further explored for electrical properties. Non−linear refractive index can be studied experimentally using Z−scan technique.

References

[1] Zachariasen W H J. *Am. Chem. Soc.* 1932 **54** 3841.

[2] Ray N H 1978 *Inorganic Polymers* New York: Academic Press, 1978.

[3] Elliott S R *Chalcogenide glasses* New York: Materials Science and Technology, 1991.

[4] Suvorova L N, Borisova Z U and Orlova G M *Izv. Acad. Nauk SSSR, Neorg. Mater.* 10(3) (1974) 441.

[5] Schultz-Sellack C 1870 *Annalen der Physik und Chemie* **139** 182.

[6] Wood R W 1902 *Phil. Mag.* **3** 607.

[7] Meier W 1910 *Annalen der Physik und Chemie* **31** 1017.

[8] Frerichs R 1950 *Physical Review* **78** 643.

[9] Frerichs R 1953 *J. Opt. Soc. Am.* **43** 1153.

[10] Fraser W A 1953 *J. Opt. Soc. Am.* 43 823.

[11] Dewulf G *Rev. Opt.* **33** (1954) 513.

[12] Winter Klein A 1955 *Verres et. Refractaires* **9** 147.

[13] Goriunova NA and Kolomiets B T 1955 *Zhurnal Tekhnicheskoi Fiziki* **25** 2069.

[14] Ovshinsky S R 1968 *Phys. Rev. Lett.* **21** 1450 & Ovshinsky S R 1970 *J. Non−Cryst. Solids* **2** 99.

[15] Mott N F and Davis E A *Electronic Processes in the Non−Crystalline Materials* Oxford: Clarendon Press, 1979.

[16] Paul A *Chemistry of Glasse, Second Edn* Dordrecht: Kluwer Academic 1990.

[17] Zallan R *The Physics of Amorphous Solids* New York: John Wiley, 1983.

[18] Elliott S R *Physics of Amorphous Materials Second Edn* New York: Longman 1990.

[19] Popescu M *Non−Crystalline Chalcogenides* Dordrecht: Kluwer Academic 2000.

[20] Fairman R and Ushkov B *Semiconductors and Semimetals, Semiconducting Chalcogenide Glass I* USA: Elsevier Academic Press 2004.

[21] Fairman R and Ushkov B *Semiconductors and Semimetals, Semiconducting Chalcogenide Glass II* USA: Elsevier Academic Press 2004.

[22] Fairman R and Ushkov B *Semiconductors and Semimetals, Semiconducting Chalcogenide Glass III* USA: Elsevier Academic Press 2004.

[23] Mikla V I and Mikla V V *Metastable States in Amorphous Chalcogenide Semiconductors* Dordrecht, New York: Springer 2010.

[24] Golovchak R, Shpotyuka O, Mccloy J S, Riley B J, Windisch C F, Sundaramc S K, Kovalskiy A and Jaind H 2010 *Phil. Mag.* **90** 4489.

[25] Fayek S A 2005 *Infrared Phys. Techn.* **46** 193.

[26] Iovu M S, Kamitsos E I, Varsamis C P E, Boolchand P and Popescu M 2005 *J Optoelectron. Adv. Mater.* **7** 1217.

[27] Mykaylo O A, Guranich O G, Rubish V M, Stefanovich V O, Shpyrko G M and Kaynts D I 2008 *Ferroelectrics* **372** 81.

[28] Santos L F, Ganjoo A, Jain H and Almeida R M 2009 *J. Non−Cryst. Solids* **355** 1984.

[29] Delaizir G, Dussauze M, Nazabal V, Lecante P, Dolle M, Rozier P, Kamitsos E I, Jovari P and Bureau B 2011 *J. Alloy. Compd.* **509** 831.

[30] Sharma P, Rangra V S, Sharma P and Katyal S C 2009 *J. Alloy. Compd.* **480** 934.

[31] Holubova J, Cernosek Z and Cernoskova E 2009 *J. Non−Cryst. Solids* **355** 2050.

[32] Shaaban E R and Tomsah I B I 2011 *J Therm. Anal. Calorim.* **105** 191.

[33] Bletskan D I 2005 *Chalcogenide Lett.* **2** 121.

[34] Piarristeguy A A, Barthelemy E, Krbal M, Frayret J, Vigreux C and Pradel A 2009 *J. Non−Cryst. Solids* **355** 2008.

[35] Sushama D, Achamma G and Predeep P 2006 *J. Optoelectron. Adv. Mater.* **8** 1639.

[36] Tiwari R S, Mehta N, Shukla R K and Kumar A 2006 *J. Optoelectron. Adv. Mater.* **8**, 1211.

[37] Kotkata M F and Mansour Sh. A 2011 *J. Therm. Anal. Calorim.* **103** 957.

[38] Mehta N, Agrahari S K and Kumar A 2006 *Physica Scripta* **74** 579.

[39] Mehta N, Tiwari R S and Kumar A 2006 *Materials Research Bulletin* **41** 1664.

[40] Saraswat S and Kushwaha S S S 2009 *J. Therm. Anal. Calorim*. **96** 923.

[41] Mehta N and Singh K 2008 *Phil. Mag.* **9** 1411.

[42] Kapoor M and Thakur N 2010 *Integrated Ferroelectrics* **118** 53.

[43] Nemec P, Jedelsky J, Frumar M, Stabl M and Cernosek Z 2005 *Thin Solids Films*, **484** 140.

[44] Shaaban E R, El-Kabnay N, Abou-sehly A M and Afify N 2006 *Physica B* **381** 24.

[45] Kotkata M F, Abdel-Wahab F A and Al-Kotb M S 2009 *Appl. Surf. Sci.* **255** 9071.

[46] Fadel M, Fayek S A, Abou-Helal M O, Ibrahim M M and Shakra A M 2009 *J. Alloy. Compd.* **485** 604.

[47] Shaaban E R, El-Hagary M, Emam-Ismail M and El-Den M B 2011 *Phil. Mag.* **91** 1679.

[48] Sharma P, Sharma I and Katyal S C 2009 *J. Appl. Phys.* **105** 053509.

[49] Pan R K, Tao H Z, Zang H C, Zhang T J and Zhao X J 2009 *Physica B* **404** 3397.

[50] Othman A A 2006 *Thin Solid Films* **515** 1634.

[51] Mainka, Sharma P, Katyal S C and Thakur N 2008 *J. Phys. D: Appl. Phys.* **41** 235301.

[52] Sharma P, Rangra V S, Sharma P and Katyal S C 2008 *J. Phys. D: Appl. Phys.* **41** 225307.

[53] Aly K A 2010 *Appl. Phys. A* **99** 913.

[54] Bahishti A A, Husain M and Zulfequar M 2011 *Radiation Effects & Defects in Solids* **166** 529.

[55] Mishra M, Chauhan R and Srivastava K K 2010 *Integrated Ferroelectrics* **118** 34.

[56] Machado K D, Sanchez D F, Maciel G A, Brunatto S F, Mangrich A S and Stolf S F 2009 *J. Phys.: Condens. Matter* **21** 195406.

[57] Boulmetis Y C, Raptis C and Arsova D 2005 *J. Optoelectron. Adv. Mater.* **7** 1209.

[58] S.M. El-Sayed 2003 *Semiconductor Science and Technology*, **18** 337.

[59] Wang G, Nie Q, Wang X, Shen X, Chen F, Hu T, Dai S and Zhang X 2011 *J. Appl. Phys.* **110** 043536.

[60] Adam A B 2009 *J. King Saud University – Science* **21** 93.

[61] Sun J, Nie Q, Wang X, Dai S, Zhang X, Bureau B, Boussard C, Conseil C and Ma H 2012 *Infrared Phys. Techn.***55** 315.

[62] Zha C, Wang R, S. Anita, Prasad A, Ruth A J and Davies B L 2007 *J Mater Sci: Mater. Electron.* **18** 389.

[63] Fayek S A, Fouad S S, Balboula M R and El-Bana M S 2007 *Physica B* **388** 230.

[64] Sharmila B H and Asokan S 2006 *Philos. Mag. Lett.* **86** 155.

[65] Ko J B and Myung T S Structural 2011 *J. Ceramic Processing Research.* **12**, 132.

[66] Vazquez J, Gonzalez-Palma R, Cardenas-Leal J L, D G G Barreda, Lopez-Alemany P L, Villares 2010 *J. Mat. Sci.* **45**, pp. 2974.

[67] Prikryl J, Hrdlicka M, Frumar M, Orava J, Benes L, Vlcek M, Kostal P, Hromadko L and Wagner T 2009 *J. Non−Cryst. Solids* **355** 1998.

[68] Dahshana A, Aly K.A. and Dessouky M T 2008 *Philo. Mag*. **88** 2399.

[69] Shaaban E R, Tomsah I B I 2011 *J. Therm. Anal. Calorim*. **105** 191.

[70] Khan S A, Al-Hazmi F S, Faidah A S, Yaghmour S J, Al-Sanosi A M and Al-Ghamdi A A 2009 *J. Alloy. Compd.* **484** 649.

[71] Lafi O A, Imran Mousa M A, Abdullah M K 1008 *Mat. Chem. and Phys.* **108** 109.

[72] Saxena M J 2005 *Phys. D: Appl. Phys.* **38** 460.

[73] Naqvi S F and Saxena N S 2012 *J. Therm. Anal. Calorim.* 108 1161.

[74] Fayek S A and Fadel M 2009 *J. Non−Oxide Glasses* **1** 239.

[75] Deepika, Jain P K, Rathore K S and Saxena N S 2009 *J. Non−Cryst. Solids* **355** 1274.

[76] Shaaban E R, Kansal I, Shapaan M and. Ferreira J M F 2009 *J. Therm. Anal. Calorim*. **98** 347.

[77] Tiwari R S, Mehta N, Shukla R K and Kumar A 2005 *J. Therm. Anal. Calorim*. **82** 45.

[78] Sharma A and Barman P B 2009 *Thin Solid Films* **517** 3020.

[79] Jain P K, Deepika and Saxena N S 2009 *Phil. Mag*. **89** 641.

[80] Mehta N, Singh K and Kumar S 2009 *Phase Transitions* **82** 43.

[81] Shaheen A A, Imran M M A, Lafi O A, Awadallah M and Abdullah M K 2010 *Rad. Phys. Chem.* **79** 923.

[82] Saffarini G, Saiter J M and Schmitt H 2007 *Opt. Mater.* **29** 1143.

[83] Abdel-Rahim M, AHafiz M M, El-Nahass M M and Shamekh A M 2007 *Physica B: Condensed Matter* **387** 383-391.

[84] Pan R K, Tao H Z, Zang H C, Zhao X J and Zhang T J 2010 *Appl. Phys. A* **99** 889.

[85] Sharma P and Katyal S C 2007 *Thin Solid Films* **515** 7966.

[86] Dahshan A, Amer H H and Aly K A 2008 *J. Phys. D: Appl. Phys.* **41** 215401.

[87] Sharma P and Katyal S.C 2007 *J. Phys. D: Appl. Phys*. **40** 2115.

[88] Petkova T, Ilcheva V, Petkov E, Petkov P, Socol G, Sima F, Ristoscu C, Mihailescu C N, Mihailescu I N, Popov C and Reithmaier J P 2011 *Appl. Phys. A* **104** 959.

[89] Saleh S A, Al-Hajry A and Ali H.M 2011 *Physica Scripta* **84** 015604.

[90] Shaaban E R, Kaid M A, Moustafa E S and Adel A 2008 *J. Physics D: Appl. Phys.* **41** 125301.

[91] Hosni H M, Fayek S A, El-Sayed S M, Roushdy M and Soliman M A 2006 *Vacuum* **81** 54.

[92] Naik R, Jain A, Ganesan R and Sangunni K S 2012 *Thin Solid Films* **520** 2510.

[93] Wang G, Nie Q, Wang X, Dai S, Xu T, Shen X, Zhang X 2010 *Physica B* **405** 4424.

[94] Petit L, Carlie N, Richardson K, Guo Y, Schulte A, Campbell B, Ferreria B and Martin S 2005 *J. Phys. Chem. Solids* **66** 1788.

[95] Dahshan A 2008 *J. Non−Cryst. Solids* **354** 3034.

[96] Aly K A, Dahshan A and Abdel-Rahim F M 2009 *J. Alloy. Compd*. **470** 574.

[97] Kumar S and Singh K 2012 *Therm. Chim. Act.* **528** 32.

[98] Sharma P and Katyal S C 2009 *Appl. Phys. B: Lasers and Optics* **95** 367.

[99] Sharma I, Tripathi S K and Barman P B 2008 *Appl. Surf. Sci.* **255** 2791.

[100] Dahshan A and Aly K A 2008 *Acta Mater.* **56** 4869.

[101] Aly K A 2009 *Phil. Mag.* 89 1063.

[102] Ahmad M, Kumar J and Thangaraj R 2009 *J. Non−Cryst. Solids* **355** 2345.

[103] VanStryland E W, Wu Y Y, Hagan D J, Soileau M J and Mansour K 1988 *J. Opt. Soc. Am. B* **5**, 1980.

[104] Troles J, Smektala F, Boudeb G, Monteil A, Bureau B and Lucas J 2002 *J. Optoelectron. Adv. Mater*. **4** 729.

[105] Tintu R, Nampoori V P N, Radhakrishnan P and Thomas S 2011 *J. Phys. D: Appl. Phys.* **44** 025101.

[106] Anne M L, Keirsse J, Nazabal V, Hyodo K, Inoue S, Boussard-Pledel C, Lhermite H, Charrier J, Yanakata K, Loreal O, Person J L, Colas F, Compere C and Bureau B 2009 *Sensor.* **9** 7398.

[107] Lucas P, Solis M A, Coq D L, Juncker C, Riley M R, Collier J, Boesewetter D E, Boussard-Pledel C and Bureau B 2006 *Sensor. Actuator. B* **119** 355.

[108] Al-Agel F A 2013 *J. Alloy. Compd.* **568** 92.

[109] Ganjoo A, Khalid S and Pantano C G 2005 *Phil. Mag. Lett.* **85** 503.

[110] Sayed El and Farag M 2004 *Optics & Laser Technology* **36** 35.

[111] Lucovsky G and Hayes T M *Amorphous Semiconductors* Berlin: Springer Verlag, 1985.

[112] Zallen R *The Physics of Amorphous Solids* USA: John Wiley, 1998.

[113] Lucovsky G, Galeener F L, Keezer R C, Geils R H and Six H A 1974 *Phys. Rev. B* **10** 5134.

[114] Tronc P, Bensoussan M, Brenac A, Sebenne C 1973 *Phys. Rev. B* **8** 5947.

[115] Mott N F *Adv. Phys.* 1967 **16** 144.

[116] Lucovsky G, Caleener F L, Ceils R H, Keezer R C *The Structure of Non−Crystalline Materials* London: Taylor and Francis, 1977.

[117] Lucovsky G, Nernanich R J and Galeener F L *Amorphous and Liquid Semiconductors* G.G. Stevenson: Dundee, 1979.

[118] http://physicalchemistryresources.com/Book5_sections/pc_ec_titleandcontents_10132009.htm

[119] Haines P J, Reading M and Wilburn *F W Handbook of Thermal Analysis and Calorimetry*, 1998.

[120] Hodge I M and Berens A R 1982 *Macromolecules* **15** 762.

[121] Morigaki K *Physics in Amorphous Semiconductors* London: Imperical College Press, 1999.

[122] Bagley B G *Amorphous and Liquid Semiconductors* US: Springer, 1974.

[123] Struik L C E 1977 *Polymer Eng. Sci.* **17** 165.

[124] Moynihan C T, Easteal A J, Wilder J and Tucker J 1974 *J. Phys. Chem.* **78** 2673.

[125] Kissinger H E 1956 *J. Res. Bur. Stand.* **57** 217.

[126] Kissinger H E 1957 *Anal. Chem.*29 1702.

[127] Colemenero J and Barandiaran J M 1978 *J. Non−Cryst. Solids* **30** 263.

[128] Mahadevan S, Giridhar A and Singh A K 1986 *J. Non−Cryst. Solids* **88** 11.

[129] Augis J A and Benett J E J. 1978 *Therm. Anal. Cal.* **13** 283.

[130] Kastner M 1972 *Phys. Rev. Lett.* **28** 355.

[131] Hecht E *Optics* fourth ed. San Francisco: Addison−Weley, 2002.

[132] Simmons J H and Potter K S *Optical Materials* Academic Press, San Diego,Calif.; London, 1999.

[133] Hecht E *Optics* second ed. San Francisco: Addison-Weley, 1988.

[134] Granaststein V L *Encyclopedia of Physics* New York: VCH Publication 1991.

[135] Sanghera J S and Aggarwal I D 1999 *J. Non−Cryst. Solids* **256−257** 6.

[136] Bureau B, Boussard-Pledel C, Lucas P, Zhang X and Lucas J 2009 Molecules **14** 4337.

[137] Swanepoel R 1983 *J. Phys. E: Sci. Instrum.* **16** 1214.

[138] Swanepoel R 1984 *J. Phys. E: Sci. Instrum.* **17** 896.

[139] Lyashenko S P and Miloslavskii V K 1964 *Opt. Spectros.* **16** 80.

[140] Wales J, Lovitt G J and Hill R A 1967 *Thin Solid Films* **1** 137.

[141] Szczyrbowski J and Czapla A 1977 *Thin Solid Films* **46** 127.

[142] Miller D A B 2007 Photonics Spectra 80−83.

[143] Tauc J *The Optical Properties of Solids* Amsterdam: North Holland, 1979.

[144] Cohen M H, Fritzsche H and Ovshinsky S R 1969 *Physics. Review Lett.* **22** 1065.

[145] Wemple S H and Di–Domineco 1971 M *Physics. Rev. B* **3** 1338.

[146] Wemple S H 1973 *Physics. Rev. B* **7** 3767.

[147] Fischer M and H Krebs *Amorphous Materials* London & New York: Wiely−Interscience 1972.

[148] Pearson A *Modern Aspects of the Vitreous State* London: Butterworth 1964.

[149] A Feltz *Amorphous Inorganic Materials and Glasses* Tokiyo: VCH 1993.

[150] Abkowitz M, Foley G M T, Markovics J M and Palumbo AC *Optical Effects in amorphous Semiconductors* (*AIP Conf. Proc.* vol 120) New York: American Institute for Physics 117 1984

[151] Marquez E, Ramirez-Malo J, Villares P. Jimenez-Garay R, Ewen P J S and Owen A E 1992 *J. Phys. D: Appl. Phys*. **25** 535.

[152] Phillips J C 1981 *J. Non−Cryst. Solids* **43** 37.

[153] Phillips J C and Thorpe M F 1985 *Solid State Commun.*53 699.

[154] Tanaka K 1989 *Phys. Rev* B **39** 270.

[155] Phillips J C 1981 *J. Non−Cryst. Solids* **34** 153.

[156] Boolchand P, Georgiev D G and Goodman B 2001 *J. Opto. Electron. Adv. Mater.* **3** 703.

[157] Thorpe M F 1983 *J. Non−Cryst. Solids* **57** 355.

[158] Fouad S S, Fayek S A and Ali M H 1998 *Vacuum* **49** 25.

[159] Zhenhua L 1991 *J. Non−Cryst. Solids* **127** 298.

[160] Tichy L and Ticha H 1994 *Mater. Lett.* **21** 313.

[161] Tichy L and Ticha H 1995 *J. Non−Cryst. Solids* **189** 141.

[162] Pauling L *The Nature of the Chemical Bond* New York: Cornell University Press, 1960.

[163] Bicerano J and Ovshinsky S R 1985 *J. Non−Cryst. Solids* **75** 169.

[164] Sanderson R T *Inorganic Chemistry* New Delhi: Affilated East-West Press PUT, 1971.

[165] Kastner M, Adler D and Fritzche H 1976 *J. Phys. Rev. Lett.* **37** 1504.

[166] Sadagopan V and Gotos H C 1965 *Solid State Electron.* **8** 529.

[167] Yamaguchi M 1985 *Phil. Mag.* **51** 651.

[168] Fayek S A, Balboul M R, Marzouk K H 2007 *Thin Solid Films* **515** 7281.

[169] Tichy L, Ticha H, Nagels P and Callaerts R 1998 *J. Non−Cryst. Solids* **240** 177.

[170] Nagels P, Tichy L, Sleeckx E and Callaerts R 1998 *J. Non−Cryst. Solids* **227−230** 705.

[171] Luckovsky G *Physics of Selenium and Tellurium* Berlin: VCH, 1969.

[172] Quiroga I, Corredor C, Bellido F, Vazquez J, Villares P and Jimnez Garay R 1996 *J. Non−Cryst. Solids* **196** 183.

[173] Somyajulu G R 1958 *J. Chem. Phys.* **28** 814.

[174] Ohsaka T 1975 *J. Non−Cryst. Solids* **17** 121.

[175] Ball G J and Chamberlain J M 1978 *J. Non−Cryst. Solids* **29** 239.

[176] Fukunaga T, Tanaka Y and Murase K 1982 *Solid State Commun.* **42** 513.

[177] Goyal D R and Mann A S 1995 *J. Non−Cryst. Solids* **183** 182.

[178] Kumar P, Sathiataj T S and Thangraj R 2010 *Phil. Mag. Lett.* **90** 183.

[179] Sharma A K, Bhatia K L, Bhatnagar V K and Malik S K 1989 *J. Non−Cryst. Solids* **108** 309.

[180] Rechtin M D, Hilton A R and Hayes D J 1975 *J. Elec. Mater* **4** 347.

[181] Zhu J Q, Bo Z L, Dong D K 1996 *Phys. Chem. Glasses* **37** 264

[182] Abdel-Rahim MA, Ibrahim M M, Dongol M and Gaber A 1992 *J. Mater. Sci.* **27** 4685.

[183] Hruby A 1972 *J. Phys. B* **22** 1187.

[184] Kauzmann W 1948 *Chem. Rev.* **43** 219.

[185] Lafi O A, Imran M M A and Abdullah M K 2007 *Physica B: Condens. Mater.* **395** 69.

[186] Kumar R, Sharma P, Barman P B, Sharma V, Katyal S C and V.S. Rangra 2012 *J. Therm. Anal. Calorim.* **110** 1053.

[187] Al-Ghamdi A A 2006 Vacuum **80** 400.

[188] Marquez E, Gonzalez-Leal J M, Bernal−Oliva A M, Wagner T and Jimenez−Garay R 2007 *J. Phys. D: Appl. Phys.* **40** 5351.

[189] Manifacier J C, Gasiot J and Fillard J P 1976 *J. Phys. E: Instrum.* **9** 1002.

[190] Gonzalez-Leal J M, Prieto-Alcon R, Angel J A and Marquez E 2003 *J. Non−Cryst. Solids*. **315** (2003) 134.

[191] Marquez E, Gonzalez-Leal J M, Bernal-Oliva A M, Jimenez-Garay R and Wagner T 2008 *J. Non−Cryst. Solids.* **354** 503.

[192] Tanaka K 1980 *Thin Solid Films* **66** 271.

[193] Mott N F and Davis E A 1970 *Phil. Mag.* **22** 903.

[194] El-Metwally E G, Abou-Helal M O and Yahia I S 2008 *J. Ovonic Res.* **4** 20.

[195] Pankove J I *Optical Processes in Semiconductors* New York: Dover 1975.

[196] Khan M A M, Kumar S, Husain M and Zulfequar M 2009 *J. Non−Oxide Glasses* **1** 71.

[197] Ticha H and Tichy L 2004 *J. Optoelectron. Adv. Mater.* **4** 381.

[198] Fournier J and Snitzer E 1974 *IEEE J. Quantum Electron.* **10** 473.

[199] Wyne J 1969 *J. Phys. Rev.* **178** 1295

[200] Moss T S 1985 *Phys. Stat. Sol.* (*b*) **131** 415.

[201] Pamukchieva V, Szekeres A, Todorova K, Fabian M, Svab E, Revay Zs and Szentmiklosi L 2009 *J. Non−Cryst. Solids* **355** 2485.

[202] Aly K A, Othman A A and Abousehly A M 2009 *J. Alloys Compd.* **467** 417.

[203] El-Sayed S M, Saad H M, Amin G A, Hafez F M and Abd-EI-Rahman M 2007 *J. Phys. Chem. Solids* **68** 1040.

[204] Mainka, Sharma P, Thakur N 2009 *Philos. Mag.* **89** (2009) 3027-3036.

[205] Othman A A, Aly K A and Abousehly A M 2007 *Thin Film Solid* **515** 3507.

[206] Pamukchieva V, Szekeres A, Todorova K, Svab E and Fabian M 2009 *Opt. Mater.* **32** 45.

[207] Andrikopoulos K S, Yannopoulos S N, Voyiatzis G A, Kolobov A V, Ribes M and Tominaga J 2006 *J. Phys. Condens. Matter.* **18** 965.

[208] Sharma P and Katyal S C 2008 *J. Non−Cryst. Solids* **354** 3836.

[209] Wang Z, Li Y, Chen Q and Tu C 1995 *J. Non−Cryst. Solids* **191** 132.

[210] Schottmiller J, Tabak M, Lucovsky G and Ward A 1970 *J. Non−Cryst. Solids* **4** 80.

[211] Dietzel A 1968 *Glastech. Ber.* **22** 41.

[212] Calventus Y, Surinach S, Baro M D 1997 *Mater. Sci. Eng. A* **226−228** 818.

[213] Rao C N R, George M V, Mahanty J and Narasimhan P T *Handbook of Chemistry and Physics* New Delhi: Affiliated East–West Press, 1970

[214] Petit L, Carlie N, Chen H, Gaylord S, Massera J, Boudebs G, Hu J, Agarwal A, Kimerling L and Richardson K 2009 *J. Solid State Chem.* **182** 2756.

[215] Gopinath J T, Soljacic M and Ippen E P 2004 *J. Appl. Phys.* **96** 6931.

LIST OF PUBLICATIONS

1. **Neha Sharma**, Sunanda Sharda, S.C. Katyal, Vineet Sharma and Pankaj Sharma, "*Effect of Te on linear and non-linear optical properties of new quaternary Ge−Se−Sb−Te chalcogenide glasses*" 2013 **Electronic Materials Letters** DOI: http://dx.doi.org/10.1007/s13391-013-3168-1 (*in press*).

2. **Neha Sharma**, Sunanda Sharda, Vineet Sharma and Pankaj Sharma, "*Far−Infrared Investigation of Ternary Ge−Se−Sb and Quaternary Ge−Se−Sb−Te Chalcogenide Glasses*" 2013 **Journal of Non–Crystalline Solids**, 375 (2013) 114–118.

3. **Neha Sharma**, Sunanda Sharda, Vineet Sharma and Pankaj Sharma, "*Effect of Antimony Addition on Thermal Stability and Crystallization Kinetics of Germanium – Selenium Alloys*" **Journal of Non–Crystalline Solids,** 371−372 (2013) 1–5.

4. **Neha Sharma**, Sunanda Sharda, Vineet Sharma and Pankaj Sharma, "*Stability Analysis of IV-V-VI Chalcogenide Glasses Using Glass Transition and Crystallization Temperature*" 2013 **AIP Conference Proceedings,** 1536 (2013) 615–616**.**

5. **Neha Sharma**, Sunanda Sharda, Vineet Sharma and Pankaj Sharma, "*Nonlinear optical properties of IV-V-VI chalcogenide glasses*" **AIP Conference Proceedings,** 1512 (2013) 546–547.

6. **Neha Sharma**, Sunanda Sharda, Vineet Sharma and Pankaj Sharma, "*Evaluation of Physical Parameters for New Quaternary $Ge_{19-y}Se_{63.8}Sb_{17.2}Te_y$ Chalcogenide Glasses*" **Chalcogenide Letters,** 9 (2012) 355–363.

7. **Neha Sharma**, Sunanda Sharda, Vineet Sharma and Pankaj Sharma, "*Optical analysis of $Ge_{19}Se_{81-x}Sb_x$ thin films using single transmission spectrum*" **Materials Chemistry and Physics**, 136 (2012) 967–972.

8. **Neha Sharma**, Sunanda Sharda, Vineet Sharma and Pankaj Sharma, "*Structural Rigidity, Percolation and Transition-Temperature Study of the* $Ge_{19}Se_{81-x}Sb_x$ *System*" **Defect and Diffusion Forum** 316–317 (2011) 37–44.

Communicated

1. **Neha Sharma**, Sunanda Sharda, Vineet Sharma and Pankaj Sharma, "*Glass transition and crystallization kinetics for* $Ge_{19-y}Se_{63.8}Sb_{17.2}Te_y$ *multi−component glassy alloys*" (2013).

National/ International Conferences

1. **Neha Sharma,** Sunanda Sharda, Vineet Sharma and Pankaj Sharma, "*Stability Analysis of IV-V-VI Chalcogenide Glasses Using Glass Transition and Crystallization Temperature*" at **International Conference – Recent Trends in Applied Physics and Material Science**, organized by GCET, Bikaner during February 1–2, 2013.

2. **Neha Sharma,** Sunanda Sharda, Vineet Sharma and Pankaj Sharma, "*Nonlinear optical properties of IV-V-VI chalcogenide glasses*" at **57th DAE Solid State Physics Symposium**, organized at IIT–Mumbai during Dec 3–7, 2012.

3. **Neha Sharma,** Sunanda Sharda, Vineet Sharma and Pankaj Sharma, "*Effect of Sb on Dispersion Parameters of Ge-Se Chalcogenide Thin Films*" at **National Conference – Recent Trends in Materials Science**, organized by JUIT, Waknaghat during October 8–10, 2011.

4. **Neha Sharma,** Sunanda Sharda, Vineet Sharma and Pankaj Sharma, "*Chemical Bond Distribution and Cohesive energy of* $Ge_{19}Se_{81-x}Sb_x$ *System*" at **National Conference – Research Methods in Science, Technology and Management** organized by GHEC, Kumarhatti during March 26–27, 2011.